

# **MELT SPINNING OF CONTINUOUS FILAMENTS BY COLD AIR ATTENUATION**

A Thesis  
Presented to  
The Academic Faculty

by

Jun Jia

In Partial Fulfillment  
of the Requirements for the Degree  
Doctor of Philosophy in the  
School of Materials Science and Engineering

Georgia Institute of Technology  
December 2010

# **MELT SPINNING OF CONTINUOUS FILAMENTS BY COLD AIR ATTENUATION**

Approved by:

Dr. Donggang Yao, Advisor  
School of Materials Science and Engineering  
*Georgia Institute of Technology*

Dr. Karl Jacob  
School of Materials Science and Engineering  
*Georgia Institute of Technology*

Dr. Youjiang Wang, Advisor  
School of Materials Science and Engineering  
*Georgia Institute of Technology*

Dr. Wallace W. Carr  
School of Materials Science and Engineering  
*Georgia Institute of Technology*

Dr. Kyriaki Kalaitzidou  
School of Mechanical Engineering  
*Georgia Institute of Technology*

Date Approved: August 16, 2010

## ACKNOWLEDGEMENTS

I express my sincere thanks to my thesis advisors, Dr. Donggang Yao and Dr. Youjiang Wang, for their invaluable guidance, support and encouragement during my PhD research. I would like to thank Dr. Karl Jacob, Dr. Wallace W. Carr and Dr. Kyriaki Kalaitzidou for serving in the thesis committee and providing valuable suggestions.

I'm grateful to Dr. Wallace W. Carr's research group for allowing me to use their air drying system.

I would like to thank Yaodong Liu, Xuxia Yao, Dr. Kaur Jasmeet and Dr. Mihir Oka for helping with the fiber characterization experiments and their helpful advice.

I wish to thank my former and current group members, Dr. Nagarajan Pratapkumar, Dr. Ruihua Li, Wei Zhang, Ram K.R.T., Sarang Deodhar, Ian Winters and Tom Wyatt, for their help and cooperation on experiments and valuable discussions.

I would like to thank GTRI machine shop and ME machine shop for helping with the design and fabrication of the extrusion/fiber spinning dies.

## TABLE OF CONTENTS

ACKNOWLEDGEMENTS	iv
LIST OF TABLES	x
LIST OF FIGURES	xi
SUMMARY	xviii
CHAPTER 1 Introduction and Literature Review	1
1.1. Fiber Spinning Technology	1
1.2. Fundamental of Melt Spinning	10
1.2.1. Tension in Melt Spinning Line	10
1.2.2. Kinematics of Melt Spinning	12
1.2.3. Formation of Fiber Structure	15
1.2.4. Numerical Simulations	18
1.3. Fundamental of Melt Blowing	18
1.4. Crystallization Behavior of Isotactic Polypropylene	19
1.4.1. Mesophase Structure	19
1.4.2. Crystalline Structure	20
1.4.3. Two Melting Endotherm Peaks	22
1.4.4. Effect of Processing Temperature and Take-up Speed on Crystallinity in Melt Spinning	25
1.4.5. Effect of Cooling Rate on Crystallinity	26
CHAPTER 2 Research Motivations and Objectives	27

CHAPTER 3 Design of Apparatus for Melt Spinning by Cold Air Attenuation	30
3.1. Design of High Speed Air Jet Nozzle	30
3.1.1. Incompressible Air Flow	31
3.1.2. Compressible Air Flow	32
3.2. Design of Spinneret Pack	36
3.3. Experiment Setup	41
CHAPTER 4 Computational Fluid Dynamics Simulation of The Fiber Attenuation	43
4.1. Model Description	43
4.2. Material Properties and Viscosity Characterization	45
4.3. Model Formulation	50
4.4. Simulation Results and Discussion	51
4.4.1. Velocity Profile and Distribution of Filament	51
4.4.2. Polymer Viscosity Effect	52
4.4.3. Processing Temperature Effect	54
4.4.4. Air/Polymer Flow Ratio Effect	56
4.4.5. Limitations	58
CHAPTER 5 Experimental Studies	59
5.1. Materials	59
5.2. Design of Parametric Studies	60
5.3. Fiber Production	61

5.4. Fiber Characterizations	62
5.4.1. Fiber Microstructures	63
5.4.2. Thermal Analysis	63
5.4.3. Mechanical Properties	64
5.4.4. Rheology	65
5.4.5. Fiber Molecular Orientation	65
5.4.6. Fiber Crystallization Behavior	68
CHAPTER 6 Experimental Results and Discussions	69
6.1. Fiber Geometry	69
6.1.1. Effect of Polypropylene Viscosity and Processing Temperature	69
6.1.2. Effect of Air/polymer Volume Flow Ratio	74
6.1.3. Fiber Morphology	75
6.2. Fiber Molecular Orientation	77
6.3. Crystallization Behavior of Resulting Fibers	80
6.3.1. Crystallinity	80
6.3.2. Crystal Form and Crystallite Size	86
6.4. Fiber Mechanical Properties	87
6.5. Melting and Crystallization Temperature	91
6.6. Comparisons with Traditional Melt Spinning	97
6.6.1. Fiber Properties	97

6.6.2.	Cost Analysis and Possibility of Scale up	97
6.7.	Fibers Made from Nylon 6	98
CHAPTER 7 Theoretical Analysis and Modeling of Cold Air Attenuation In Melt Spinning Process		102
7.1.	Introduction and Objectives	102
7.2.	Literature Review	103
7.3.	Model Formulation	114
7.3.1.	Model Description	114
7.3.2.	Governing Equations	115
7.3.3.	Constitutive Equations	117
7.3.4.	Boundary Conditions	117
7.4.	Method of Solution	118
7.5.	Validation of Computation Method	120
7.6.	Isothermal Model	124
7.6.1.	Effect of Model Geometry Length	126
7.6.2.	Effect of Polymer Viscosity	128
7.6.3.	Effect of Initial Fiber Velocity	129
7.6.4.	Effect of Air Flow Velocity	131
7.7.	Non-isothermal Model	131
7.7.1.	Modification of Calculation Method	132
7.7.2.	Effect of Processing Temperature	135

7.7.3. Effect of Air Flow Speed	136
7.7.4. Effect of Initial Fiber Velocity	139
7.7.5. Comparisons Between Experimental Results and Model Simulation Results	140
CHAPTER 8 Conclusions and Suggestions for Future Studies	143
8.1. Conclusions	143
8.2. Suggestions for Future Studies	144
APPENDIX A Drawing of Spinneret Pack	147
A.1. Spinneret Die	147
A.2. Air Chamber	148
A.3. Air Nozzle	149
A.4. Insulation Piece	150
APPENDIX B Picture of Fiber Extruder	152
APPENDIX C Matlab Codes for Theoretical Modeling	154
C.1. Validation Model	154
C.2. Isothermal Model	154
C.3. Non-isothermal Model	155
References	159



## LIST OF TABLES

Table 3-1 Air jet velocity comparisons.	31
Table 4-1 Materials properties of Polypropylene and air.	45
Table 5-1 First design of parametric studies on processing conditions.	60
Table 5-2 Second design of parametric studies on processing conditions.	62
Table 6-1 PP115 fiber diameters and their processing conditions.	71
Table 6-2 PP12 fiber diameters and their processing conditions.	72
Table 6-3 Crystallite size and $2\theta$ value of 110 plane of PP115 fiber made at 220°C.	87
Table 6-4 Melting and crystallization temperatures of resulting fibers.	92
Table 6-5 Fiber properties of fibers made by traditional melt spinning.	97
Table 6-6 Processing conditions and resulting fiber properties of Nylon-6 fibers.	101
Table 7-1 Value of $\beta$ and $n$ from literature [44].	109
Table 7-2 Material properties and processing conditions for the isothermal model with 5cm model geometry length.	125
Table 7-3 Material properties and processing conditions for non-isothermal case.	132
Table 7-4 Comparisons between experimental results and simulation results on final fiber diameter under various processing conditions.	141

## LIST OF FIGURES

Figure 1.1 A typical melt spinning setup.	2
Figure 1.2 Schematic of apparatus used for laser heating [8].	3
Figure 1.3 Schematic diagram of melt spinning with liquid isothermal bath. (a) The normal LIB process; (b) The modified LIB process [19, 20].	4
Figure 1.4 Illustration of the set-up used for the various types of spinline modification attempted: on-line zone cooling, on-line zone heating, on-line zone cooling and then heating [23].	5
Figure 1.5 Schematic of dry-spinning process [24].	6
Figure 1.6 Schematic of wet-spinning process [24].	7
Figure 1.7 Detailed schematic of the melt blowing die: (a) sectional and (b) end-on view of the two pieces [29].	8
Figure 1.8 Production line of nanofibrous materials [32].	9
Figure 1.9 Cohesive fracture of a steady-state liquid jet [24].	11
Figure 1.10 Break-up of a liquid jet due to capillary wave [24].	11
Figure 1.11 The individual contributions to spinning line tension vs. distance from spinneret [24].	12
Figure 1.12 The velocity profiles and gradient in (a) shear flow in a capillary, and (b) elongational flow in a spinline [51].	13
Figure 1.13 Comparison of shear and elongational viscosity functions vs. shear and tensile stress of polypropylene [52].	14
Figure 1.14 Variation of elongational viscosity with time at a constant elongational strain rate at 200°C for polypropylene. Elongational strain rate ( $s^{-1}$ ): ●0.6; ▲0.2; ■0.05; △0.02; ○0.005; □0.002 [53].	15
Figure 1.15 Formation of fiber structure in melt spinning [54].	15
Figure 1.16 Morphological models of polyethylene crystallization during melt spinning [55].	17
Figure 3.1 Mechanism of Laval Nozzle.	33
Figure 3.2 Boundary conditions for simulation.	34

Figure 3.3 Simulation results of static pressure, static temperature and Mach number.	35
Figure 3.4 Detailed schematic of the first design of cold air attenuation setup.	36
Figure 3.5 Detailed schematic of the second design of cold air attenuation setup.	37
Figure 3.6 Four different insulation plate designs.	38
Figure 3.7 Air flow velocity profile of in the air nozzle and with two different insulation plates shape.	40
Figure 3.8 Schematic of customized hydraulic piston-driven fiber extruder.	42
Figure 4.1 Model descriptions of geometry, sub-domains and boundary sets, where the SD1 and SD2 present polymer, while SD3 and SD4 present air.	44
Figure 4.2 Polypropylene viscosity dependence of shear rate at different temperature.	46
Figure 4.3 Polypropylene viscosity fitted by Cross law model at 180°C.	47
Figure 4.4 Polypropylene viscosity fitted by Arrhenius law model.	48
Figure 4.5 DSC test of virgin polypropylene.	49
Figure 4.6 Temperature ramp with angular frequency at 1 rad/s for polypropylene.	49
Figure 4.7 The velocity profiles and gradient in a spinline.	52
Figure 4.8 Effect of polypropylene viscosity on fiber geometries, (a) low viscosity; (b) medium viscosity and (c) high viscosity.	53
Figure 4.9 Fiber geometries and temperature profiles at different processing temperature: (a) 200°C; (b) 230°C and (c) 260°C.	55
Figure 4.10 Fiber geometries and temperature profiles at different air/polymer flow ratio: (a) low; (b) medium and (c) high.	57
Figure 5.1 Up: typical on-line ZZ polarized Raman spectra for polypropylene fibers with different draw ratios (A 1.5, B 2.5, C 3.0 and D 3.5); Bottom: Plot of draw ratio vs. the Raman intensity ratio and birefringence for the polypropylene fibers [94].	67
Figure 6.1 Viscosity of PP115 at different temperatures and angular frequencies.	69
Figure 6.2 Viscosity of PP35 at different temperatures and angular frequencies.	70
Figure 6.3 Viscosity of PP12 at different temperatures and angular frequencies.	70
Figure 6.4 Fiber diameter of PP115 and PP12 made at 220°C.	73

Figure 6.5 Data fitting of the relation between fiber diameter and air/polymer volume flow ratio.	74
Figure 6.6 SEM photographs of fibers.	76
Figure 6.7 Typical ZZ polarized Raman spectra of PP115 fibers, compared with WXRD pattern. Fibers were made with different draw ratio at different temperatures (a) 1600 at 220°C; (b) 330 at 220°C; (c) 360 at 240°C; (d) control (raw PP115 pellet).	78
Figure 6.8 PP115 fiber molecular orientation estimated by Raman spectra.	79
Figure 6.9 Crystallinity of resulting fibers made from PP 115 at different temperatures.	81
Figure 6.10 Crystallinity of resulting fibers made from PP 12 at different temperatures.	82
Figure 6.11 Wide-angle X-ray diffraction patterns of PP115 under various processing conditions. Inside the shaded box, the first number indicates the air/polymer flow ratio; the second one is the resulting fiber diameter.	85
Figure 6.12 WXRD spectra of typical PP115 fibers made at 220°C.	86
Figure 6.13 Typical stress-strain curves of single filament.	87
Figure 6.14 Tensile strength of PP115 fibers.	89
Figure 6.15 Tensile modulus of PP115 fibers.	90
Figure 6.16 Tensile strength of PP12 fibers.	90
Figure 6.17 DSC heating thermograms of PP115 fibers with different endotherm peak shapes.	93
Figure 6.18 WXRD spectra patterns of fibers with one or two melting peak(s) in DSC.	94
Figure 6.19 DSC heating thermograms of PP115 fibers made with various heating rate.	95
Figure 6.20 DSC heating thermograms of cold drawn and original undrawn PP115 fibers.	96
Figure 6.21 Viscosity of Nylon-6 at different temperatures and angular frequencies.	98
Figure 6.22 Nylon-6 fiber diameter versus air/polymer flow ratio.	100
Figure 6.23 Polarized microscopy image of Nylon-6 fiber.	100
Figure 7.1 Nu vs. Re in cooling by forced convection of cylindrical body; (●) data of Simmons; (○) data of Mueller; (△) data of Sano and Nishikawa; (□) Kase and Matsuo's work [57].	105

Figure 7.2 Comparison of the predictions of the 3D model with those of the 2D and 1D models [45].	113
Figure 7.3 Schematic of the melt spinning process by cold air attenuation and the force balance on fibers.	115
Figure 7.4 Model description of geometry and boundary conditions of freely fall down fiber in Polyflow.	121
Figure 7.5 Polyflow simulation results for freely fall down fiber model with different model geometry in length, (a) 3 cm, (b) 4 cm, (c) 5 cm and (d) 10 cm.	123
Figure 7.6 Comparison between the results obtained by Polyflow and MATLAB for different initial geometry length, 3 cm, 4 cm, 5 cm and 10 cm.	124
Figure 7.7 Isothermal model: fiber diameter profiles with different stop point positions (Inset: magnified view).	127
Figure 7.8 Isothermal model: fiber diameter profiles with different polymer viscosity with air flow velocity at 100 m/s (Inset: magnified view).	128
Figure 7.9 Isothermal model: fiber diameter profiles with different polymer viscosity with air flow velocity at 20 m/s.	129
Figure 7.10 Isothermal model: fiber diameter profiles with different initial fiber velocity (Inset: magnified view).	130
Figure 7.11 Isothermal model: fiber velocity profiles with different initial fiber velocity.	130
Figure 7.12 Isothermal model: fiber diameter profiles with different air flow velocity.	131
Figure 7.13 Non-isothermal model: fiber diameter and temperature.	133
Figure 7.14 Non-isothermal model: fiber diameter and temperature with processing temperature at 240°C and stop point position set at 5 cm.	135
Figure 7.15 Non-isothermal model: fiber diameter and temperature with processing temperature at 220°C and stop point position set at 4.5 cm.	136
Figure 7.16 Non-isothermal model: fiber diameter and temperature with air velocity of 10 m/s and stop point position set at 7 cm.	137
Figure 7.17 Non-isothermal model: fiber diameter and temperature with air velocity of 35 m/s and stop point position set at 5 cm.	137
Figure 7.18 Non-isothermal model: fiber diameter and temperature with initial fiber velocity at 0.01 m/s and stop point position set at 9 cm.	139

## LIST OF SYMBOLS AND ABBREVIATIONS

$h_c$	Heat transfer coefficient
$Nu$	Nusselt number
$k_a$	Thermal conductivity of air
$r$	Radius of fiber
$\pi$	Circumference ratio
$V_f$	Fiber velocity
$Q$	Polymer volume flow rate
$Re_D$	Reynolds number
$V_a$	Air velocity
$\rho_a$	Air density
$\mu_a$	Air viscosity
$\rho_f$	Polymer density
$C_{pf}$	Heat capacity of polymer
$T_f$	Fiber temperature
$\eta$	Polymer viscosity
$\eta_0$	Polymer zero shear rate viscosity
$T$	Fiber temperature
$g$	Gravitational acceleration
$C_f$	Air drag coefficient
cfm	Cubit feet per minute
$\tau$	Stress tensor

$F_{\text{ext}}$	Take up tension
$F_{\text{rheo}}$	Rheological force
$F_{\text{surf}}$	Surface tension
$F_{\text{aero}}$	Aerodynamic force
$F_{\text{gray}}$	Gravity
$P_{\text{xx}}$	Tensile stress
$P^*$	Fiber tensile strength
$A$	Cross-section area at nozzle exit
$A^*$	Cross-section area at nozzle throat
$\gamma$	Specific heat ratio
$P$	Air pressure
$M$	Mach number
MFI	Melt flow index
$\Delta n$	Birefringence
$M_n$	Number average molecular weight
PP	Polypropylene
PP115	Polypropylene with melt flow index of 115
PP35	Polypropylene with melt flow index of 35
PP12	Polypropylene with melt flow index of 12
iPP	Isotactic polypropylene
PA6	Polyamide-6
PA66	Polyamide-66
PLA	Polylactic acid
PET	Polyethylene terephthalate
LDPE	Low density polyethylene

SEM	Scanning electron microscope
DSC	Differential scanning calorimetry
DMA	Dynamic mechanical analysis
WXRD	Wide angle X-ray diffraction
CFD	Computational fluid dynamics
FEM	Finite element method



## SUMMARY

Melt spinning is the most convenient and economic method for polymer fiber manufacturing at industrial scales. In its standard setup, however, the thermomechanical history is often hard to control along the long spinline, resulting in poor controllability of the processing and fiber structure, and limited capability of producing very fine fibers. To address these process drawbacks, we developed and investigated an alternative melt spinning process where attenuation of continuous filaments is conducted solely by an annular high-speed cold air jet. This differs from the standard melt spinning process where filament stretching is driven by mechanical pulling force applied along the spinline. With the new process, the fiber is quenched by a symmetric cold air jet and simultaneously attenuated where an inverse parabolic velocity profile in molten fiber is expected. Since the formation of fiber structure is highly dependent on the process conditions, the new process will provide a unique and controllable operation window to study fiber attenuation and structural formation under high-speed cold air drawing.

Assisted by computational analysis on air/polymer fluid dynamics, we designed a high speed jet attenuation spinneret pack consisted of an extrusion die, an isolation plate, an air chamber, and an air nozzle. We built a piston-driven melt extruder, mounted to a hydraulic press and retrofitted with a single orifice extrusion die and the above described spinneret pack. The diameter of the die orifice was 0.5 mm. Parametric experimental studies were carried out to investigate effects of process variables on resulting fiber properties, including fiber diameter, molecular orientation, crystallinity and mechanical properties. Theoretical modeling was conducted to analyze the non-isothermal fiber attenuation mechanism under cold air drawing conditions.

Polypropylene was chosen as the polymer for the major part of the process study. The fibers produced by the new process showed a uniform diameter and a smooth surface appearance. The fiber diameter was found highly dependent on the polymer viscosity and processing conditions, including the processing temperature and the air/polymer flow ratio. The fiber diameter decreases with increasing of the air/polymer flow ratio and the processing temperature, and with decreasing of the polymer viscosity and the initial fiber velocity. Fibers with diameter of 7  $\mu\text{m}$  were produced from the 0.5 mm diameter spinneret, yielding an equivalent drawing ratio exceeding 5,000.

The molecular orientation of cold air attenuated fibers was found to increase with the increase of the air/polymer flow ratio. The maximum molecular orientation was observed at mild processing temperature (200-220°C). The measured fiber mechanical properties, in general, correlated well with the molecular orientation. The tensile strength and modulus increased with increasing of the air/polymer flow rate. Although no post drawing and heat setting steps were performed, the single filament with diameter of 10 $\mu\text{m}$  (without post drawing) showed moderately good mechanical properties, with a tensile strength of 100 MPa and a modulus of 2.5 GPa.

Orientation induced crystallization was found to be dominant in this new process. The fiber crystallinity increases with increase of the air/polymer flow ratio accompanied with formation of high molecular orientation. Low crystallinity fiber was associated with high processing temperature at relatively low air/polymer flow ratio. Only  $\alpha$ -monoclinic crystalline was formed in the produced polypropylene fibers.

For further demonstration, this process was also successfully applied to other polymer materials, including Nylon-6.

An isothermal Newtonian model was developed to analyze the single factor effect of processing conditions on fiber diameter. A non-isothermal model was implemented to predict the fiber diameter under different processing conditions. The predicted values compared favorably with the experimental data.

The new knowledge obtained in this study would likely yield a new process for producing innovative fiber products.

# **CHAPTER 1**

## **INTRODUCTION AND LITERATURE REVIEW**

### **1.1. Fiber Spinning Technology**

The first man-made fiber, known as viscose rayon, was invented by French scientist and industrialist Hilaire de Chardonnet in 1891. Since then, synthetic fibers have been largely used in the textile industry for apparel applications and as reinforcement for composite plastics [1]. Compared with natural fibers, synthetic fibers can be produced inexpensively, easily and in large volume. Among all the synthetic fibers, polymer fibers are a major subset, which are usually made from polyesters, polyamides and polyolefins. Traditionally, polymer fibers are made by a spinning process, including melt spinning, dry spinning and wet spinning. During fiber spinning, a polymer melt or solution is usually extruded through a spinneret and taken up downstream by a winder to form a filament. In 1950s, a melt blowing process was developed to produce nonwoven fabrics that contain fibers finer than normal textile fibers [2]. The ultra-fine fibers in nonwoven fibers/fabrics made by melt blowing supersede traditional fibers in many highly demanding applications, such as filtration systems, super absorbents and medical fabrics. Recent developments in bi-component spinning and electrospinning processes paved new ways to produce finer fibers for wider applications, including biomedical applications such as tissue engineering scaffolds [3, 4]. Among all these methods, melt spinning and melt blowing are still the most convenient and economic methods of fiber manufacture because of their high productivity, not requiring the use of auxiliary materials and simplicity of the process.

In conventional melt spinning, a melted polymer stream is ejected into a gas, usually air at ambient temperature (Figure 1.1). The gas performs the main function of cooling the filament, and it exerts a drag force upon the rapidly moving filament. Inside the capillary die, the polymer melt experiences mainly shear flow, while outside of the die flow changes to uniaxial elongational flow. When the polymer melt is extruded from the spinneret, it exhibits a die swell phenomenon. Then under the drag force applied by the winder, fiber starts to attenuate and chain orientation and crystallinity take place within a short time before melt solidification by the air cooling effect. The comparatively simple and easy processing is the most important advantage of melt spinning. However, it also suffers from problems like fiber breakdown, variation in filament thickness, and limit to the fineness of fiber and spinneret clogging.

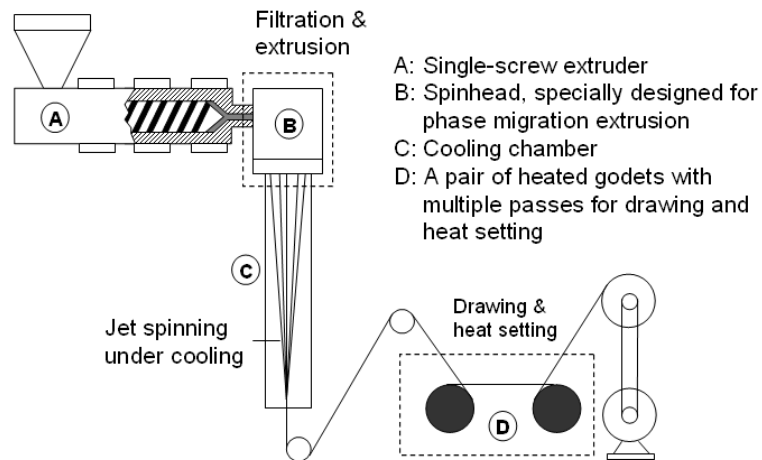


Figure 1.1 A typical melt spinning setup.

The mechanical properties of a filament can be improved by heat treatment of running filament in the spinline. For example, Suzuki et al. [5-18] developed a laser-thinning method to produce microfiber by irradiating a carbon dioxide (CO<sub>2</sub>) laser to fiber. One end of the zone-annealed fiber was connected to a jaw equipped with an

electric slider, whereas the other was attached to a slight weight. The zone-annealed fiber, moving downward at a speed of 500 mm/min, was heated by irradiating the CW CO<sub>2</sub> laser, and drawn instantaneously (Figure 1.2). The microfiber can be wound as a monofilament at winding speeds ranging from 100 to 2500 m/min. They have applied this method to PET, PA6, PP, PA66 and PLA fibers with diameter range of 1.5~5  $\mu\text{m}$ . Various fiber properties were improved by this process, such as tensile modulus, tensile strength and birefringence.

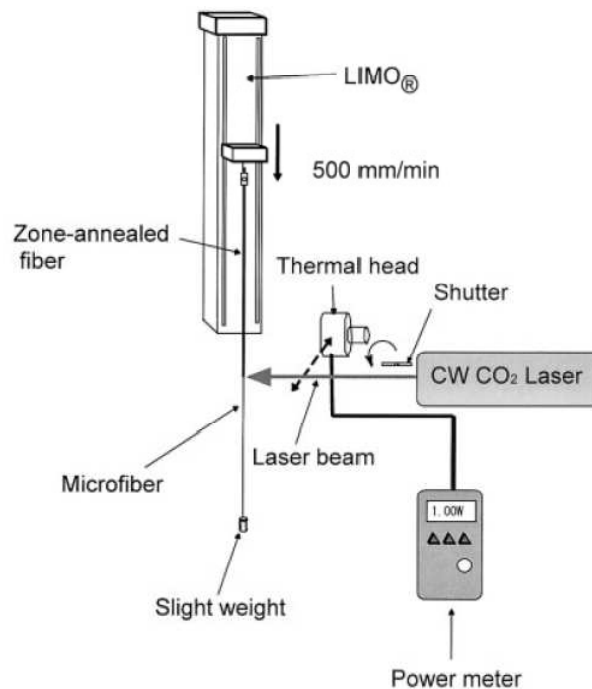


Figure 1.2 Schematic of apparatus used for laser heating [8].

A modified isothermal liquid bath was also used in melt spinning to produce high performance poly(ethylene terephthalate) fiber, reported by Cuculo et al. [19, 20]. In their experimental set-up (Figure 1.3), an isothermal liquid bath with temperature at 160°C is placed under the spinning orifice with different distance to develop an extremely high level of tension in the threadline. With this modification, as-spun fibers with extremely high amorphous orientation and low crystallinity can be produced. The resulting fibers

show good mechanical properties which is similar to those made by commercial spin-draw processes.

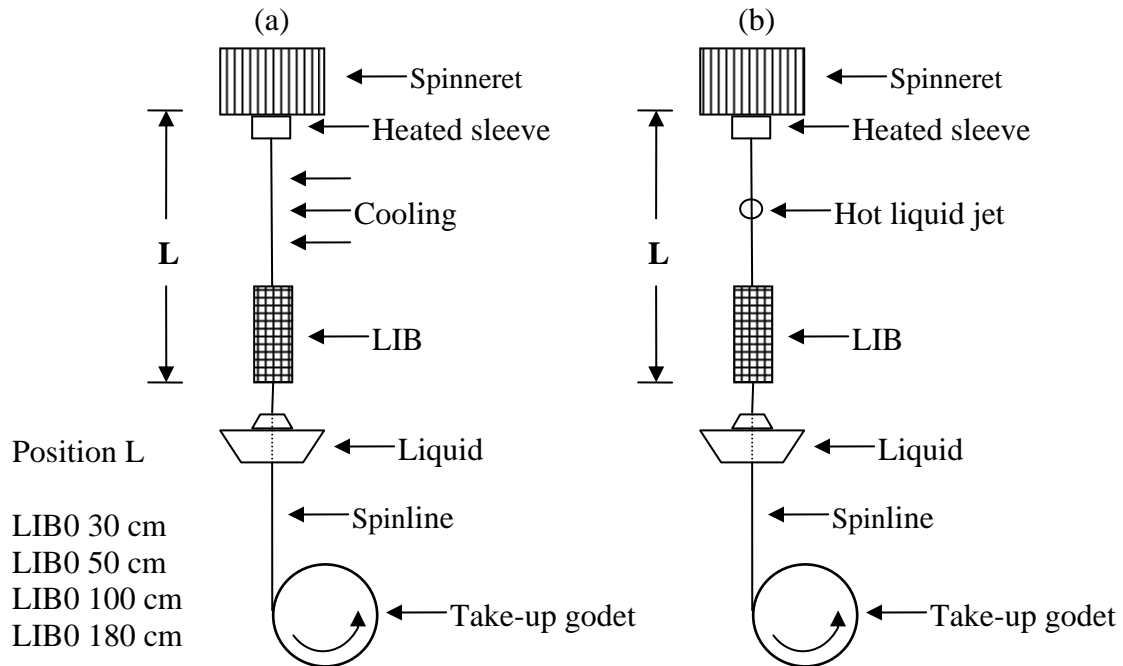


Figure 1.3 Schematic diagram of melt spinning with liquid isothermal bath. (a) The normal LIB process; (b) The modified LIB process [19, 20].

Some other efforts have been made to cool or quench filaments in the spinline to produce highly oriented amorphous yarn which is required for as-spun yarn to process into high tenacity yarn [21, 22]. In one of these methods, a liquid quenching medium is introduced. A highly oriented amorphous structure is formed by cooling the filaments in the spinline during high speed spinning. The effect of cooling bath position and temperature has been studied. Other than using a liquid quench bath, effect of modified air quenches on melt spinning process was also investigated [23]. As shown in Figure 1.4, a combination of enhanced and/or retarding air quenches is used to modify the threadline dynamics, resulting in significant improvement in spinning performance and as spun fiber

structure. With particular combination, produced fibers revealed high orientation and crystallinity, large crystal dimensions and greater mechanical properties. It was also claimed by the authors that this modified process can be applied to melt spinning over a wide range of take-up speeds.

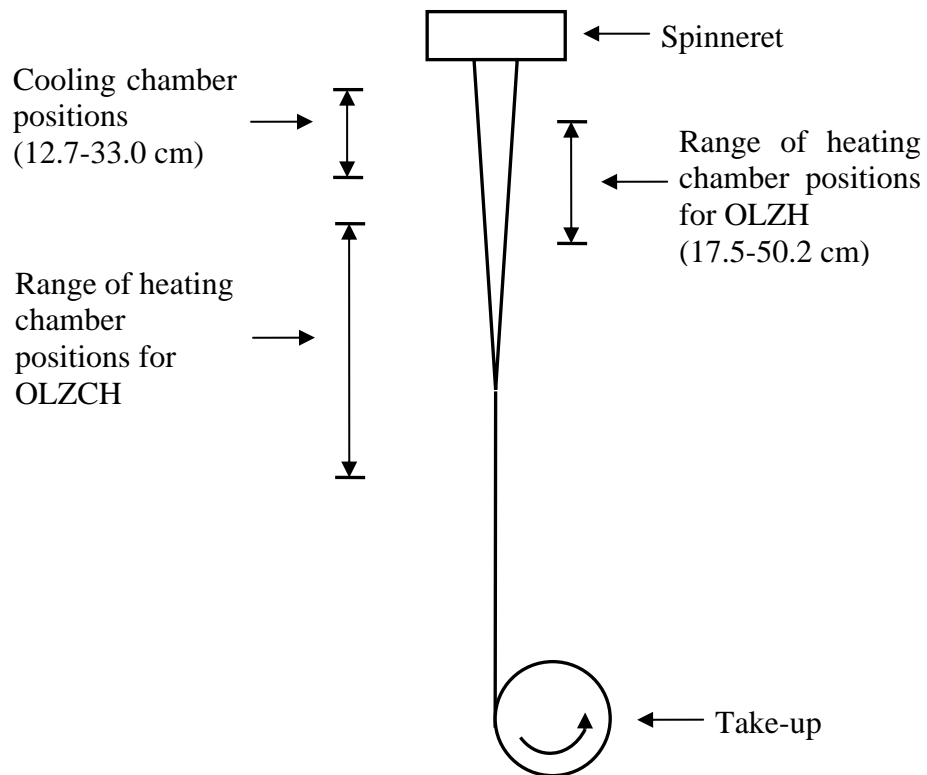
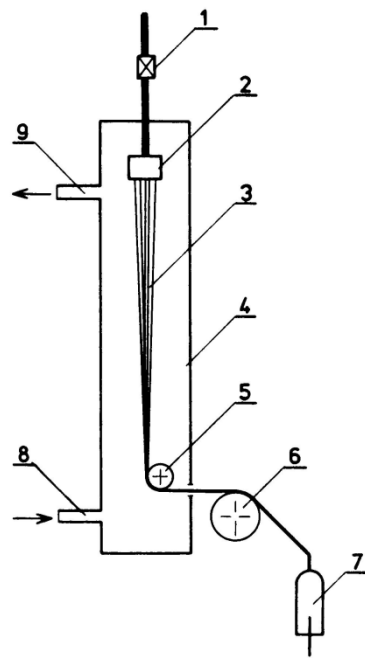


Figure 1.4 Illustration of the set-up used for the various types of spinline modification attempted: on-line zone cooling, on-line zone heating, on-line zone cooling and then heating [23].

Solution spinning is another method to make fiber if a suitable solvent can be found. Solution spinning can be classified primarily into two methods, dry spinning and wet spinning. The typical solution spinning processes are shown in Figure 1.5 and Figure 1.6. In dry spinning, the filament is formed by the evaporation of polymer solvent into air or an inert gas phase. The wet spinning is where a solution of a polymer is spun through a

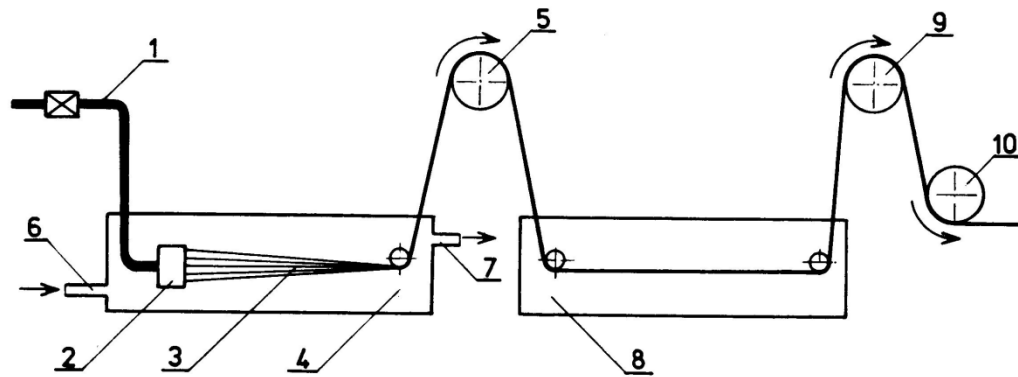


spinneret into a liquid which can coagulate the polymer. It can be further divided into three methods: the liquid-crystal method, the gel method and the phase-separation method. In the liquid-crystal method, a liquid-crystalline solution of a lyotropic polymer is solidified through the formation of a solid crystalline region in the solution. In the gel method, polymer solution is solidified through the formation of intermolecular bonds in the solution. In the case of phase separation, two different phases appear in the solution, one polymer-rich, and the other polymer-lean. However, the solution spinning process is too complicated and it is difficult to find the proper solvent for every polymer. Therefore, this method can only be applied for limit types of polymers to produce fibers, particularly when melt spinning is not a feasible process for these polymers.



1, metering pump; 2, spinneret; 3, spinning line; 4, drying tower; 5, 6, 7, take-up elements; 8 and 9, inlet and outlet of the drying gas.

Figure 1.5 Schematic of dry-spinning process [24].



1, inlet of the spinning dope; 2, spinneret; 3, spinning line; 4, spinning bath; 5, take-up godet; 6, 7, inlet and outlet of the spinning bath; 8, plasticizing bath; 9, 10, drawing elements.

Figure 1.6 Schematic of wet-spinning process [24].

For many years, melt blowing has been used for producing microfibers of finite length [25, 26]. In conventional melt spinning, a polymer stream is ejected into air at ambient temperature and pressure. However, the gas performs a very different task in melt blowing. A common feature for different melt blowing processes is that, in addition to spinning orifices, hot air nozzles are placed in the vicinity to draw the threads. Once mixed with the colder ambient air, there is simultaneous cooling and solidification and often the thread breaks. The original work on melt blowing dates back to the efforts of Naval Research Laboratory in the 1950s. Wentz [2] first described the construction of a melt blowing die composed of a number of orifices and slots. Motivation for his work was to make the submicron fibers for filters on drone aircraft. Based on the “slot” concept and an extension of sheet die technology, Exxon was able to improve Wentz’s work to a commercial production scale [27, 28]. Since then, a number of companies have used the technology to produce commercial nonwoven products. In general, these commercial products are composed of fibers with average diameters about 1-2  $\mu\text{m}$ .

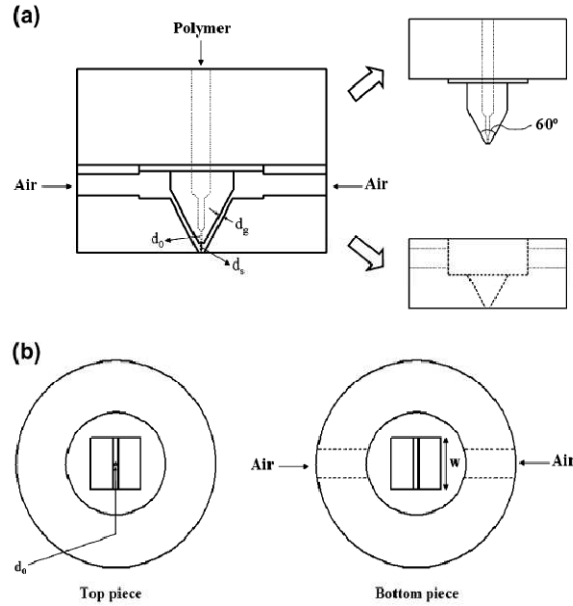


Figure 1.7 Detailed schematic of the melt blowing die: (a) sectional and (b) end-on view of the two pieces [29].

The limitations of melt blowing include the stochastic process dynamics, the high energy consumption and the very short length of the fiber produced. If the melt blowing technology can be extended to submicron fiber size, it would provide a much easier, faster, and cheaper alternative to ultra fine fiber industry. Hence, the major focus of melt blowing research is to extend the technology to nanofibers [29-31]. Poly(butylene terephthalate), polypropylene, and polystyrene nanofibers with average diameters less than 500 nm have been produced by Ellison et al. [29] using a single orifice melt blowing apparatus (Figure 1.7) and commercially viable processing conditions. Furthermore, analysis of fiber diameter distributions reveals they are well described by a log-normal distribution function regardless of average fiber diameter, indicating that the underlying fiber attenuation mechanisms are retained even when producing nanofibers. Fiber breakup was observed under certain processing conditions, which was believed driven by

surface tension and these instabilities may represent the onset of an underlying fundamental limit to the process.

Podgorski et al. [32] developed a modified melt-blown technology, which facilitated the production of filters composed of micrometer as well as nanometer sized fibers. The schematic of the set up for obtaining fibers by blowing a melted polymer and details of the die construction are shown in Figure 1.8 (a polymer stream is denoted there by 1 and the air stream by 2). The processing conditions and the die orifice diameter were not reported.

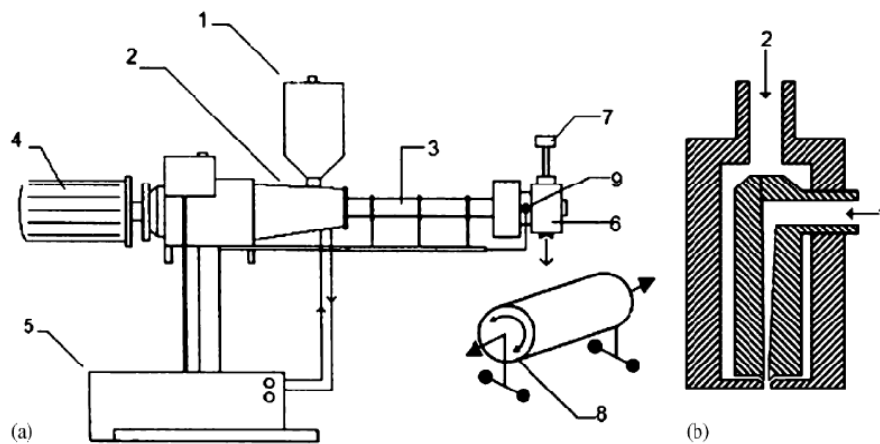


Figure 1.8 Production line of nanofibrous materials [32].

The research group in University of Oklahoma conducted a series of studies on melt blowing process, including the effect of die shape on air flow profile, filament motion and CFD simulation [26, 33-50]. A sharp and a blunt die are designed and studied in their paper. The results show that the blunt die is a better option to reduce turbulence fluctuation along the path of the polymer fiber.

In summary, melt blowing is typically used to produce nonwoven fabrics and usually the fiber strength is low. To make continuous filaments, melt spinning and solution spinning are the two major processes. Since solvent is introduced to dissolve the polymer,

solution spinning requires a relative complicated manufacturing set up and limits its application in industry. Therefore, the melt spinning process draws lots of interests in research to improve the fiber properties by modifying the spinline thermal and mechanical conditions as indicated in the literature. The mechanisms of how the processing conditions affect fiber properties will be discussed in the next sections.

## **1.2. Fundamental of Melt Spinning**

### **1.2.1. Tension in Melt Spinning Line**

Fiber breakage is the major issue in melt spinning. The physical mechanisms of the fiber breakage can be explained by two types of processes, cohesive failure and capillary wave breakage. In the first process, rupture occurs when the tensile stress in a polymer fiber exceeds some critical limit, the tensile strength. As shown in Figure 1.9, from the spinneret, initially the tensile stress ( $P_{xx}$ ) is lower than the fiber tensile strength ( $P^*$ ). Downstream along the spinline, both the tensile stress and fiber strength increase, but the tensile stress increases much faster than the tensile strength. At some critical point, the tensile stress will exceed the fiber tensile strength, thus resulting in fiber breakage. The second process, capillary wave breakage, is associated with surface tension. As shown in Figure 1.10, a polymer melt splits into individual drops when the growing amplitude of the capillary waves reaches the radius of the undistorted jet.

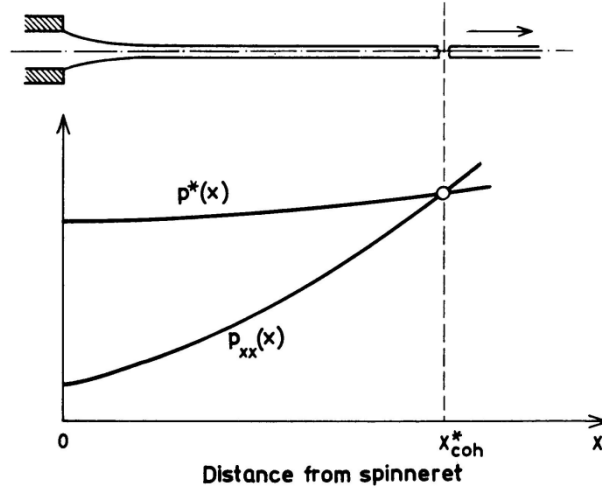


Figure 1.9 Cohesive fracture of a steady-state liquid jet [24].

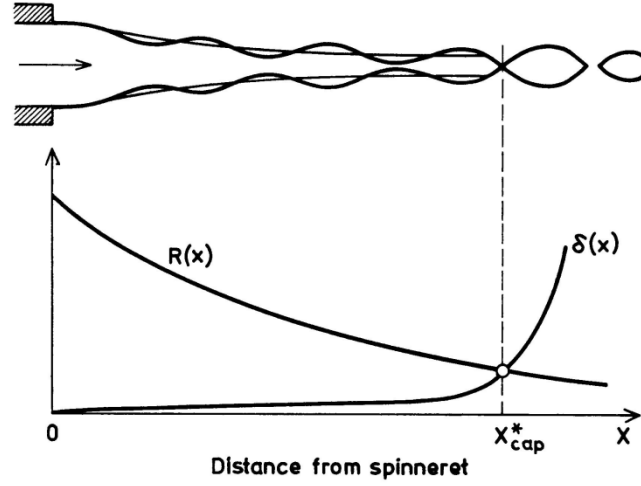


Figure 1.10 Break-up of a liquid jet due to capillary wave [24].

Integration of the momentum conservation equation yields the following equation of force balance at a distance  $x$  from the spinneret:

$$F_{ext} + F_{grav}(x) = F_{rheo}(x) + F_{in}(x) + F_{surf}(x) + F_{aero}(x). \quad (1)$$

$F_{ext}$ ,  $F_{grav}$ ,  $F_{rheo}$ ,  $F_{surf}$ ,  $F_{in}$  and  $F_{aero}$  represent take-up tension, gravity, rheological force, surface tension, inertia and aerodynamic force. Figure 1.11 illustrates the distribution of

individual force contributions along the spinline of a Nylon 6 monofilament [24]. Compared with other forces, the surface tension can be neglected as being less than 1% of the take up tension. Gravity and inertia provide an appreciable effect on the filament tension near the spinneret and then keep decreasing downstream the spinline. Aerodynamic and rheological forces are the major forces balancing with take up tension along the spinline. The take up tension is assumed to be constant along the spinline in normal spinning speed. At higher spinning speed, the aerodynamic force plays a dominant role thus the assumption of constant force along the spinline is not valid.

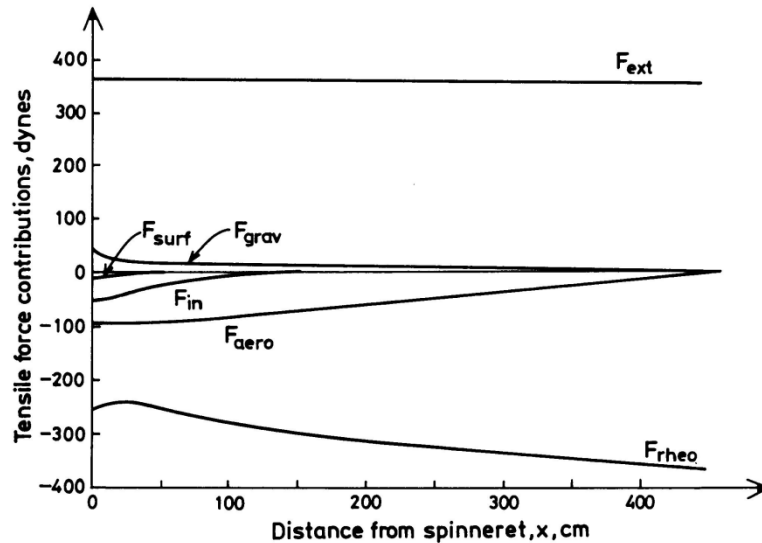


Figure 1.11 The individual contributions to spinning line tension vs. distance from spinneret [24].

### 1.2.2. Kinematics of Melt Spinning

The velocity distribution and profile of the polymer melt appear in different forms along the spinline, which play an important role in the fiber formation. Inside the spinneret channel, the polymer flow is a typical Poiseuille flow with a parabolic velocity

profile. By assuming an incompressible Newtonian liquid of viscosity  $\eta$  through a capillary of radius  $R$  and length  $L$ , the radial velocity distribution can be described as:

$$V(r) = \frac{P}{4\eta L}(R^2 - r^2), \quad (2)$$

where  $P$  is the pressure difference between the inlet and outlet of capillary.

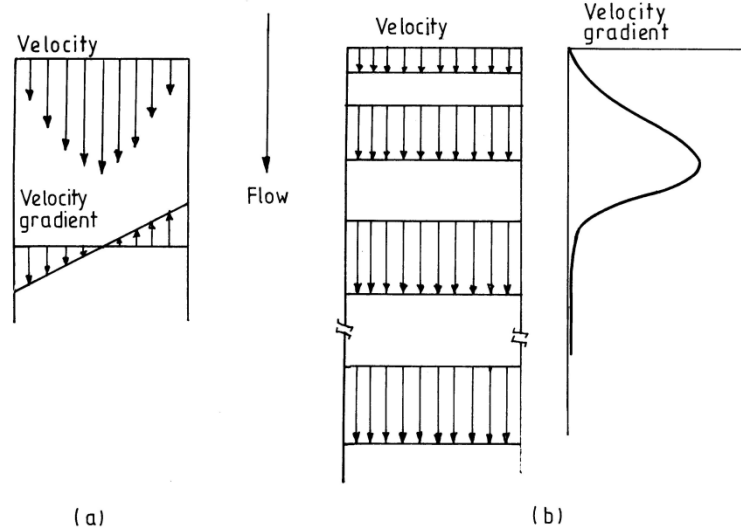


Figure 1.12 The velocity profiles and gradient in (a) shear flow in a capillary, and (b) elongational flow in a spinline [51].

When polymer is extruded out the orifice, a phenomenon of die swell is observed due to the relaxation of stored elastic energy. The degree of swelling depends on the conditions of extrusion, temperature and geometry of the die. For example, in melt spinning, the die swell ratio decreases with the increase of extrusion temperature. Under take up tension, the flow of polymer melt transits from shear flow to elongational flow, or uniaxial extensional flow. In elongational flow, the velocity keeps increasing along the spinline and finally reaches the take-up speed. Figure 1.12 shows the differences on velocity profile between shear flow and elongational flow.



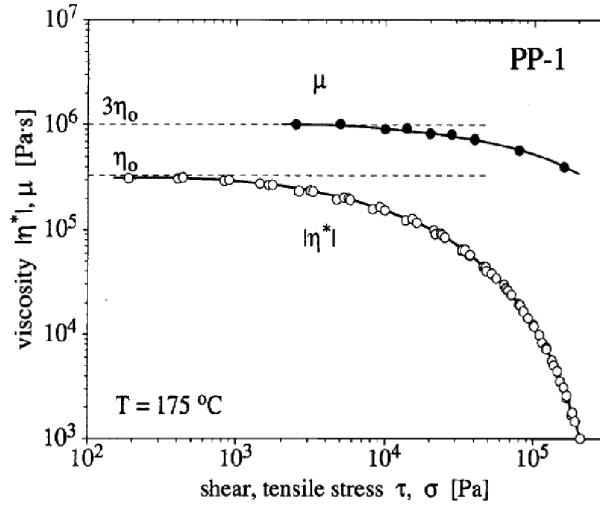


Figure 1.13 Comparison of shear and elongational viscosity functions vs. shear and tensile stress of polypropylene [52].

The fiber formation occurring underneath the spinneret is affected by elongational viscosity  $\eta^*$  over a wide range of temperatures. In a steady state elongation, the elongation viscosity  $\eta^*$  is nearly constant and equal to 3-times Newtonian viscosity  $\eta_0$  (the so-called Trouton's viscosity model) in the range of moderate elongation rate:

$$\eta^* = 3\eta_0. \quad (3)$$

When the elongational rate exceeds some critical value, the elongational viscosity deviates from the  $3\eta_0$  model for a Newtonian liquid because of the dominating elastic deformation. The typical shape of the elongational viscosity as a function of tensile stress for polypropylene melts is shown in Figure 1.13. For small stress, the elongational viscosity fits the threefold value of shear viscosity. When the stress increases, the shear viscosity decreases more abruptly than the elongational viscosity.

In highly viscoelastic materials such as molten polypropylene, steady state elongational flow is not possible at higher elongational rate because the rapid increase of tensile stress is followed by cohesive fracture. Figure 1.14 shows the time dependent

elongational viscosity of polypropylene. At low elongational rate, the elongational viscosity increases smoothly and finally reaches the constant value  $3\eta_0$ . For higher elongational rate, the elongational viscosity increases dramatically once beyond the critical time. The critical time also decreases with increasing elongational rate.

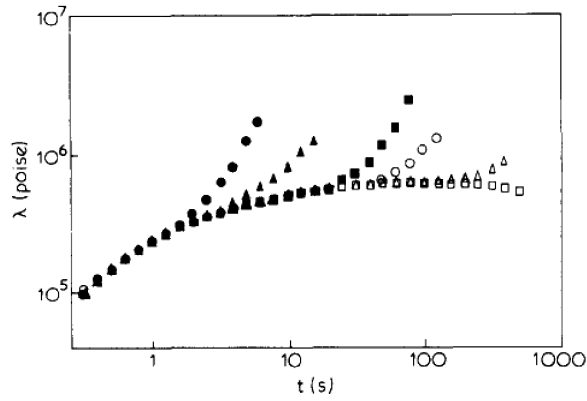


Figure 1.14 Variation of elongational viscosity with time at a constant elongational strain rate at 200°C for polypropylene. Elongational strain rate ( $\text{s}^{-1}$ ): ● 0.6; ▲ 0.2; ■ 0.05; △ 0.02; ○ 0.005; □ 0.002 [53].

### 1.2.3. Formation of Fiber Structure

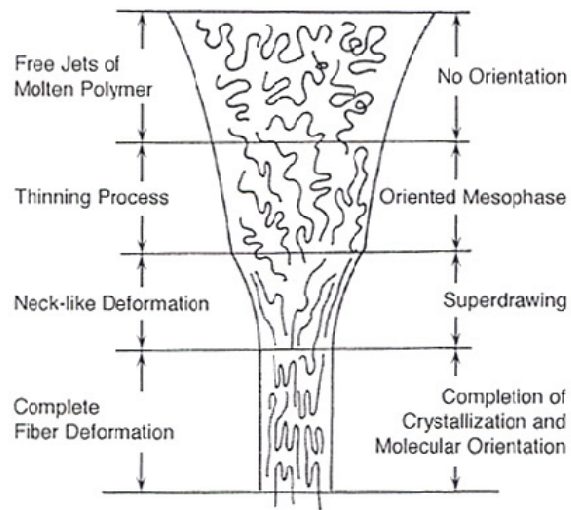


Figure 1.15 Formation of fiber structure in melt spinning [54].

Formation of molecular orientation and crystalline plays an important role in melt spinning and thus affects the ultimate structure and physical properties of fibers. Figure 1.15 describes a typical fiber structure formation process in melt spinning.

Molecular orientation arises from parallelization of the molecular chains along the fiber axis in both the crystalline and non-crystalline regions. During melt spinning, the molecular orientation develops in two stages: in spinneret channel and under elongation. Molecular alignment is developed when the polymer melt is forced through a capillary channel. As it comes out of the spinneret, the molecular alignment becomes disorientated and thus contributes very little to the final fiber orientation. The major contribution of orientation is made by the elongational flow along the spinline. The parallel velocity gradient, the relaxation time distribution and the elapsed time are the important factors which affect the molecular orientation. For example, a higher heat transfer coefficient results in an increase in orientation since it causes more effective freezing of orientation on filament quenching. The molecular orientation also increases with the increase in take-up speed, extrudate viscosity and reciprocal of polymer mass flow rate.

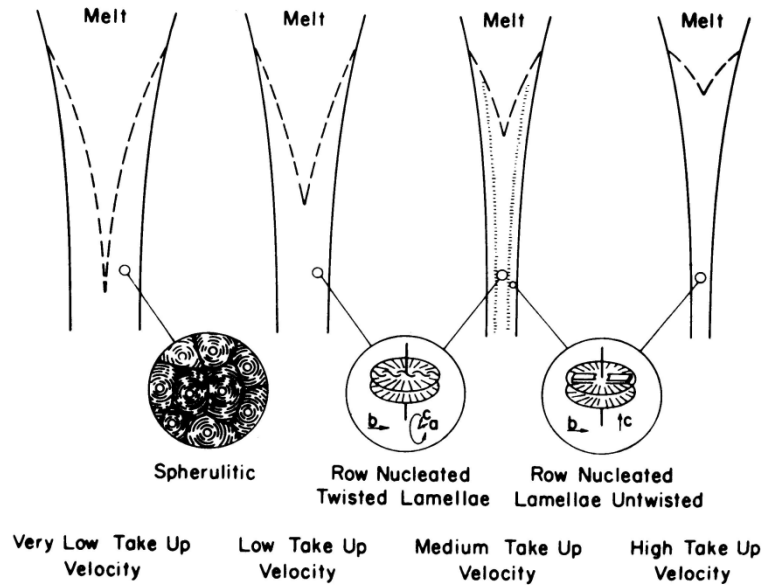


Figure 1.16 Morphological models of polyethylene crystallization during melt spinning [55].

Non-isothermal and oriented crystallization of the filament is also developed during melt spinning, and the oriented crystallization plays a privileged role in fiber formation. It was observed by Keller [56] that during elongation, the nuclei are formed along the spinline in the form of platelets known as row nucleation. With the increase of take-up speed, the morphological forms of crystallization alter from spherulitic to row nucleated twisted lamellae, and finally to row nucleated lamellae untwisted. A morphological model of melt spun PE proposed by Dees and Spruiell [55] is shown in Figure 1.16. The crystallization is also very sensitive to the spinning conditions. In contrast to orientation, crystallinity decreases with the increase of heat transfer coefficient and increases with the increase of fiber diameter since slow cooling gives more time for molecules to crystallize.

#### **1.2.4. Numerical Simulations**

Since the early 1960s a number of researchers have started to analyze the dynamics of melt spinning by establishing a set of simultaneous partial differential equations over a wide range of spinning conditions. Kase et al [57, 58] studied the axial and radial variations in temperature and velocity of steady spinline, and stability of unsteady spinline using multi-part study. A 3-D axisymmetric temperature profile in a constant radius fiber has been solved by Morrison in 1969 [59]. Moutsoglou [60] studied the temperature field subjected to an exponential stretching rate. The numerical analyses of melt spinning were also extended from isothermal Newtonian flow to viscoelastic fluid, nonisothermal Newtonian flow, nonisothermal viscoelastic flow and recently flow with crystallization [61-64].

### **1.3. Fundamental of Melt Blowing**

Melt blowing is a one step process for producing nonwoven fabrics from polymer melt with high speed hot air attenuation. The microfibers made by melt blowing usually have diameters in the range of 2 to 4  $\mu\text{m}$  with very short length. The basic product properties include random fiber orientation, web strength, fiber diameter and filtration characteristics. Most of the efforts in this area focused on optimization of process conditions for improving those product properties [38, 65-69]. Unlike the melt spinning process, fundamental studies of melt blowing are seldom reported except some numerical modeling studies. The interest in the development of a numerical model for the melt blowing process dates back to 1990s. Uyttendaele and Shambaugh [70] developed a 1-D model by assuming fiber motion only in the axial direction. Their model can successfully predict the fiber attenuation under the action of the hot air steam within relatively low

spinning speeds. Rao and Shambaugh [71] expanded the 1-D model to a 2-D model in which the fiber motion is considered in a plane. Recently, a 3-D model involving the simultaneous solution of the momentum, energy and continuity equations has been developed by Marla and Shambaugh [45]. Other relevant numerical models of melt blowing have also been investigated by a number of researchers, such as simulation of the fiber movement, air-jet flow field and air drawing [39, 40, 72]. Details on these numerical models will be discussed later.

#### **1.4. Crystallization Behavior of Isotactic Polypropylene**

Isotactic polypropylene (iPP) is a widely used polymer material in the fiber industry because of its ease of processing, low cost and rapid crystallization. The crystallization process of iPP is complicated, sensitive to the processing conditions. A less ordered mesophase can be formed at high cooling rate and low orientation. The crystalline structure usually results from low cooling rate and modest to high orientation.

##### **1.4.1. Mesophase Structure**

Boye et al. [73] reported a smectic structure observed on a melt-extruded isotactic polypropylene quenched in ice water. The sample density was 0.882 g/ml which is higher than the amorphous polypropylene. In addition, two broad peaks located at  $2\theta=14.8^\circ$  and  $21.3^\circ$  were exhibited in the X-ray diffraction spectra.

Choi and White [74] studied the effect of cooling rate and spinline stress on the formation of different crystalline forms. The sample filaments were prepared by melt spinning at various melt temperatures and take-up speeds. The filaments were quenched by either ice water or ambient air before taken up by roller. Smectic structures were only detected on the filaments quenched by ice water. It was also observed that the smectic

structure transits to  $\alpha$ -monoclinic crystalline structure with increasing of draw-down ratio and spinline stress at melt temperature 200°C and 230°C. However, this transition was not observed when melt temperature increased to 260°C. They also developed continuous cooling transformation (CCT) curves and a map of crystalline form as a function of cooling rate and spinline stress. The CCT curves and the map were then used to predict the formation of cross-sectional variation structure in thick filaments and rods.

Gorga et al. [75] studied the meso-to- $\alpha$  phase transition in iPP made from quenching and melt spinning for two different polypropylene (iPP<sub>E</sub> and iPP<sub>S</sub>) with similar molecular weight profile. The iPP<sub>S</sub> melt spun fibers showed mesophase structure when the take-up speed is in the regime of 100-1000 m/min. This range changed to 30-1000 m/min for iPP<sub>E</sub> for the formation of mesophase. When the take-up speed exceeds 1500 m/min, the  $\alpha$ -monoclinic structure was redeveloped for both iPP<sub>E</sub> and iPP<sub>S</sub> melt spun fibers. The mesophase structure was also observed in the non-oriented iPP<sub>E</sub> sample quenched by ice-water. However, the mesophase was not formed for iPP<sub>S</sub> even when it was quenched by liquid nitrogen, the hardest quenching conditions used in their study. It was indicated that the molecular orientation increases with increasing take-up speed for all crystalline, mesophase and amorphous structures. Mechanical properties showed strong relation with molecular orientation, but it is unrelated with the presence of mesophase.

#### **1.4.2. Crystalline Structure**

The crystalline phase of isotactic polypropylene has three kinds of crystalline forms:  $\alpha$ -monoclinic,  $\beta$ -hexagonal and  $\gamma$ -triclinic. iPP predominately crystallize in  $\alpha$ -monoclinic under usual conditions. For example, iPP fibers made by melt spinning usually exhibits  $\alpha$ -monoclinic crystalline structure. The  $\beta$ -hexagonal and  $\gamma$ -triclinic crystalline can be

formed under extreme conditions or by introducing nucleating agents. The three different crystal forms can be characterized by X-ray diffraction method. For  $\alpha$ -monoclinic, it shows three strong reflections located at  $2\theta=14.2^\circ$ ,  $17.1^\circ$  and  $18.6^\circ$  which correspond to 110, 040 and 130 plane respectively.  $\beta$ -hexagonal has a strong peak in X-ray diffraction spectra located at  $2\theta=16.1^\circ$  which represents 300 plane. For  $\gamma$ -triclinic, the 100, 040 and 130 planes show strong reflection at  $2\theta=13.9^\circ$ ,  $16.8^\circ$  and  $20.1^\circ$ .

Broda [76] observed the formation of  $\beta$ -hexagonal crystal in iPP fibers made by melt spinning with the addition of quinacridone pigment. In this paper, the crystallization behavior was compared for colored and noncolored fibers melt spun under various conditions. In noncolored fibers, the mesophase was observed for modest take-up velocity and  $\alpha$ -monoclinic was formed at low or high take-up velocity. The content of mesophase was found increased at higher melt temperature because of low orientation and high cooling rate. In colored fibers, the  $\beta$ -hexagonal was observed at low take-up velocity for both low and high melt temperature. When the take-up velocity increases, the content of  $\beta$ -hexagonal crystalline became smaller and finally transitioned to a crystalline structure with only  $\alpha$ -monoclinic. This transition was explained by the marginal nucleating effect of the pigment at high take-up velocity where the crystallization is governed by the orientation.

Al-Raheil et al. [77, 78] studied the spherulitic structure of isotactic polypropylene from melt by polarized light and SEM. Their results showed that  $\alpha$  and  $\beta$  spherulitic can be obtained for crystallization from melt below  $132^\circ\text{C}$ . Above  $132^\circ\text{C}$ , only  $\alpha$  type spherulitic was observed for isothermal crystallization. Their study also indicated that  $\alpha$  spherulitic has a more complicated crosshatched lamellar structure than  $\beta$  spherulitic.



$\gamma$ -triclinic crystalline structure is very difficult to form under normal conditions. Wittmann and Lotz [79] reported the formation of  $\gamma$ -phase crystal obtained from low molecular weight extracts of pyrolyzed iPP crystallized from melt. Several major differences from  $\alpha$ -phase crystal were claimed in their study. The  $\gamma$ -phase crystal elongates along the  $b^*$ -axis direction with chain axis inclined at  $50^\circ$  to the lamellar surface. And the screw dislocations were found for  $\gamma$ -phase crystal. Shen and Li [80] studied the  $\beta$ - and  $\gamma$ -form distributions of iPP injection molding controlled by melt vibration. The  $\beta$ -form crystals were obtained in injection-molded iPP by either conventional injection molding or vibration-assisted injection molding. The content of  $\beta$ -form crystals can be controlled by applying different vibration modes. The  $\gamma$ -form crystals can only be obtained under relatively low vibration frequency and large vibration pressure amplitude.

#### **1.4.3. Two Melting Endotherm Peaks**

It was reported that sometimes isotactic polypropylene has two melting endotherms in its DSC thermograms. Different theories have been proposed to explain this melting behavior, such as formation of two different crystal structure and crystalline size, recrystallization and reorganization during the heating in DSC scan.

Somani et al. [81] studied the orientation-induced crystallization in iPP melt by shear deformation. The DSC thermograms of sheared iPP samples showed two melting peaks: one at  $164^\circ\text{C}$  and the other at  $179^\circ\text{C}$ . Further investigations suggested that the first peak corresponds to the nominal melting of the unoriented spherulites consisting of folded chain crystal lamellae. And the second one is from the melting of oriented crystalline structures.

Yan and Jiang [82] investigated the effect of drawing condition on the observed properties of drawn, compression-molded isotactic polypropylene. The iPP pellets were firstly melted and compression-molded to sheets at 195°C. The sheets were then cooled naturally under pressure. An Instron tensile testing machine was used to draw the sheet under various temperatures and draw ratios. For the sample with high draw ratio and high heating rate used in DSC, it was observed two melting endothermic peaks in DSC thermograms. The position of the two melting peaks was found influenced by drawing conditions. The peak at lower temperature is related to the drawing ratio and temperature, while the peak at higher temperature only depends on the draw ratio. All the tested samples exhibited typical  $\alpha$ -form crystalline in X-ray diffraction pattern. They assumed that the peak at lower temperature comes from extremely thin quasi-amorphous or crystalline layers among neighboring microfibrils, whereas the peak at higher temperature comes from the lamellar crystals within microfibrils.

Kim et al. [83] conducted a study on melting of isotactic polypropylene isothermally crystallized at different temperatures. Double melting peaks were observed for crystallization temperature in the range of 110°C to 140°C. The double melting peaks are contributed from two preexisting crystal fractions with different  $T_m$ . Pae and Sauer [84] studied the effects of thermal history on isotactic polypropylene. A double endothermic peak was observed after a series of stepwise annealing treatments when the final annealing temperature is close to 160°C.

Jain and Yadav [85] studied the melting behavior of isotactic polypropylene isothermally crystallized from melt. The development of the multiple fusion endotherms was investigated based on different crystallization temperature. The crystal imperfections

play an important role with crystallization temperature at or lower than 127°C. Under heating, the crystallized fraction recrystallized to a fraction with higher degree of perfection which has higher melting temperature. When the crystallization temperature increases, the crystallization rate decreases. The higher melting peak starts to disappear and finally merges with the lower melting peak to a single peak at  $T_c=127^\circ\text{C}$ . At crystallization temperature higher than 127°C, the multiple peaks were attributed to the existence of different crystalline species with different crystal disorder and stereo-block character.

Qudah et al. [78] also observed double melting peaks on DSC curves when the isotactic polypropylene crystallized isothermally above 132°C at which only  $\alpha$ -monoclinic crystalline was formed. It was concluded that the peak at low temperature comes from the melting of crosshatched lamellae of  $\alpha$ -monoclinic crystalline, while the other peak is related to melting of the radial and the reorganized tangential lamellae. Guerra [86] discovered two different modifications of  $\alpha$ -monoclinic crystalline by annealing which has difference in order. The recrystallization from less ordered modifications to more ordered ones results in a large increase of melting temperature which leads to the double peak of melting endotherm.

Aboulfaraj et al. [86] observed double peaks in melting endotherm for a thick plate of isotactic polypropylene. The appearance of double melting peaks was attributed to the formation of different crystal forms,  $\alpha$ -monoclinic and  $\beta$ -hexagonal phases. A distribution of  $\alpha$  and  $\beta$  crystal forms was developed by a slow solidification process. The  $\alpha$  form crystal was found dominant on the surface and coexisted with  $\beta$  form crystal inside the

plate. The portion of  $\beta$  form crystal changes from 0 to 60% from the surface to the core of the sample plate.

#### **1.4.4. Effect of Processing Temperature and Take-up Speed on Crystallinity in Melt Spinning**

As summarized in the previous part, the crystallization of polymer during melt spinning is a complex process which is governed by many competing factors. It was reported by Cao et al. [87] that the polypropylene crystallization behavior is influenced by two main competing factors, cooling rate and crystallization rate. In their studies, two kinds of polypropylene with different melt index values were used to produce fibers by melt spinning process. The experiments were conducted at different temperatures with various take-up velocities. The fiber crystallinity was characterized in terms of density and the relation between fiber crystallinity and take-up velocity was studied. At high processing temperature (270°C and 290°C), the crystallinity firstly decreases and then increases with the increase of take-up speed. However, at low processing temperature (210°C and 250°C), the crystallinity keeps constant which does not change with the take-up velocity. This phenomenon was explained by the concept of competitive effect of cooling rate and crystallization rate. Both the cooling rate and crystallization rate increase with the increase in take-up velocity. At low take-up velocity, the cooling rate dominates the crystallization process since the spinline stress is low. Therefore, the crystallinity decreases with increasing take-up velocity. However, when take-up velocity increases to some point, the crystallization rate becomes dominant in the crystallization process due to the increasing spinline stress and high orientation. Consequently, the fiber crystallinity starts to increase with increasing take-up speed.

#### **1.4.5. Effect of Cooling Rate on Crystallinity**

Crystallization of polymer under varied processing conditions is a very complicated process and cannot be described by any single-valued effect, because it is not possible to separate the thermodynamics from kinetics effects during the process. Piccarolo et al. [88] developed a specially designed experimental setup which can independently study the effect of cooling rate on polymer crystallization. The cooling rate covers an overall variation from 0.01-1000°C/s. It can be controlled by changing the coolant, flow rate, temperature, or the sample thickness. The crystallization behavior of iPP, PET and PA6 were studied. The crystallinity was characterized in terms of density. A dramatic decrease in iPP density was found when the cooling rate reaches about 100°C/s. This critical cooling rate decreases to 10°C/s and 2°C/s for PA6 and PET respectively. After the critical point, the polymer density remains almost at a constant value depending on the final phase structure. A mesophase to  $\alpha$ -monoclinic phase transition was observed in iPP samples when the cooling rate is above 100°C/s.

## **CHAPTER 2**

### **RESEARCH MOTIVATIONS AND OBJECTIVES**

Melt spinning is the most convenient and economic method for polymer fiber manufacturing at industrial scales. In its standard setup, melt spinning involves mechanical stretching of polymer filaments both in a liquid and in a solid state. However, this process is subjected to some inherent process flaws. Particularly, the process is operated in a relatively narrow process window, mainly designed for stretching the filament with a constant tensile force and cooling the filament using cross air flow. Because a constant tension is applied during fiber extenuation, the tensile stress rapidly increases along the spinning line. This can cause instabilities and difficulty in producing fine fibers. More importantly, the thermomechanical history is often hard to control in this narrow process window, resulting in poor controllability of the process and the fiber structure.

As discussed in the literature review, some efforts have been made in modifying the spinline thermal and mechanical dynamics to improve fiber properties or produce finer fibers. One approach is to heat the spinline by hot air or laser, such as melt blowing and melt spinning with online laser heating. With the increase of spinline temperature, the filaments tend to be attenuated more and usually finer fibers can be achieved. However, the fibers created from melt blowing are typically discontinuous with short fiber length. The online laser heating process also needs specially designed equipment and post drawing process to achieve high fiber strength. Another approach is to apply a liquid bath on the spinline to increase the spinline stress and control the filament temperature. With

this modification, highly orientated highly crystalline fibers or highly orientated amorphous fibers can be obtained dependent on the liquid bath conditions. However, the complex setup and processing procedure make it impossible for massive industry production. Therefore, it is highly desirable to develop a new process to produce continuous filaments with modified spinline thermal and mechanical environment. In addition, this process should satisfy the requirements of industrial production, such as easy setup, stable process, environmental friendliness, solvent free process, and mass productivity.

To achieve these purposes, we investigated and developed a modified melt spinning process with an annular high-speed jet nozzle to produce continuous polypropylene filaments by cold air drawing only. With this setup, the fiber emerged out of the die orifice is quenched and simultaneously attenuated by a symmetric cold air jet. Since the formation of fiber structure is highly dependent on the processing conditions, the new process will provide a unique operation window to study fiber attenuation and structural formation under high-speed cold air drawing. The new knowledge obtained in this study would likely yield a new process for producing innovative fiber products.

With these motivations, the specific objectives of the project are to:

- Design and build a high speed air jet nozzle.
- Retrofit a melt-spinning unit with a specially designed spinneret and high speed air nozzle.
- Study the non-isothermal fiber attenuation mechanisms by computational fluid dynamics method. Based on the simulation results, perform a parametric study under different process conditions which include processing temperature, air velocity and

polymer volume flow rate.

- Investigate the relationships between the process conditions and resulting fiber properties, such as fiber geometry, orientation, crystallization, thermal and mechanical properties.
- Build a mathematical model to theoretically study the fiber attenuation mechanisms, mainly on how the resulting fiber geometry is affected by the polymer melt temperature, the polymer/air throughput ratio, and the polymer viscosity. Also use this model to predict the final fiber diameter.



# **CHAPTER 3**

## **DESIGN OF APPARATUS FOR MELT SPINNING BY COLD AIR ATTENUATION**

An annular single orifice melt spinning equipment at laboratory scale was assembled to produce the microfiber by high speed air jet attenuation. This kind of design has several notable advantages in fundamental process study compared with commercial multi-port extrusion die. Firstly, non uniform polymer distribution problems can be avoided and more uniform fibers can be produced in the single orifice design. Secondly, without the interference from other orifices, it is easier to control the operation conditions and to collect or take up the produced single continuous filaments. A high speed air jet nozzle was attached underneath the spinneret to generate a parallel high speed air jet to elongate the melt polymer once it was extruded out of the orifice. Since cold air was used, an insulation piece made from Teflon was inserted between the hot die and the cold air chamber to prevent the spinneret die from cooling. A winder was used to collect the produced fiber without applying any tension on the fiber threadline. The detail of this design is discussed in later part of this chapter.

### **3.1. Design of High Speed Air Jet Nozzle**

A convergent and divergent nozzle was designed and used to generate high speed air flow. When the stagnation pressure is close to atmospheric pressure, the air is considered incompressible and the air flow field is directly converted from flow rate measured by flow rate meter. When the air pressure is much higher than atmospheric pressure, the air

is then considered as compressible and a supersonic air flow may be generated under certain conditions based on the nozzle geometry.

### 3.1.1. Incompressible Air Flow

The velocity of the air jet at the exit plane of the nozzle can be calculated in terms of volume flow rate and nozzle cross-sectional area when the gas pressure is close to the atmospheric pressure. The air density is assumed to be constant in this case. The volume flow rate is the same anywhere in air flow line, which means the volume flow rate measured at the testing position is the same as that at the exit plane of nozzle. Hence, the air velocity can be calculated by the following equation:

$$V_a = Q_a / A \quad (4)$$

where A is the nozzle cross-sectional area,  $V_a$  is the air jet velocity, and  $Q_a$  is the volume flow rate of air jet.

To validate the calculated air velocity, a manometer was used to measure the air velocity at the nozzle exit plane. The calculated and measured air velocities obtained at different volume flow rates are listed and compared in Table 3-1.

Table 3-1 Air jet velocity comparisons.

<b>Air Volume Flow Rate (CFM)</b>	<b>1</b>	<b>2</b>	<b>3</b>	<b>4</b>	<b>5</b>
<b>Calculated Velocity (m/s)</b>	22	44	66	88	110
<b>Measured Velocity (m/s)</b>	24	56	80	100	130

The difference between the calculated and measured velocities might result from the assumption of a constant air density, since the air density will deviate from assumed constant value once the air pressure increases to a relative high value at high flow rate.

### 3.1.2. Compressible Air Flow

The convergent and divergent nozzle is also called Laval nozzle, named after Gustaf de Laval, a Swedish inventor. Laval nozzles were widely used in numerous industrial applications, e.g., steam turbines, rocket engines, mixing devices, thermal spraying facilities, etc [41, 45, 46, 89-91]. The gas flow through a Laval nozzle can be accelerated to a supersonic flow. The working mechanism can be explained from the basic continuity and momentum equations of compressible gas flow [92]:

$$0 = \frac{dV}{V} + \frac{d\rho}{\rho} + \frac{dA}{A} \quad (5)$$

$$0 = \frac{dp}{\rho} + d\left(\frac{V^2}{2}\right) \quad (6)$$

where  $A$  is the cross-sectional area,  $V$  is the gas velocity,  $\rho$  is the density, and  $p$  is pressure.

By introducing  $a^2 = dp/d\rho$  and  $M = V/a$  (Mach number), a relation between the infinitesimal area element,  $dA$ , and the infinitesimal velocity change,  $dV$ , can be obtained from Equations (5) and (6):

$$\frac{dA}{A} = -\frac{dV}{V}(1 - M^2) \quad (7)$$

Therefore, if a nozzle is composed of a converging nozzle first and then the diverging nozzle, the velocity of the gas flowing through it can be continuously increased in the direction of flow from subsonic to supersonic, as shown in Figure 3.1.

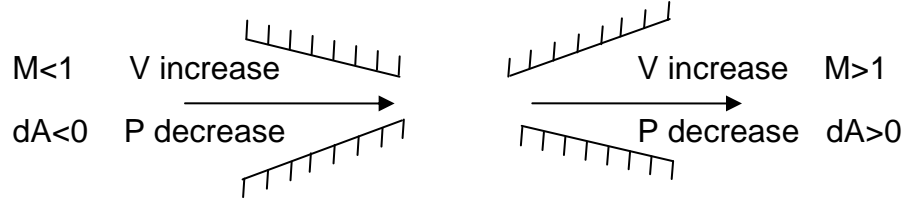


Figure 3.1 Mechanism of Laval Nozzle.

The following equations are the property ratios for the steady, isentropic and one-dimensional flow of a perfect gas, which are derived from the basic governing equations.

$$\frac{T_0}{T} = 1 + \frac{\gamma-1}{2} M^2 \quad (8)$$

$$\frac{p_0}{p} = \left( 1 + \frac{\gamma-1}{2} M^2 \right)^{\gamma/(\gamma-1)} \quad (9)$$

$$\frac{\rho_0}{\rho} = \left( 1 + \frac{\gamma-1}{2} M^2 \right)^{1/(\gamma-1)} \quad (10)$$

$$\frac{A}{A^*} = \frac{1}{M} \left[ \frac{2}{\gamma+1} \left( 1 + \frac{\gamma-1}{2} M^2 \right) \right]^{(\gamma+1)/[2(\gamma-1)]} \quad (11)$$

where  $A^*$  and  $A$  are the cross-sectional areas at the throat and the exit, respectively, and  $\gamma = C_p/C_v$  is the specific heat ratio.

To reach a supersonic speed, the nozzle needs to operate under an appropriate condition at which the above-defined ratios strictly obey Equations (8)-(11). The initial conditions were calculated by assuming that the air flow inside the nozzle is an isentropic flow of a perfect gas. With a cross-sectional area ratio of 1.08 between the outlet and the throat, the Mach number was calculated to be 1.33. The pressure and temperature ratios were then determined, using this Mach number, to be 0.35 and 0.74, respectively. With these nozzle design parameters, the outlet air pressure was expected to be identical to the back pressure, i.e., atmospheric pressure in our case. Thus the inlet pressure should be set

to 42 psi (289.6 KPa) with  $p/p_0=0.35$  and  $p=14.7$  psi (101.3 KPa). The air temperature at the exit was calculated to be 222 K with an initial temperature of  $T_0=300$  K at the inlet.

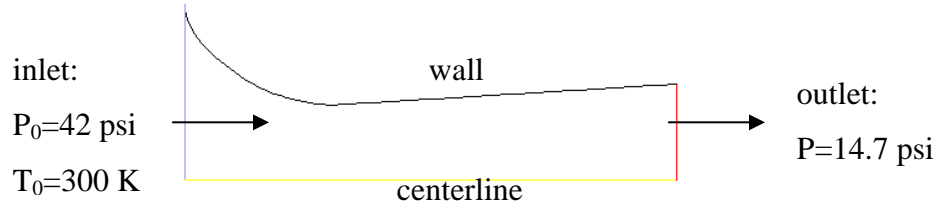
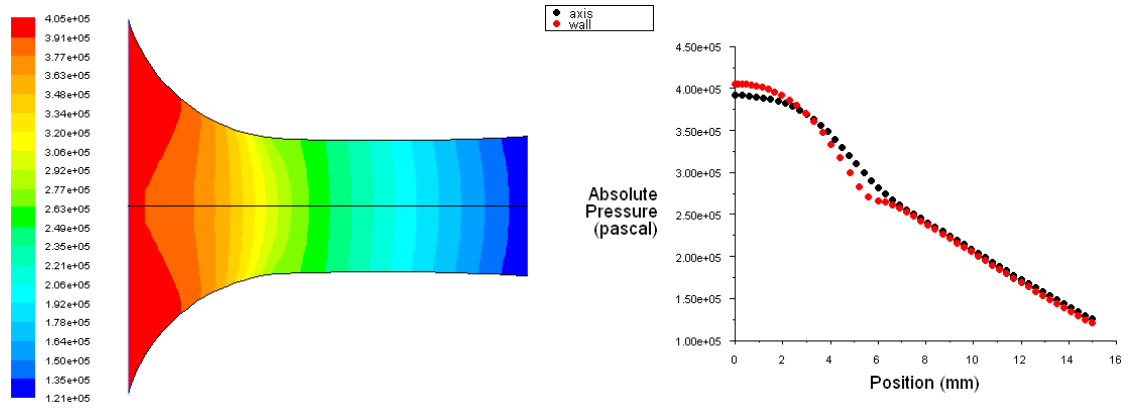
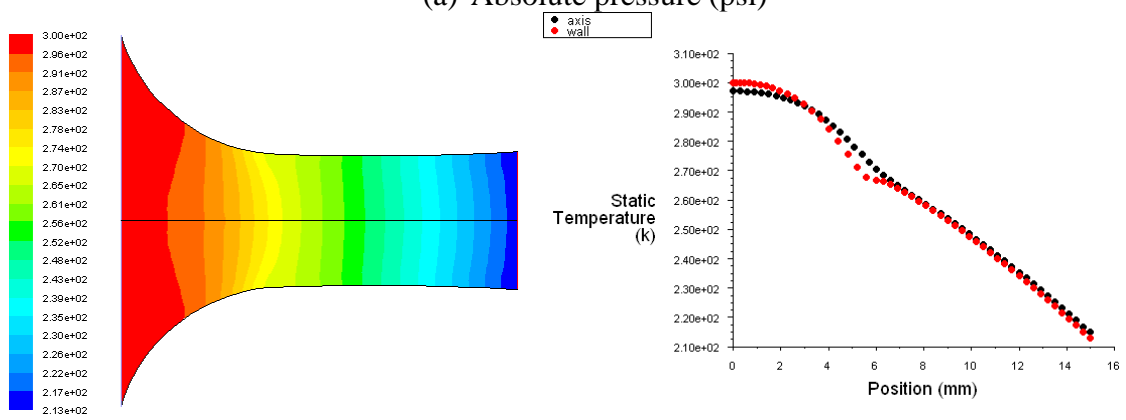


Figure 3.2 Boundary conditions for simulation.

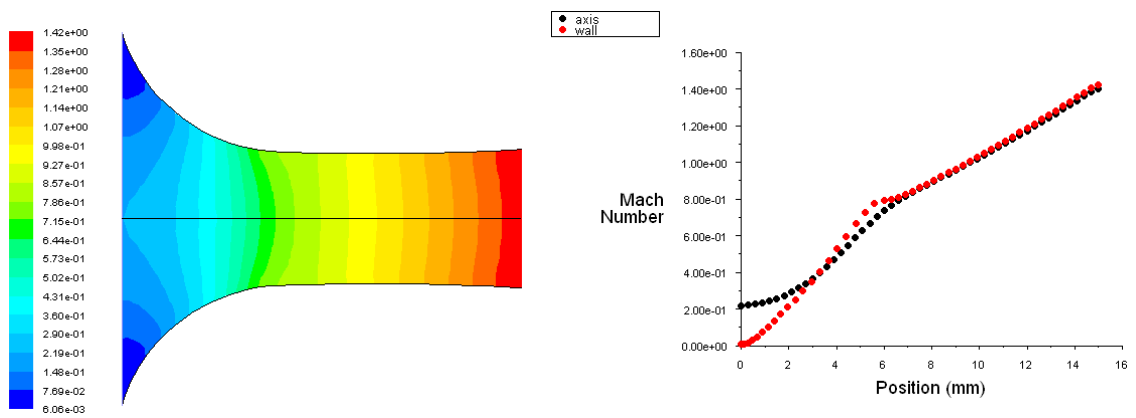
CFD simulations were conducted using Fluent® to analyze the air flow in the Laval nozzle and optimize our nozzle geometry. The axisymmetric nozzle geometry was imported to Fluent with the boundary conditions as shown in Figure 3.2. To reduce the difficulty and cost of making the nozzle, we modified the profile of the divergent part to a straight line. A testing case with the following setting of parameters was simulated to investigate the effect of the nozzle geometry on the air flow. An ideal gas and an inviscid flow model were used. The air pressure and temperature at the inlet were 42 psi and 300 K, respectively, and the exit air pressure was set to atmospheric pressure. Figure 3.3 shows the simulation results based on one geometrical design, including static pressure, static temperature and Mach number. Along the air flow direction, the air pressure kept decreasing to atmospheric pressure, the air temperature kept decreasing, and the air flow speed continuously increased to a Mach number of 1.33. These simulation results verified our calculation results from the equations, and a Laval nozzle made of metal was fabricated according to this geometry.



(a) Absolute pressure (psi)



(b) Static temperature (K)



(c) Mach number

Figure 3.3 Simulation results of static pressure, static temperature and Mach number.

### 3.2. Design of Spinneret Pack

Based on the simulation results, a cold air attenuation spinneret pack was designed which is consisted of an extrusion die, an insulation plate, an air chamber, and an air nozzle. In the first design, as shown in Figure 3.4, the compressed cold air went into the nozzle through multiple small holes on the wall of the air chamber. The polymer melt came down from the orifice and was then dragged by the high speed air through the nozzle. The extrusion die is single orifice with diameter of 0.5 mm. The insulation plate is made of Teflon and is used to isolate the hot die set from the air chamber, preventing the extrusion die from being cooled.

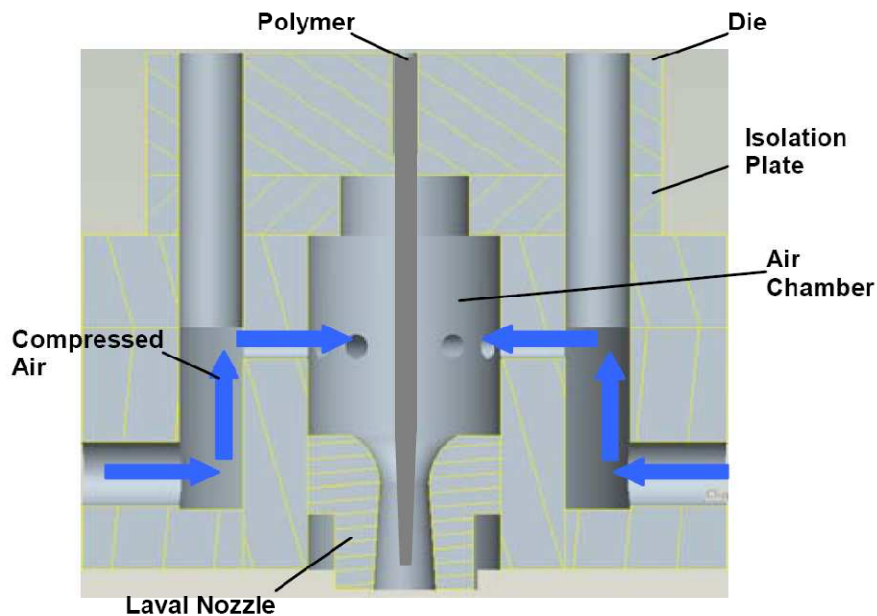


Figure 3.4 Detailed schematic of the first design of cold air attenuation setup.

However, after conducting a series of experiments on this spinneret pack design, it was found that the fibers tend to break before it can be attenuated to fine diameter. The fiber breakage may result from the instability caused by the high speed air flow. In this first spinneret pack design, the high speed air directly impacted with the fiber before it went through the high speed nozzle. Therefore, the high speed air flow acted like an

impinge flow to cut the fiber. Moreover, the melting fiber traveled a long distance from the extrusion orifice before it reached the high speed air nozzle. During this period, the fiber was cooled and thus ended up with large diameter since fiber attenuation only occurs in the melt stage. To overcome these drawbacks, a new spinneret pack was designed as shown in Figure 3.5, where a 60° cone shape extrusion die was introduced. With this modification, the gap between the extrusion die tip and air nozzle is reduced. Polymer melt is directly extruded into the high speed air nozzle for attenuation which reduces the cooling effect caused by cold air flow.

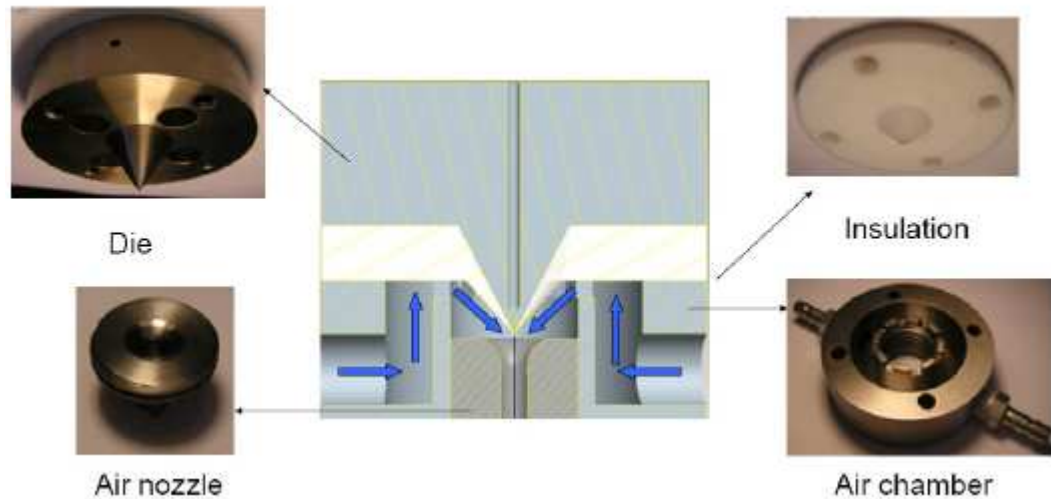


Figure 3.5 Detailed schematic of the second design of cold air attenuation setup.

In the spinneret pack, a heat insulation plate was also used to guide the air flow for reducing the impinge flow. Four insulation plates with different shape designs are shown in Figure 3.6. Design (a) and (b) are similar, and the only difference is in the tip shape; one is sharp and the other is blunt. The experimental results showed that the blunt tip actually reduces the fluctuation under the die tip, which makes the process more stable. Furthermore, the blunt tip design also provided a better insulation effect since the blunt tip has a thicker Teflon cover on the hot extrusion die tip. Insulation plates (c) and (d)



were designed to further prevent the fiber from being cooled and cut by high speed cold air flow. Based on design (b), the new designs included a small tube underneath the blunt tip. Since the air flow is blocked by the tube, the air inside the tube is actually in a stagnation state, which also prevents the melt from being cooled by the air. Compared with design (b), it is obvious that the Teflon plate is even thicker. Therefore, a better heat insulation can be expected with design (c). Insulation plate (d) was modified from design (c) to reduce the thermal conductivity between extrusion die and Teflon plate by creating a sealed air gap in which the heat conduction is negligible.

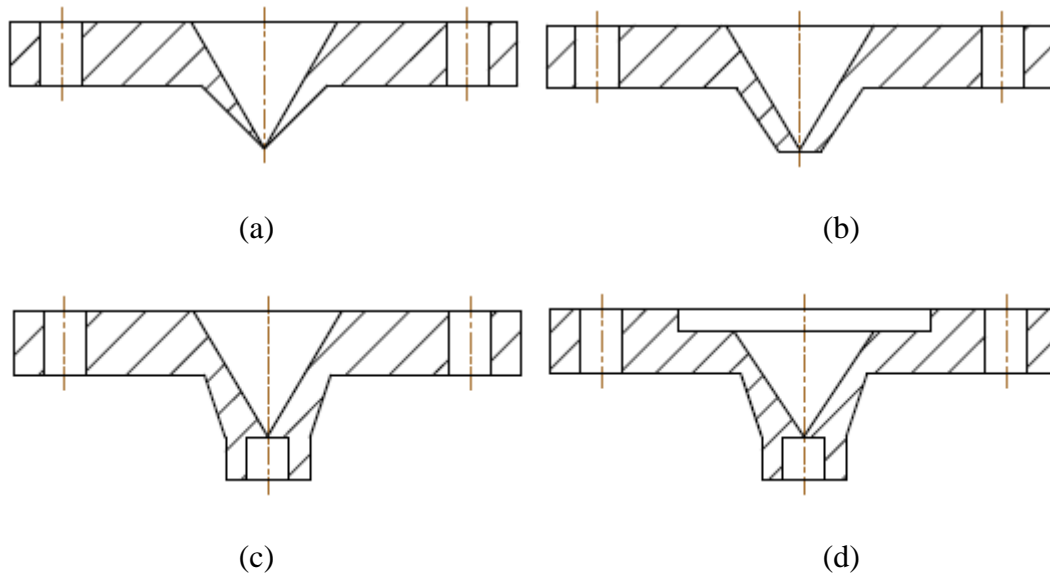
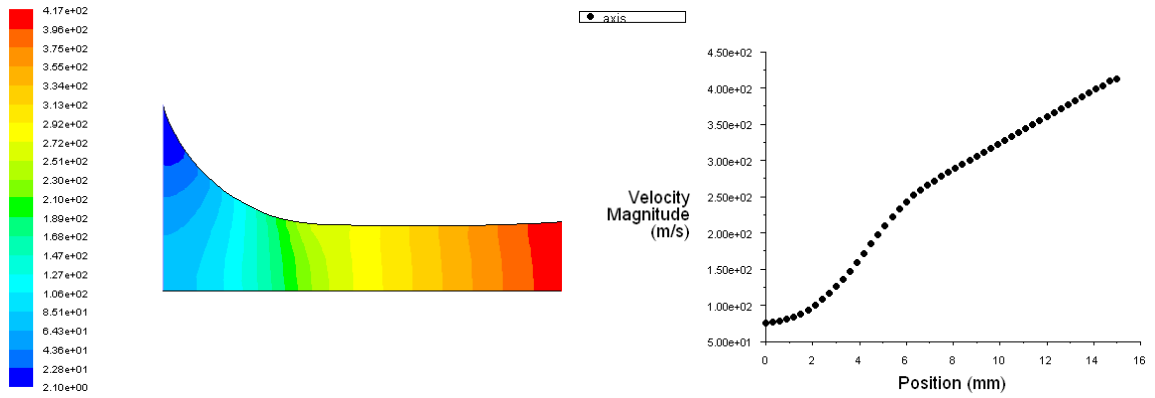


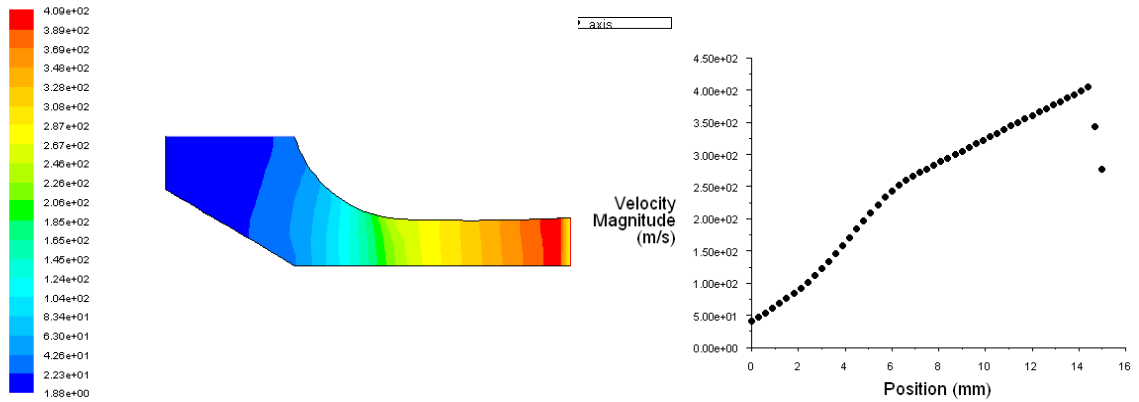
Figure 3.6 Four different insulation plate designs.

With the different shapes of insulation plates, the air flow was simulated using Fluent and results are showed in Figure 3.7. In these figures, position 0 represents the inlet of air nozzle. For all these four different insulation plates, the air flow showed the similar velocity at the inlet and reaches the same velocity at outlet, which is about 400 m/s for the compressible supersonic flow. Along the centerline of the air nozzle, the velocity profile is almost the same which means that the different shape of insulate plate does not

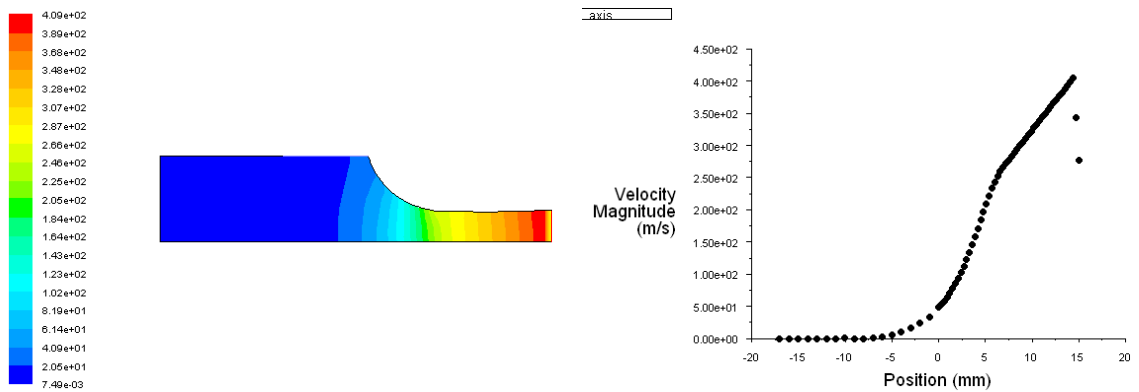
affect the air flow inside the nozzle. The simulation results of insulation design (c) also proved that there is a stagnation state inside the tube where air velocity is equal to zero.



Origin air nozzle



Air nozzle with insulation plate design (a)



Air nozzle with insulation plate design (c)

Figure 3.7 Air flow velocity profile of in the air nozzle and with two different insulation plates shape.

### **3.3. Experiment Setup**

A piston-driven melt extruder was built and mounted to a hydraulic press and retrofitted with cold air attenuation melt spinning spinneret pack. The fiber extruder consists of a cylinder with outside diameter of 2 inches (50.8 mm) and inside diameter of 0.5 inch (12.7 mm), a piston of 1 foot long and a specially designed melt spinning spinneret pack. The fiber extruder is held and fixed at the center beam of the frame of hydraulic press, as shown in Figure 3.8. The piston is driven by the hydraulic plunger at the top of press frame and its movement is controlled by the combination of valves and electronic unit. Sets of heat bands were used to heat the extruder bore and extrusion die with individual zone by zone temperature control unit. The spinneret pack was mounted to the bottom of extruder bore by 4 screws. Compressed air is generated by an air compressor. The compressed air was purified by sets of filters and then dried by refrigerated air dryer before supplied to the high speed air nozzle. The air temperature, flow rate and pressure were measured and monitored by the air flow rate meter and pressure regulator.

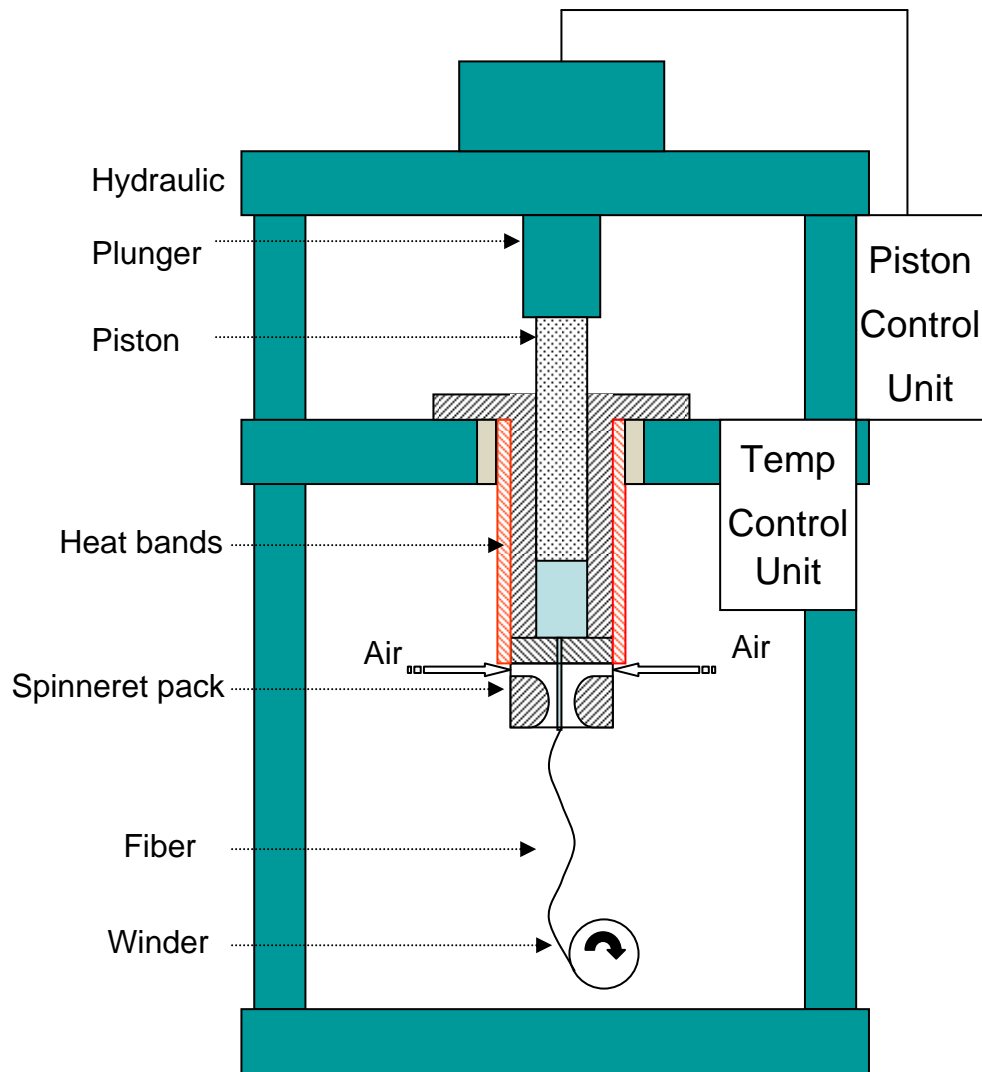


Figure 3.8 Schematic of customized hydraulic piston-driven fiber extruder.

## **CHAPTER 4**

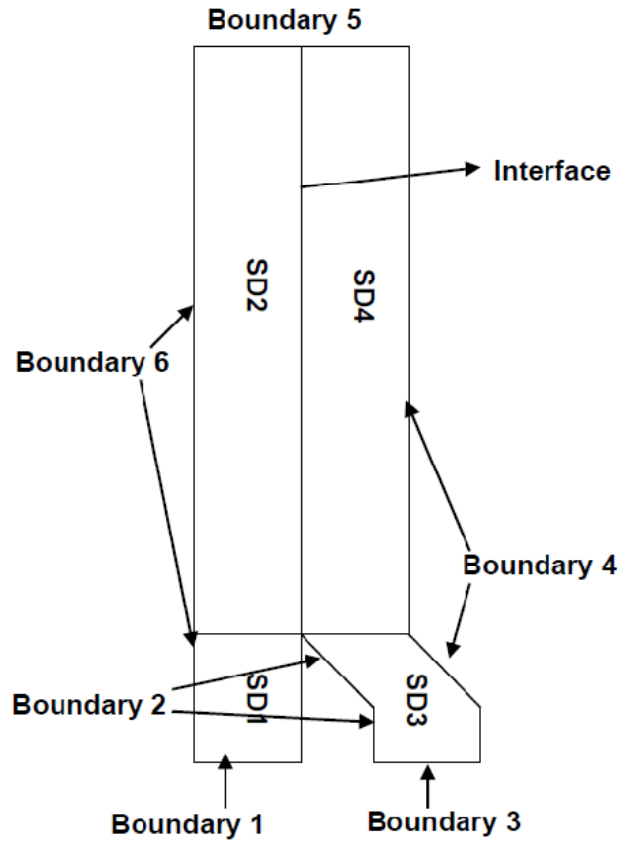
### **COMPUTATIONAL FLUID DYNAMICS SIMULATION OF THE FIBER ATTENUATION**

Before carrying out the experimental studies, a preliminary CFD simulation was conducted to provide basic guideline about what kind of processing conditions can lead to the production of continuous fine filaments. Then a parametric experimental study was designed based on the simulation results.

#### **4.1. Model Description**

The fiber attenuation process of polypropylene was simulated using a non-isothermal generalized Newtonian fluid model using the commercial software Polyflow®.

Figure 4.1 illustrates the geometry, sub-domains and boundary sets defined in the simulation. The geometry used in the model was from the real experimental setup, extrusion die with diameter of 500  $\mu\text{m}$  and air nozzle with diameter of 5 mm. The model consists of two co-flow fluids, one is the melt polymer and the other is the high speed cold air. The driving force for fiber attenuation was simulated by the friction force between air and polymer located on their intersection. Heat transfer was also considered on the intersection by applying a heat flux.



Boundary	Boundary Conditions	
	Flow	Thermal
1	Inflow	Temperature imposed-533 K
2	Wall	Insulated boundary
3	Inflow	Temperature imposed-300 K
4	Wall	Insulated boundary
5	Outflow	Outflow
6	Axis	Axis

Figure 4.1 Model descriptions of geometry, sub-domains and boundary sets, where the SD1 and SD2 present polymer, while SD3 and SD4 present air.

The intersection of polymer and air was set to interface condition, which is the standard boundary condition between two adjacent fluids. In Polyflow, this condition establishes the continuity of the velocity field and the contact forces in the momentum equation. During the simulation, the position of this intersection line was unknown at the beginning and was calculated as part of the solution. In other words, this interface boundary was considered as a moving boundary which requires re-meshing of geometry during calculation. In this steady flow of two immiscible fluids, the interface must be a streamline. An additional kinematic condition  $\mathbf{v} \cdot \mathbf{n} = 0$  was added to the system to satisfy this condition and thus ensured that the material points will not cross the interface.

#### 4.2. Material Properties and Viscosity Characterization

The material properties of polypropylene and air used in simulation are listed in Table 4-1:

Table 4-1 Materials properties of Polypropylene and air.

	$\rho$ (kg/m <sup>3</sup> )	$\eta$ (Pa·s)	$C_p$ (J/kg·K)	$\kappa$ (W/m·K)
<b>Air</b>	1.2	0.00002	1000	0.027
<b>Polypropylene</b>	900	*	2000	0.12

The viscosity of polypropylene is not listed in the table since the temperature and shear rate dependences of viscosity were considered in the simulation. The viscosity measurement was conducted by parallel plate rheometer. Frequency sweep test was carried out to measure the complex viscosity at a constant temperature with angular frequency ranging from 0.1 to 628.3 rad/s. Then the same tests were repeated for different temperature from 180 to 260°C. The complex viscosity  $\eta^*$  obtained from



parallel plate rheometer were directly mapped to shear rate dependent viscosity using the Cox-Merz rule.

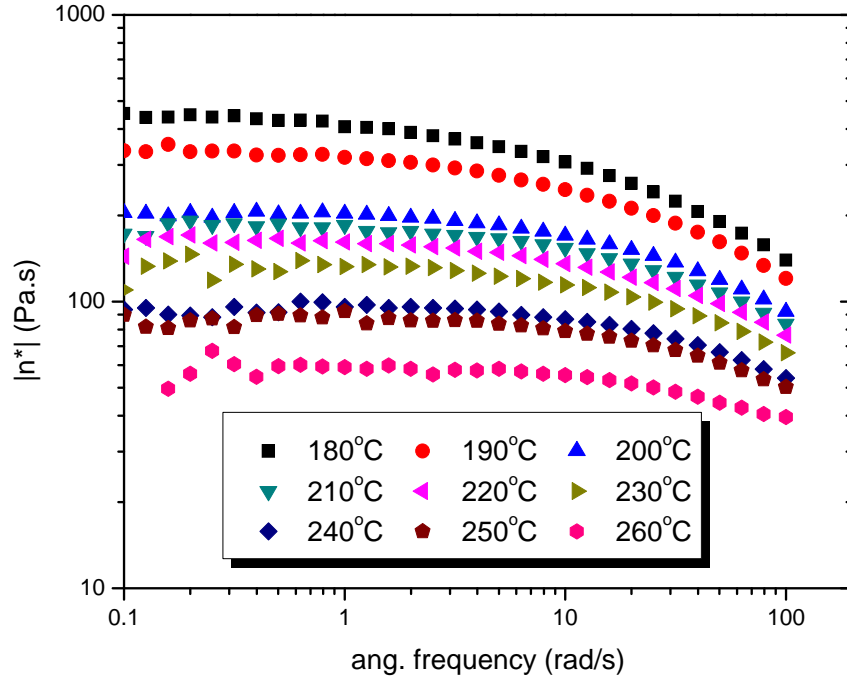


Figure 4.2 Polypropylene viscosity dependence of shear rate at different temperature.

The viscosity of polypropylene at temperature of 180°C was plotted against shear rate as shown in Figure 4.3. To describe the shear rate dependence of viscosity, several models were fitted to the measured data, such as power law, cross law and modified cross law model. After comparison, it was found that the cross law model provided the best fitting. The Cross law model used in Polyflow was defined as:

$$\eta = \frac{\eta_0}{1 + (\lambda \dot{\gamma})^m}, \quad (12)$$

where  $\eta_0$  = zero shear rate viscosity

$\lambda$  = nature time (i.e., inverse of the shear rate at which the fluid changes from Newtonian to power law behavior)

$m$  = Cross law index ( $=1-n$  for large shear rates)

$\dot{\gamma}$  = shear rate

In this fitted model, the parameters were determined as  $\eta_0=450$ ,  $\lambda=0.03$  and  $m=0.6$ .

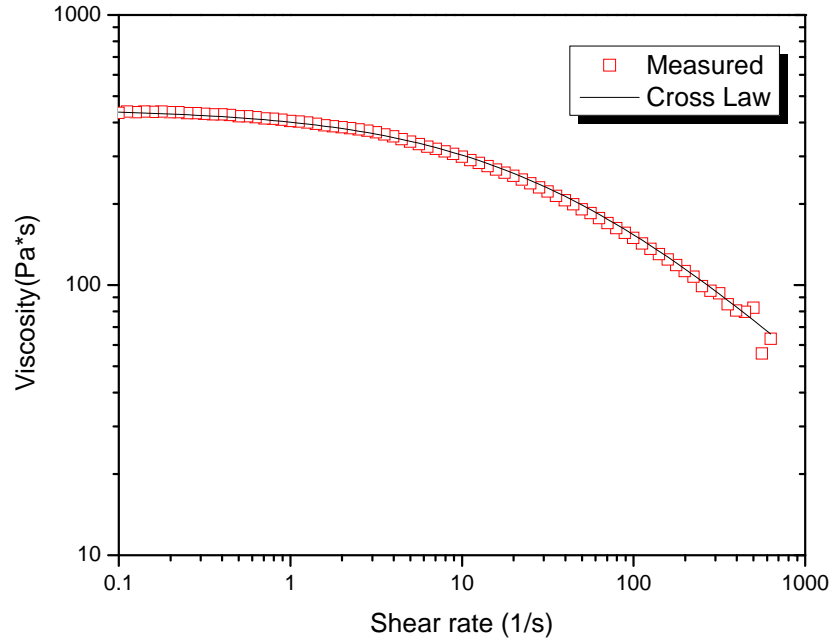


Figure 4.3 Polypropylene viscosity fitted by Cross law model at 180°C.

Arrhenius equation was used for different temperature shift and 180°C was chosen as the reference temperature. In Polyflow, the Arrhenius equation was given as:

$$H(T) = \exp\left[\alpha\left(\frac{1}{T-T_0} - \frac{1}{T_\alpha-T_0}\right)\right] \quad (13)$$

where  $\alpha$  is the energy of activation and  $T_\alpha$  is a reference temperature for which  $H(T) = 1$ . The reference temperature  $T_0$  is set to 0 by default, so  $T$  and  $T_\alpha$  are absolute temperatures.

The polypropylene viscosity in logarithmic scale was plotted against the reciprocal of temperature in Kelvin as shown in Figure 4.4. By fitting a linear model, the energy of activation  $\alpha$  was calculated and equal to 4.5976 KJ/mol.

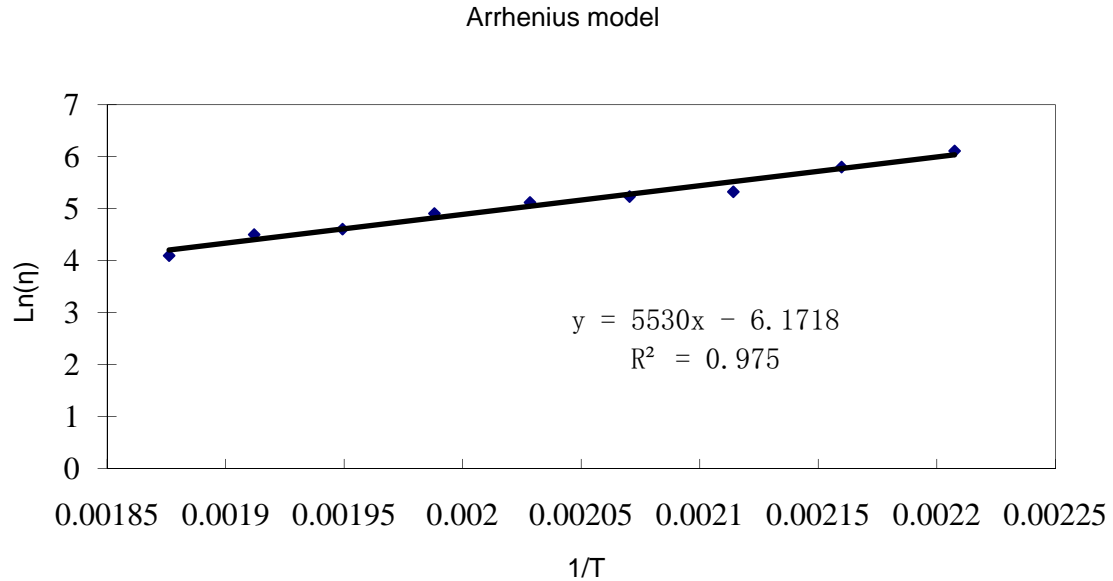


Figure 4.4 Polypropylene viscosity fitted by Arrhenius law model.

The fiber solidification transition was simulated by assuming the fiber viscosity increases to an extremely high value once the fiber temperature has been cooled below some specific temperature. Usually, the melting point was chosen as the temperature at which the polymer starts to solidify. As shown in Figure 4.5, the melting temperature of polypropylene is 165°C measured by DSC. However, it was observed in the rheological test that the polymer still behaved like a fluid even when the temperature was well below 165°C. Figure 4.6 shows the results of temperature ramp test by parallel plate rheometer. The test was conducted with angular frequency of 1 rad/s and temperatures decreasing from 180°C to 130°C. At temperature about 135°C, dramatic increases of storage and loss

modulus were observed which means that the polymer melt is becoming solid. Based on this observation, 135°C was chosen as the solidification temperature for the simulation.

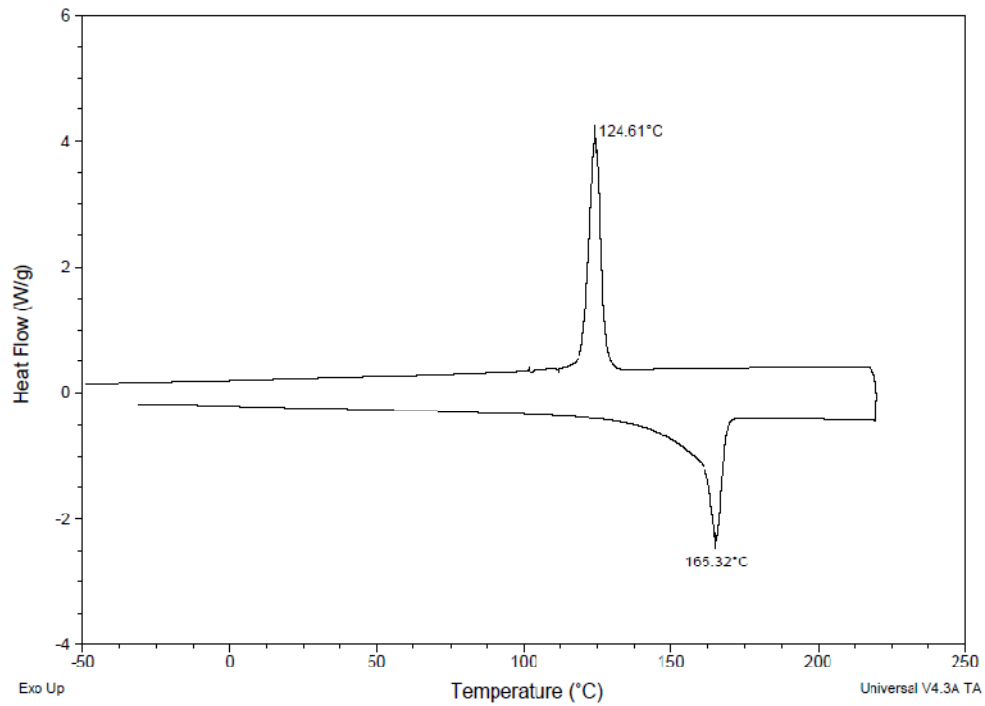


Figure 4.5 DSC test of virgin polypropylene.

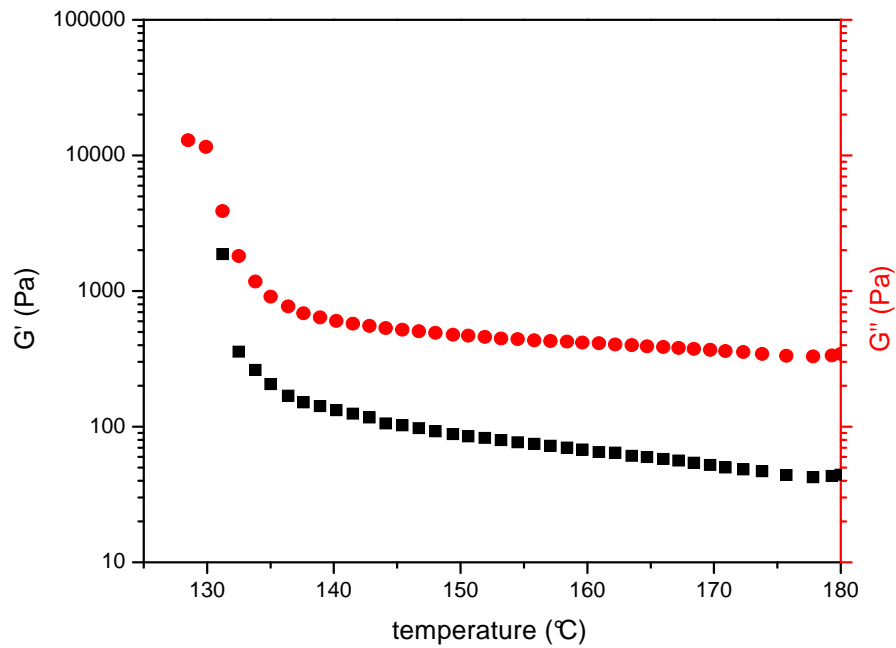


Figure 4.6 Temperature ramp with angular frequency at 1 rad/s for polypropylene.

### 4.3. Model Formulation

Polyflow uses a finite element method (FEM) to solve partial differential equations which are defined for the flow domains with boundary conditions. Since the problem involves an axisymmetric steel die and air jet nozzle, a 2-D cylindrical reference frame (r, z) with r=0 as the axis of symmetry was chosen which involves two velocity components (u,v). As a 2-D axisymmetric model, only half of the geometry was created and meshed in Gambit® and then imported to Polyflow.

In Polyflow, the following basic continuity equation, momentum equation and energy equations were used for calculation.

$$0 = \frac{\partial \rho}{\partial t} + \nabla \cdot (\rho \underline{v}) \quad (14)$$

$$\frac{\partial (\rho \underline{v})}{\partial t} + \nabla \cdot (\rho \underline{v} \underline{v}) = \nabla \cdot \underline{\underline{\sigma}} + \rho \underline{g} \quad (15)$$

$$\rho c_p \left( \frac{\partial T}{\partial t} + \underline{v} \cdot \nabla T \right) = \nabla \cdot (k \nabla T) + \dot{W} \quad (16)$$

The flow and thermal boundary conditions were described in previous parts. Cross law model and Arrhenius model were used to construct the constitutive equations. The intersection between polymer and air is a free surface interface, the shape of which is unknown. In order to maintain a proper shape for the meshed elements, the interface boundary deforms while the meshed elements deforms accordingly. As a typical re-meshing method for 2-D extrusion problem, the method of spines was chosen to re-mesh the geometry during the calculation.

The most difficult issue in this simulation was the convergence problem resulted from the nonlinearity and high gradient. The nonlinearity is caused by the shear rate

dependence of viscosity and heat convection. The high gradient exists on the interface between polymer and air because these two domains have huge difference in viscosity, density, temperature and flow velocity. Evolution method was then applied on these parameters and boundaries to ensure the convergence of the computation.

#### **4.4. Simulation Results and Discussion**

##### **4.4.1. Velocity Profile and Distribution of Filament**

In traditional melt spinning process, the velocity profile changes from a parabolic to a uniform profile under the tension force applied by the draw roller. However, in our new process, different velocity profiles were observed along the spinline. Near the spinneret orifice, the velocity profile is nearly parabolic, as expected. Downstream, the velocity starts to redistribute because of the high speed air drag on fiber surface, resulting in an inverse parabolic profile. But this inverse parabolic profile only stays for a short period since the filament is cooled down very fast by the high speed cold air. During the cooling process, the velocity starts to redistribute to a uniform profile and finally reaches a uniform velocity at the solidification point.

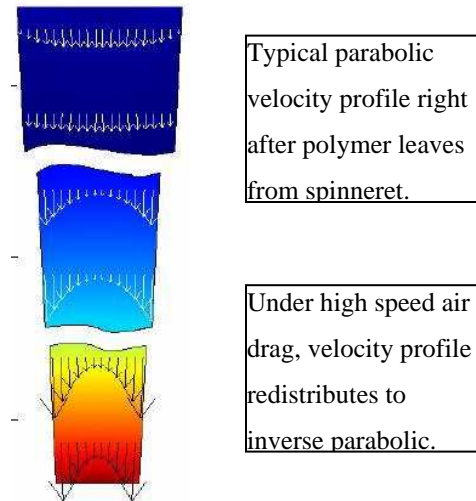


Figure 4.7 The velocity profiles and gradient in a spinline.

#### 4.4.2. Polymer Viscosity Effect

Viscosity is considered as the major factor in polymer processing because it indicates the polymer flow properties. In this study, three models with different zero shear rate polymer viscosities ( $\eta_0$ ,  $2\eta_0$  and  $4\eta_0$ ) were simulated by maintaining all the other conditions the same. The simulation results are shown in Figure 4.8. As expected, it showed that the final fiber diameter becomes bigger with the increase of polymer viscosity. It can also be observed that the viscosity significantly increases along the spinline. This is because the viscosity was intentionally set to a very high value once the fiber is cooled below the solidification temperature. This transition can ensure that the fiber will not be attenuated after the solidification.

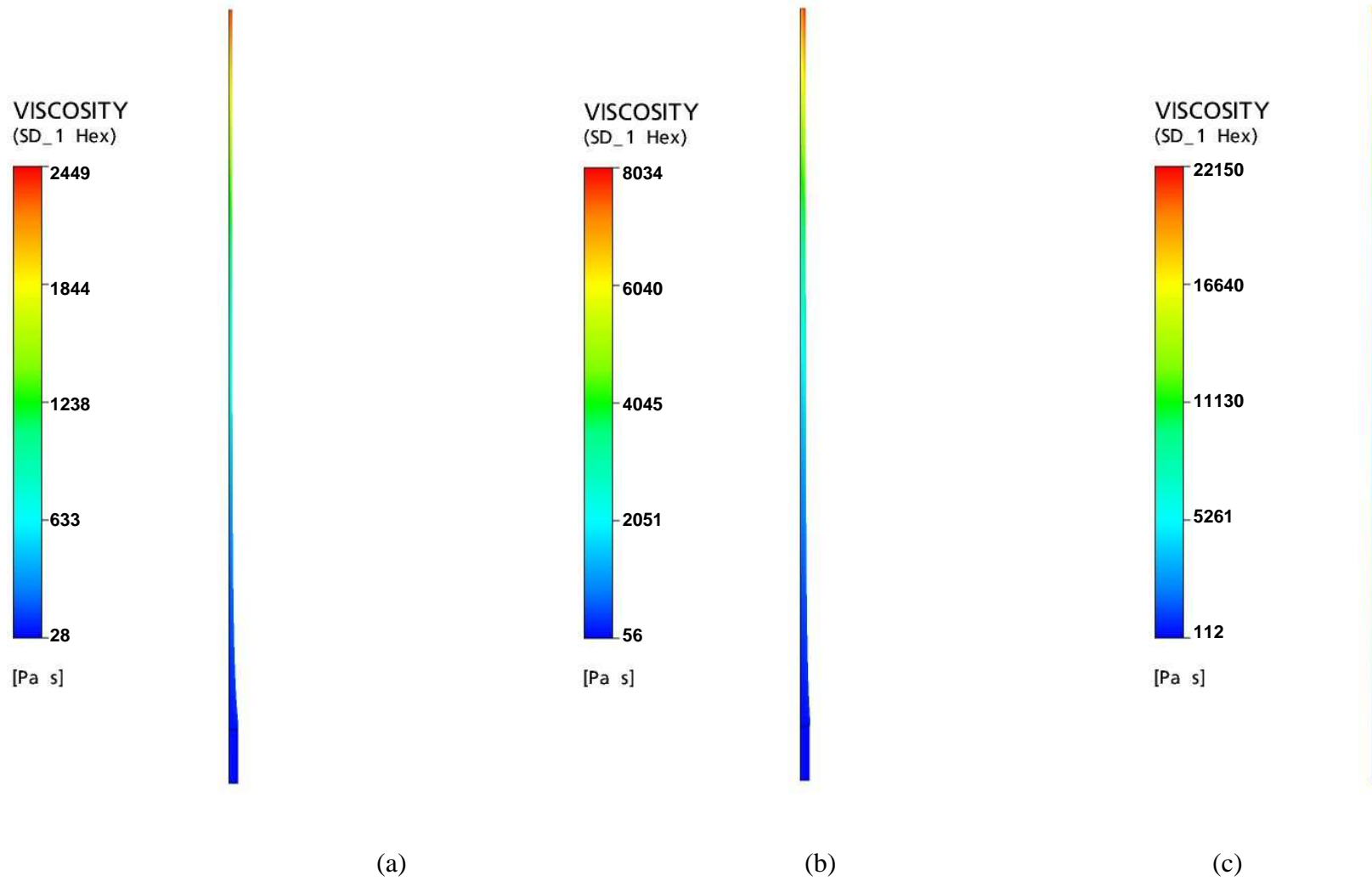


Figure 4.8 Effect of polypropylene viscosity on fiber geometries, (a) low viscosity; (b) medium viscosity and (c) high viscosity.



#### **4.4.3. Processing Temperature Effect**

Processing temperature plays an important role in this fiber spinning process since it affects not only the polymer viscosity but also the heat transfer between the polymer and air. For comparison, the simulations were conducted with three different processing temperatures, 200°C, 230°C and 260°C. The resulting fiber geometries with temperature profile are shown in Figure 4.9. With the increase of processing temperature, the final fiber diameter becomes smaller. This is because the higher temperature results in a lower melt viscosity which makes polymer melt more easily to be attenuated under the air drag force. Meanwhile, the higher processing temperature also provides longer time for attenuation before the polymer melt is solidified.

It is interesting to point out that the fiber attenuation mechanism in this process is totally different from that in conventional melt spinning, in which the fiber diameter either gradually decreases along the spinline or a neck is formed somewhere along the spinline. However, in our process, the attenuation took place within a very short distance underneath the spinneret. Beyond that distance, the polymer melt is already cooled down and becomes solid.

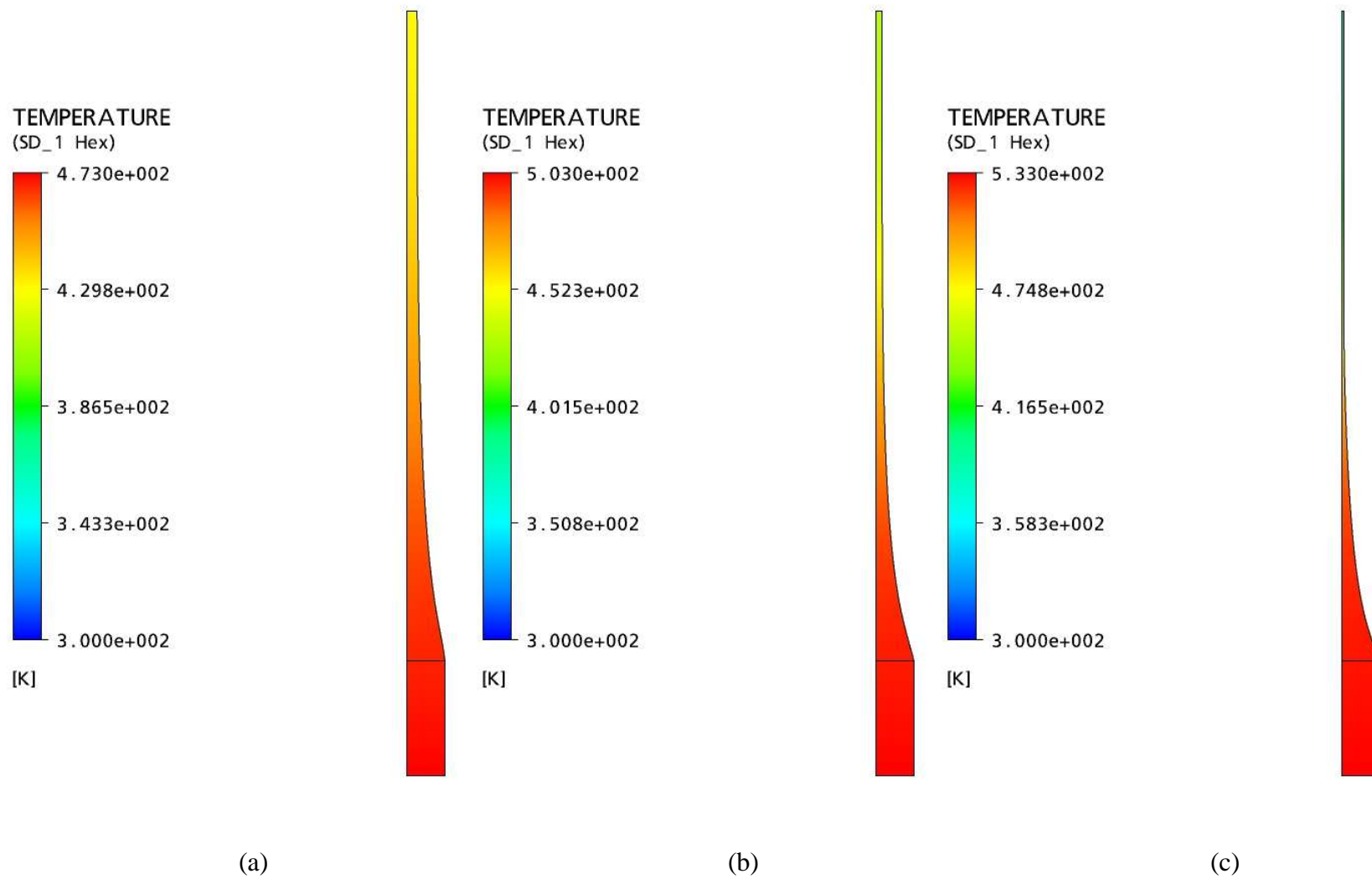


Figure 4.9 Fiber geometries and temperature profiles at different processing temperature: (a) 200°C; (b) 230°C and (c) 260°C.

#### **4.4.4. Air/Polymer Flow Ratio Effect**

In this section, the simulations were conducted under three different levels of air to polymer flow ratios, 4000, 8000 and 16000 respectively. As expected, the higher ratios produced finer fibers because the higher air flow rate provides more drag force on the fiber surface. However, in experiments the air flow rate cannot go too high. When it reached some critical point, the polymer melt began to break and ended up with staple fibers. As the air flow speed continuously increases to supersonic, a nonwoven type of web can be produced even with cold air of at room temperature. Under the supersonic air flow, the polymer melt was attenuated and shot out of the air nozzle extremely fast. Within such a short time, the polymer still remained at melt stage after it left from the air nozzle. Therefore, the melt fibers adhered to each other and formed a nonwoven web.

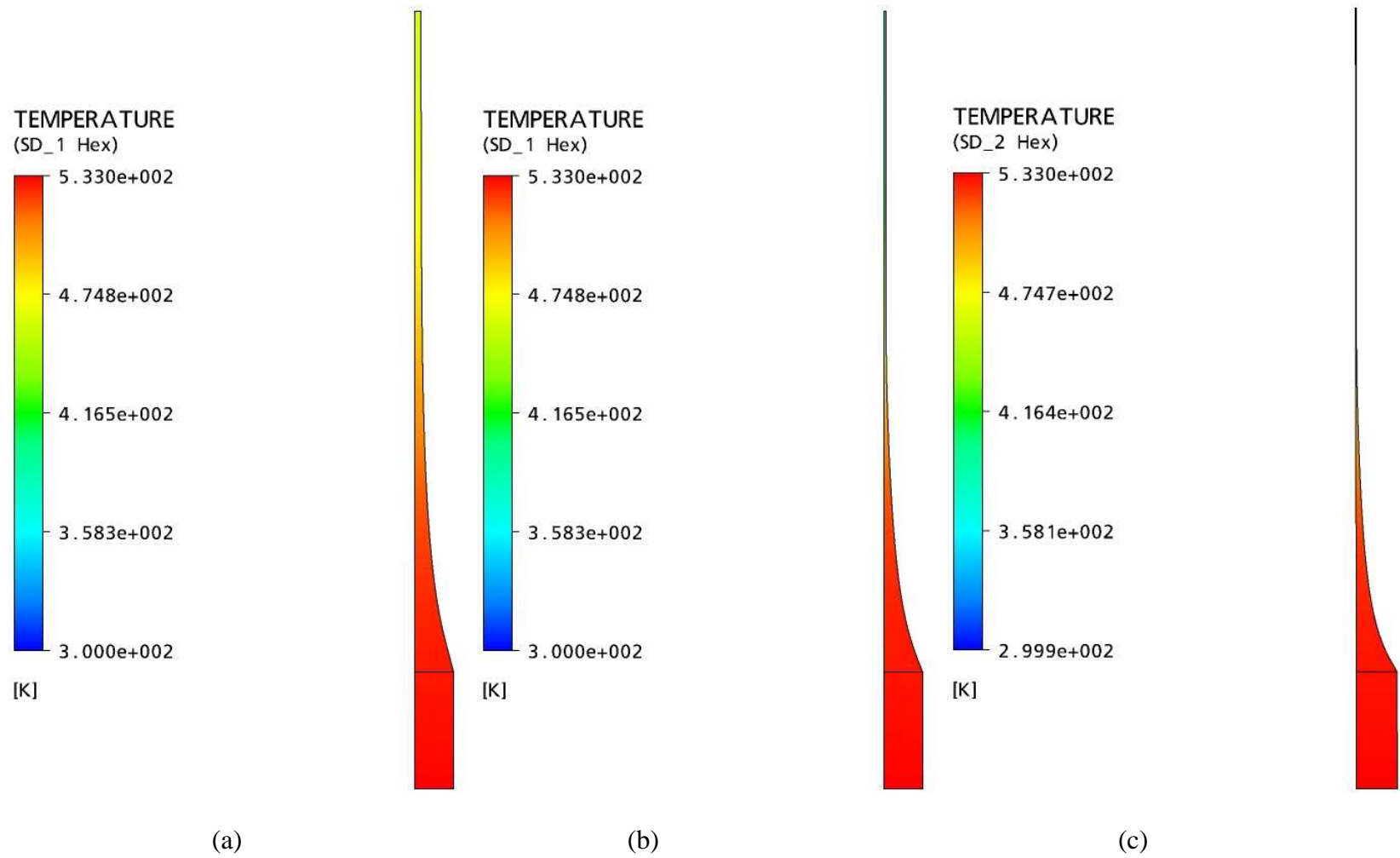


Figure 4.10 Fiber geometries and temperature profiles at different air/polymer flow ratio: (a) low; (b) medium and (c) high.

#### **4.4.5. Limitations**

The above CFD simulation provided a comprehensive understanding of the attenuation mechanism for this modified fiber spinning process. Nevertheless, the gap between simulation and experiments still exists in this specific case for two reasons. Firstly, the above simulation can not exactly model the air drag force applied by high speed air flow. Secondly, a fixed geometry is required for each simulation model, but the simulation results are also dependent on the origin geometry. It is difficult to run the iteration on the geometry to find out when and where exactly the fiber is solidified. Therefore, an improved model is desired for a more focused theoretical study on the fiber attenuation mechanism.

## **CHAPTER 5**

### **EXPERIMENTAL STUDIES**

#### **5.1. Materials**

Polypropylene and Nylon-6 were selected to produce continuous fine filaments.

Polypropylene was chosen as raw material because of its wide variety of applications and relative ease to process from the melt. Its large range of available molecular weights and tacticities can offer the opportunity for the study of the effect of material properties on the resulting fiber diameter and other properties. The insulation plate in the spinneret pack was made of Teflon, and its highest operating temperature is 260°C. The relative low melting temperature of PP (165°C) has a great advantage for parametric studies because it gives about 100°C temperature window to conduct the parametric study on processing temperature. In this study, three different grades of PP were used to produce fibers. PP115 was obtained from Phillips Sumika Polypropylene Company with an MFI (melt flow index) of 115 (grams per 10 minutes). PP35 was obtained from Sigma Aldrich with MFI 35 and average molecular weight  $M_n=50000$ . PP12 was also obtained from Sigma Aldrich with an average molecular weight  $M_n=67000$ .

As a widely used material in the textile industry, Nylon 6 was also chosen in this study to demonstrate the applicability of this new process to other types of polymer. Nylon 6 was obtained from BASF with MFI 130 and melting point about 235°C. The Nylon 6 was dried in a vacuum oven at temperature about 90°C for 48 hours before being used in the melt spinning experiments.

## 5.2. Design of Parametric Studies

Firstly, a series of experiments were conducted to determine the proper process conditions which can lead to the production of continuous fibers finer than 1 denier. Then a full parametric study was carried out to further investigate the relationships between the resulting fiber properties and processing conditions. In this study, the processing conditions include the air flow rate, the polymer mass flow rate and the processing temperature. The fiber properties include the fiber diameter, tensile strength, tensile modulus, molecular orientation and crystallinity.

The parametric study was designed based on the previous simulation results. It was indicated by the simulation that the final fiber diameter depends on the polymer viscosity, the processing temperature and the air flow rate. Therefore, three polypropylenes with different viscosity values were chosen in the experimental studies. For each polypropylene, four different temperatures were chosen as processing temperatures: 180°C, 200°C, 220°C and 240°C respectively. Under each processing temperature, the air flow rate was adjusted from 1 to 5 cfm (cubic feet per minute, 1 cfm=0.0283 m<sup>3</sup>/min) or even higher with 1 cfm increment. The full parametric design is given in Table 5-1.

Table 5-1 First design of parametric studies on processing conditions.

Air flow ratio	1 CFM	2 CFM	3 CFM	4 CFM	5 CFM
180°C	√	√	√	√	√
200°C	√	√	√	√	√
220°C	√	√	√	√	√
240°C	√	√	√	√	√

\* 3 different polypropylenes are used to repeat this parametric study.

### 5.3. Fiber Production

In every experiment, polypropylene pellets were fed into the extruder and pre-heated to desired temperature for about 10 minutes before extrusion. Low-velocity air flow was conducted at the startup to cool down the cold air attenuation setup, which was conductively heated by the die. When all temperatures stabilized, the hydraulic press was turned on and began to extrude the polypropylene under a slight air drag. Then the air flow rate was slowly and continuously raised to increase the air flow velocity. As indicated in the literature on melt blowing, the higher the ratio of air flow rate to polymer mass flow rate, the finer the fibers can be produced. Therefore, in our experiments, the polymer mass flow rate was fixed at a relative small value. The air volume flow rate was purposely changed from low to high at different levels as designed in the parametric study. The same sets of experiments were then repeated with different processing temperatures. With this design, a large number of fibers were produced at different processing conditions for further study on the relationships between fiber properties and processing conditions.

Firstly, a small number of experiments were conducted (for sensitivity study purposes) to gain some guidelines for producing continuous filaments. It was observed that the previously designed parametric studies cannot be fully applied to some experiments. Specifically, the melt filaments tended to break at high air flow rate when the melt viscosity was relatively low. The low melt viscosity can be caused either by the polymer properties itself or by high processing temperature. Therefore, only low air flow rate can be applied for low viscosity polypropylene and high processing temperature. For example, at 220°C and 240°C, the maximum air flow rate for low viscosity PP115 is



about 1-2 cfm. In this case, the air flow rate was fixed at 1 cfm and the polymer flow rate was adjusted to several different levels to fulfill the parametric studies. Consequently, instead of the air volume flow rate, the air/polymer volume flow ratio was used as a variable of processing condition to conduct the parametric studies. The new parametric studies were designed based on this modification as shown in Table 5-2.

Table 5-2 Second design of parametric studies on processing conditions.

<b>Air/polymer volume flow ratio</b>	<b>50000</b>	<b>100000</b>	<b>200000</b>	<b>300000</b>	<b>400000</b>	<b>500000</b>	<b>600000</b>
<b>180°C</b>	√	√	√	√	√	√	√
<b>200°C</b>	√	√	√	√	√	√	√
<b>220°C</b>	√	√	√	√	√	√	√
<b>240°C</b>	√	√	√	√	√	√	√

\* 3 different polypropylenes are used to repeat this parametric study.

In conventional melt spinning, a roll winder is used to collect the fibers and at the same time provides a tension force to attenuate the melt filament. In our study, the major objective was to investigate the effects of cold air attenuation on resulting fiber properties. The tension force generated by the roll winder can cause interference on the study of the air drag force effect. Therefore, in our experiments, the produced fibers freely fell down into a box collector as a coil or were collected simultaneously by a roll winder with a speed that was much lower than the fiber speed to avoid the tension force.

#### **5.4. Fiber Characterizations**

Different characterization methods were performed to study the resulting fiber properties, including microstructures, thermal properties, mechanical properties, rheological properties, molecular orientation and crystallization behavior.

#### 5.4.1. Fiber Microstructures

Fiber linear mass density was measured by a vibroscope (Lenzing Instrument) according to ASTM D1577. Fiber diameter was then converted based on the relationship: 1 denier = 1 gram per 9000 meters. Assuming the fiber is a cylinder with uniform diameter, the fiber diameter can be derived by the equation:

$$d_f = \sqrt{\frac{4 \times \text{denier}}{9000 \times \rho_f \times \pi \times 1000}} \quad (17)$$

Scanning electron microscopy (SEM) was employed to examine fiber geometry. Two different SEM setups were used in this study: Hitachi S800 field emission gun and Hitachi-3400SN respectively.

#### 5.4.2. Thermal Analysis

Polymer melting, glass transition and crystallization behavior were studied by differential scanning calorimetry (DSC) (TA Instrument Q2000 model). The fibers were cut and wound to fit into the DSC aluminum pan. The sample was heated from -60°C to 220°C under different heating rate, 5°C/min, 10°C/min, 20°C/min and 40°C/min. Then the sample was cooled down at the same cooling rate. A second cycle was repeated with the same heating and cooling rate.

Polymer crystallinity can be determined with DSC by quantifying the heat associated with melting (fusion) of the polymer. This heat was reported as percent crystallinity by normalizing the observed heat of fusion to that of a 100% crystalline sample of the same polymer. As authentic samples of 100% crystalline polymer are rare, literature values are often used for this value.

$$a_c = \Delta H_m / \Delta H_m^0 \times 100\% \quad (18)$$

where the melting enthalpy of the ideal perfect crystalline polypropylene per gram  $\Delta H_m^0$  is 207 J/g. It is believed that the first heating cycle would include information of previous thermal and mechanical history formed in the polypropylene fiber. Therefore, the melting enthalpy of this cycle was used to evaluate the fiber crystallinity.

The polymer viscoelastic nature and glass transition temperature are analyzed by dynamic mechanical analysis (DMA) (TA Instrument Q800 model). Since there is no fiber clamp available with the machine, fibers were first fixed on a paper tab and then were fastened by clamps used for film testing. When the fiber diameter is smaller than 50 microns, a single fiber is too weak to meet the requirement of DMA test. In this case, a bundle of fibers was prepared in which all the fibers were aligned parallel. The sample was heated from -40°C to 60°C in a nitrogen environment with heating rate 1 °C/min. The test was performed under tension mode. The oscillation frequency was fixed at 5 Hz and the strain amplitude was 0.1%, which was well within the linear viscoelastic region. The storage modulus, loss modulus and loss tangent were recorded and plotted against temperature.

#### **5.4.3. Mechanical Properties**

The tensile properties of monofilament were measured using an Instron tensile test machine with a 2.5 Newton load cell. The single fiber was cut to a proper length and fixed on the specific fiber test tab with test length of one inch. The crosshead speed was set to 2.0 cm/min for all tests. Three samples were tested at one time to obtain the average results of tensile strengths, elongation ratios and tensile modulus. The stress-strain curve was recorded and used to calculate the tensile modulus.

#### **5.4.4. Rheology**

Rheology tests were performed on a parallel plate rheometer (TA Instrument AR2000ex) to study the polymer viscosity dependence of temperature and shear rate. The test results were also used as the material data in simulation. The test sample sheet was molded by a hot press at 200°C. Then the sheet was cut into a plate with diameter of 25 mm and thickness about 2-3 mm. Oscillation model with frequency sweep was used for all the tests. During the test, the angular frequency swept from 628.3 rad/s to 0.001 rad/s with gap distance 1000  $\mu\text{m}$ . The storage modulus  $G'$ , loss modulus  $G''$  and complex viscosity  $|\eta^*|$  were collected and plot against angular frequency.

#### **5.4.5. Fiber Molecular Orientation**

In this study, two different methods were used to determine the fiber molecular orientation.

The X-ray diffraction study was conducted on a Rigaku Micromax-002 WAXS/SAXS system operated at 45 kV and 0.66 mA and equipped with a Rigaku R-axis IVtt 2-D detection system. The diffraction patterns were analyzed using Area Max V. 1.00 and MDI Jade 6.1 software. A bundle of sample fibers were aligned and fixed on a paper tab which was then placed on the sample holder with fiber oriented vertically. The plane of the fibers was then adjusted perpendicular to the incident beam. The intensity was collected with  $2\theta$  from 8 to 35 degrees. The background was subtracted by scanning the air under the same condition. Most efficiently, the fiber molecular orientation can be qualitatively determined by the 2-D pole figures. Quantitatively, the orientation can be determined by the Wilchinsky equation [93] and the Herman orientation function if a symmetry plane perpendicular to c axes (fiber axes) exists.

$$\langle \cos^2 \phi_{j,z} \rangle = \frac{\int_0^{\pi/2} I_{hkl}(\phi_{j,z}) \cos^2 \phi_{j,z} \sin \phi_{j,z} d\phi_{j,z}}{\int_0^{\pi/2} I_{hkl}(\phi_{j,z}) \sin \phi_{j,z} d\phi_{j,z}} \quad (19)$$

$$f_j = \frac{3 \langle \cos^2(\phi_{j,z}) \rangle - 1}{2} \quad (20)$$

Here,  $\phi$  is the azimuthal angle and  $I(\phi)$  is the scattered intensity at  $\phi$ ,  $f$  is the orientation factor.  $\langle \cos^2 \phi \rangle$  is equal to 1 when all the crystals are oriented with  $c$  axes parallel to the reference direction, and equal to 0 when perpendicular to reference direction.

However, there is no such a plane in  $\alpha$  monoclinic isotactic polypropylene. Therefore, the intensity of 110 and 040 crystal planes was used to calculate the orientation based on the following equations:

$$\langle \cos^2 \phi_{c,z} \rangle = 1 - 1.1099 \langle \cos^2 \phi_{110,z} \rangle - 0.901 \langle \cos^2 \phi_{040,z} \rangle \quad (21)$$

$$f_c = \frac{3 \langle \cos^2 \phi_{c,z} \rangle - 1}{2} \quad (22)$$

In addition to X-ray diffraction, polypropylene fiber molecular orientation can also be qualitatively determined by polarized Raman spectroscopy [94, 95] as reported recently. As shown in Figure 5.1, it was confirmed that the ratio of the 841 to 809  $\text{cm}^{-1}$  band intensity has an approximately linear relation with birefringence and can be used to qualitatively estimate the molecular orientation in polypropylene fiber.

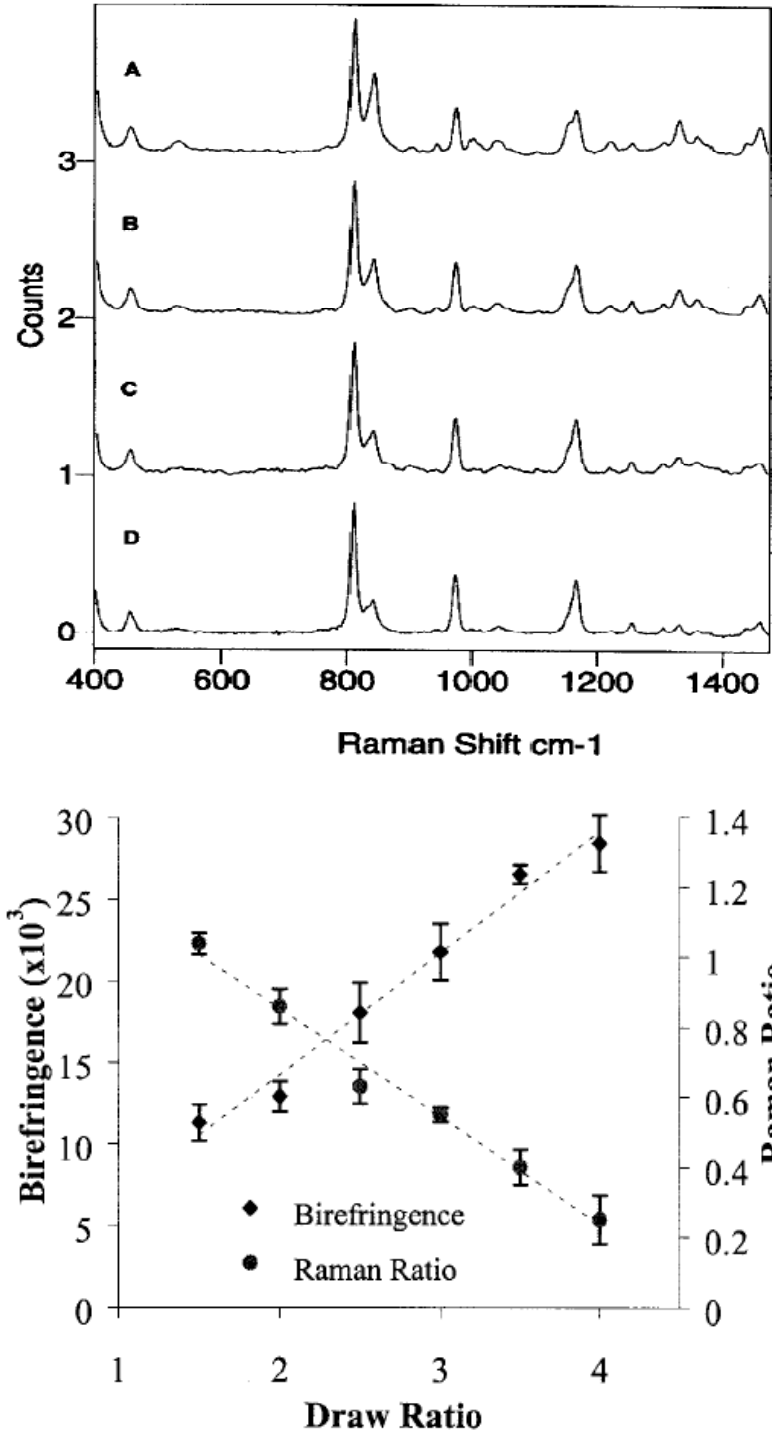


Figure 5.1 Up: typical on-line ZZ polarized Raman spectra for polypropylene fibers with different draw ratios (A 1.5, B 2.5, C 3.0 and D 3.5); Bottom: Plot of draw ratio vs. the Raman intensity ratio and birefringence for the polypropylene fibers [94].

The Raman spectra were collected on Holoprobe Research 785 Raman Microscope using 785 nm incident laser wavelength with polarizer and analyzer parallel to each other. The test sample was prepared in the same way as that for X-ray diffraction test. The plane of the fibers was perpendicular to the incident laser. The test results were plotted as the intensity against Raman shift. The curve was then smoothed and subtracted a linear base line for further peak fitting to determine the actual peak area of peak 809 and 841  $\text{cm}^{-1}$ . Compared with X-ray diffraction, this method requires significantly shorter time on test scanning and data analysis. Therefore, Raman spectra were mainly used in this study to determine the fiber molecular orientation. The result measured by Raman spectra was also compared with wide angle X-ray diffraction data.

#### **5.4.6. Fiber Crystallization Behavior**

In addition to DSC, Wide angle X-ray diffraction was also used to determine the resulting fiber's crystal form, crystallinity and crystal size based on integrated X-ray diffraction spectra. The data can be collected during the orientation test or by performing the same test procedure. The crystal size was calculated using the Scherrer equation:

$$\tau = \frac{K \lambda}{\beta \cos \theta} \quad (23)$$

Here, K is the shape factor and equal to 0.9 for polypropylene,  $\lambda$  is the wavelength of CuKa which is equal to 1.54 Å,  $\theta$  is the Bragg angle,  $\beta$  is the peak breadth at half-maximum intensity.

## CHAPTER 6

### EXPERIMENTAL RESULTS AND DISCUSSIONS

Continuous fibers were produced from three polypropylenes with different viscosity value according to the design of the parametric studies. The resulting fibers were collected and characterized to determine their geometry, molecular orientation, crystallization behavior and mechanical property. In this chapter, these characterization results will be presented. The relationship between processing conditions and fiber properties will also be discussed.

#### 6.1. Fiber Geometry

##### 6.1.1. Effect of Polypropylene Viscosity and Processing Temperature

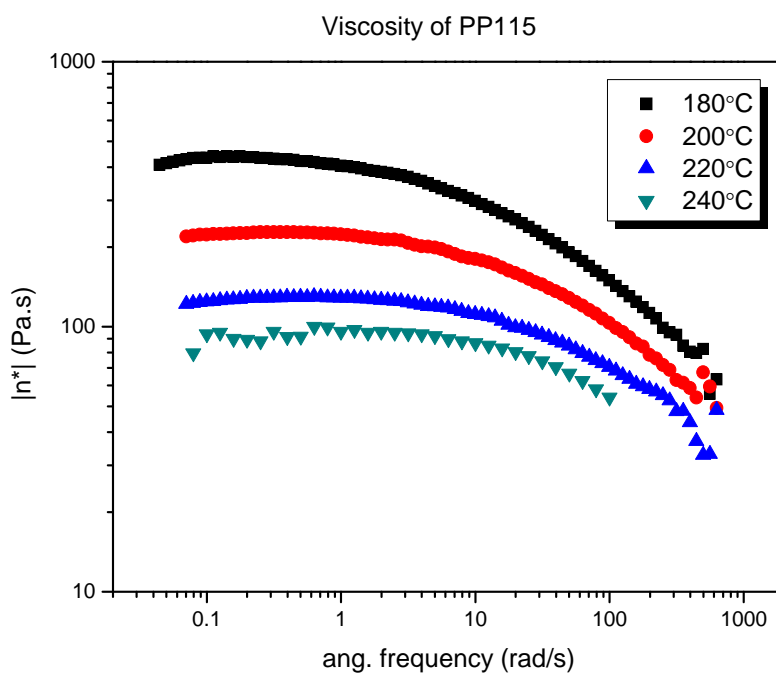


Figure 6.1 Viscosity of PP115 at different temperatures and angular frequencies.



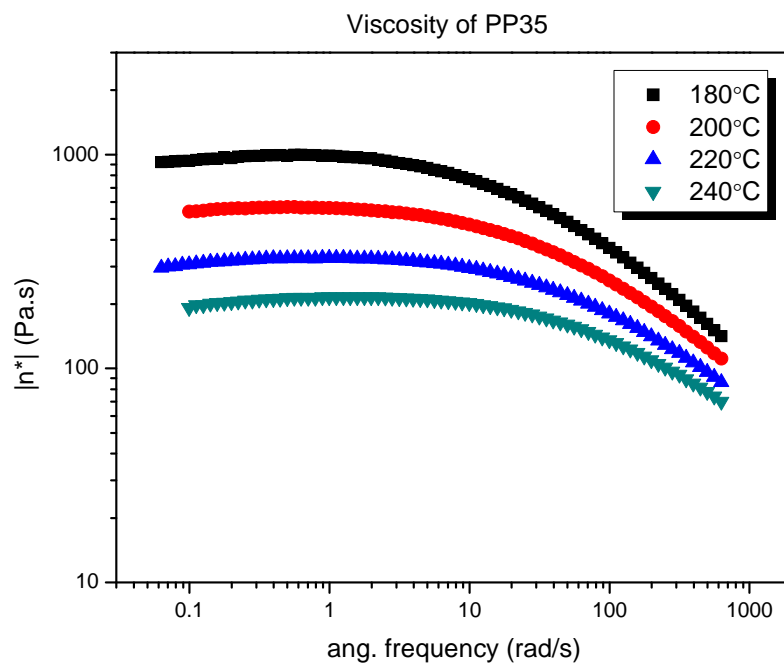


Figure 6.2 Viscosity of PP35 at different temperatures and angular frequencies.

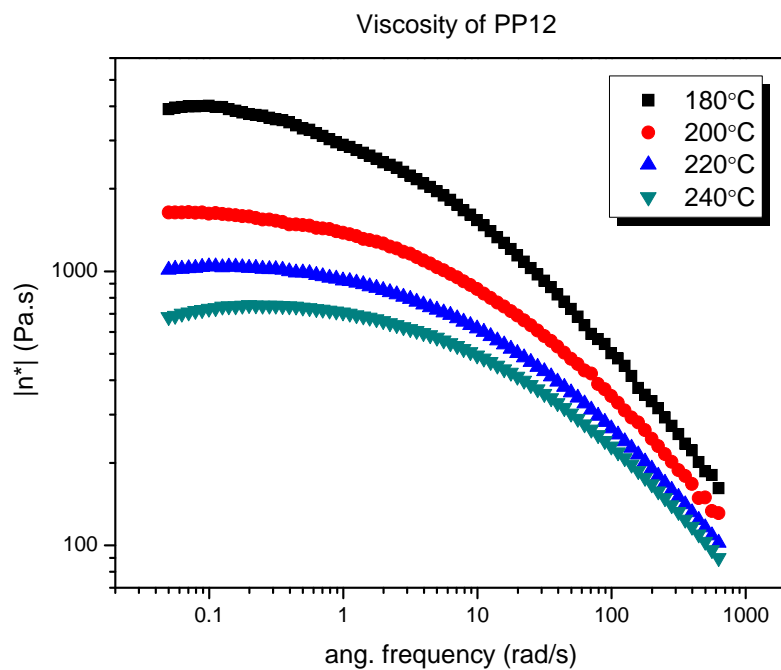


Figure 6.3 Viscosity of PP12 at different temperatures and angular frequencies.

Table 6-1 PP115 fiber diameters and their processing conditions.

<b>Air/polymer volume flow ratio</b>	<b>Average fiber diameter (<math>\mu\text{m}</math>)</b>	<b>Standard deviation (<math>\mu\text{m}</math>)</b>	<b>Processing temperature (<math>^{\circ}\text{C}</math>)</b>	<b>Diameter range (<math>\mu\text{m}</math>)</b>
42578	131.5	11.34	180	32~130
96865	46.6	1.79		
136065	40.5	1.06		
151685	31.7	0.73		
17463	70.9	1.24	200	30~70
67060	41.4	0.05		
82355	33.5	0.26		
134121	29.7	0.57		
101607	24.9	0.70	220	15~25
153681	19.5	0.20		
290596	15.9	0.59		
510939	14.9	0.34		
63867	25.4	0.17	240	8~25
69855	19.2	0.46		
279420	8.0	0.14		
447072	7.4	0.16		

Three different polypropylenes were used to study the effect of viscosity on final fiber diameters. The viscosities of these 3 PP's were tested by parallel plate rheometer and their viscosities were plotted against angular frequency for different temperatures, 180°C, 200°C, 220°C and 240°C. As shown in Figure 6.1, Figure 6.2 and Figure 6.3, the PP115 and PP35 have relatively similar viscosity. While PP12 has relatively higher viscosity compared with PP115 and PP35. As expected, the experimental results indicated that the PP115 and PP35 fibers exhibited similar fiber diameter distributions under same processing conditions. Therefore, we will mainly focus on comparing the PP115 and PP12 fibers in this section.

Table 6-2 PP12 fiber diameters and their processing conditions.

<b>Air/polymer volume flow ratio</b>	<b>Average fiber diameter (<math>\mu\text{m}</math>)</b>	<b>Standard deviation (<math>\mu\text{m}</math>)</b>	<b>Processing temperature (<math>^{\circ}\text{C}</math>)</b>	<b>Diameter range (<math>\mu\text{m}</math>)</b>
63867	669.3	1.52	180	93~670
107297	557.3	6.42		
638674	203.3	11.54		
993493	92.6	8.02		
134121	256.6	7.63		
178828	117.7	0.77	200	70~256
201182	115.1	3.48		
239502	73.2	0.38		
268243	69.0	2.88		
242164	133.6	2.61		
251478	69.0	1.72	220	30~134
402364	45.0	1.76		
536486	31.1	1.51		
647078	29.7	0.92		
298048	54.8	1.46		
357657	29.3	0.53	240	20~55
447072	19.7	0.10		

Table 6-1 and Table 6-2 summarized the fiber diameters and their processing conditions of PP115 fibers and PP12 fibers. These results reveal an obvious trend that the fiber diameter decreases with the increase of processing temperature. It is believed that the material viscosity is the real factor behind processing temperature since the viscosity is very sensitive to the temperature. When the temperature increases, the decreased viscosity causes more attenuation of melt filament and thus results in a smaller fiber diameter.

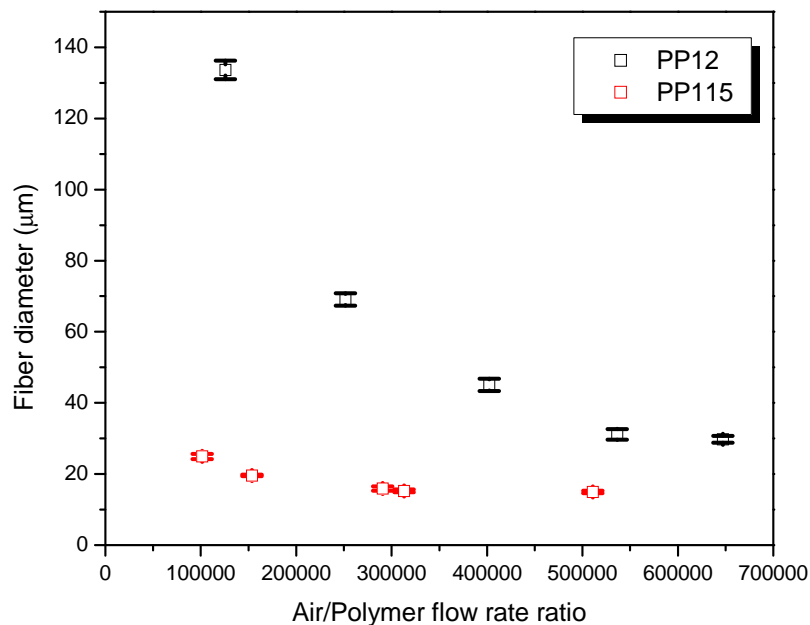


Figure 6.4 Fiber diameter of PP115 and PP12 made at 220°C.

It is also interesting to point out that a more scattered fiber diameter distribution appeared for the same processing temperature range when viscosity increased. For example, most of the fiber diameters fall into the range of 7-50  $\mu\text{m}$  for fibers made from low viscosity PP115. However, this range dramatically increases to 20-150  $\mu\text{m}$  for fiber made from higher viscosity PP12. As shown in Figure 6.4, at processing temperature 220°C, the PP12 fibers diameters vary from 30 to 140 microns, but the PP115 fiber diameters just scatter between 15-25  $\mu\text{m}$ . This can be explained by the viscosity data shown in Figure 6.1, Figure 6.2 and Figure 6.3. The zero shear rate viscosity of PP115 decreases gradually from about 400 Pa·s to 100 Pa·s when the temperature increases from 180°C to 240°C which shows a relatively small magnitude difference in viscosity at different temperatures. However, within the same temperature range, the zero shear rate viscosities of PP12 are approximately 4000 Pa·s, 2000 Pa·s, 1000 Pa·s and 700 Pa·s which shows a broader difference in viscosity. It can be concluded that the distribution of

fiber diameter is determined by the viscosity difference at different temperatures. A higher difference in viscosity will result in a wider distribution in the fiber diameter within the same processing temperature range.

### 6.1.2. Effect of Air/polymer Volume Flow Ratio

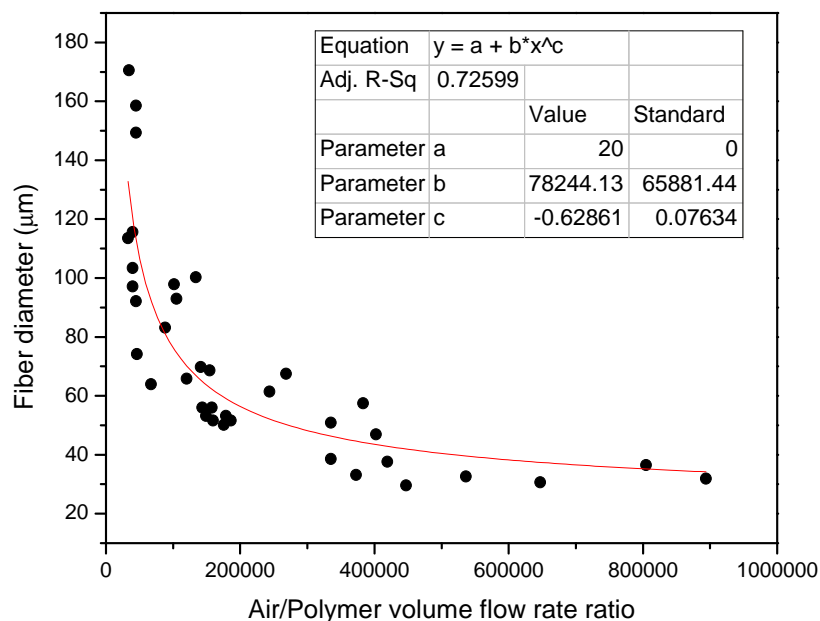


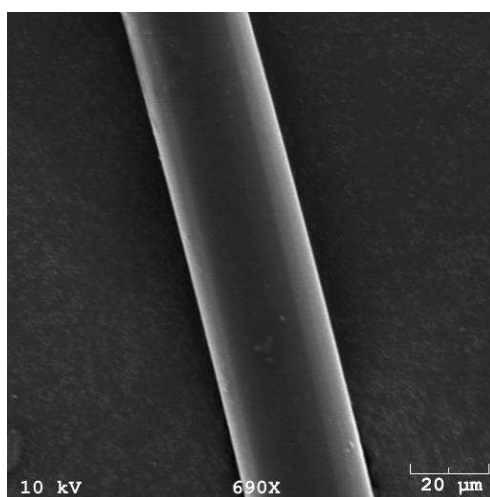
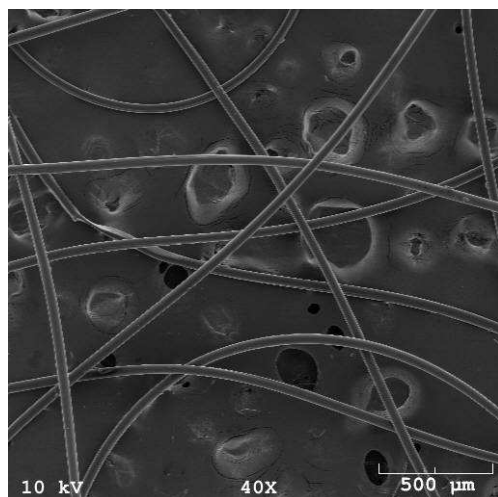
Figure 6.5 Data fitting of the relation between fiber diameter and air/polymer volume flow ratio.

In the previous section, it has been reported that the fiber diameter is also highly dependent on the air/polymer flow ratio. Basically, the fiber diameter decreases with the increase of the ratio. However, it is hard to draw a further conclusion since very limited data were presented. To generate more data points, PP12 was selected to produce fibers at 220°C with different air/polymer volume flow ratios. The viscosity of PP12 at 220°C is thought to be a proper viscosity which is high enough to apply different levels of air/polymer flow ratios.

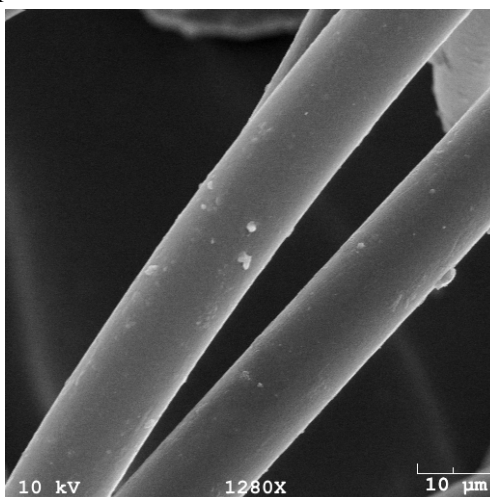
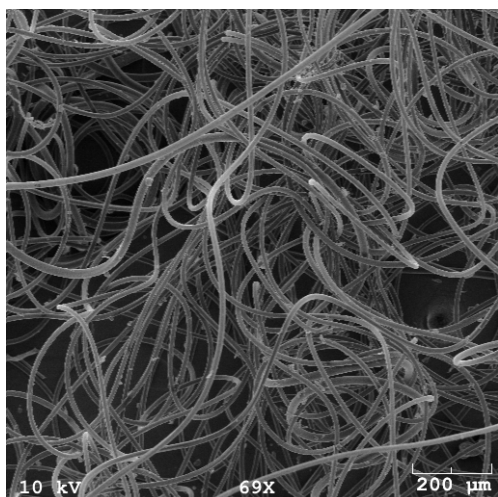
About 40 experiments were carried out and the results are plotted in Figure 6.5. The fiber diameter showed a strong correlation with the air/polymer volume flow ratio. When the ratio is below 200000, the fiber diameter drops severely with the increase of the ratio. Beyond that point, the fiber diameter still tends to decrease with increase of flow ratio, but the slope becomes flatter and finally tends to approach a horizontal line. This trend suggests that a power law equation in the form of  $y=a+b*x^c$  may be a good fitting on the data. In this equation, power index 'c' is assumed to be a negative value because the fiber diameter decreases with the increase of flow ratio. In this case, when the ratio goes to infinity the fiber diameter is approaching a constant value 'a'. In the data fitting, parameter 'a' was fixed at 20  $\mu\text{m}$  which is little bit smaller than the finest diameter (30  $\mu\text{m}$ ) achieved in the experiments. After regression, equation  $y=20+18400.91*x^{-0.62861}$  was selected to fit the data. A similar equation was fitted for a single hole melt blowing process reported by Haynes [96], but the physical meaning of the power index was not revealed.

### 6.1.3. Fiber Morphology

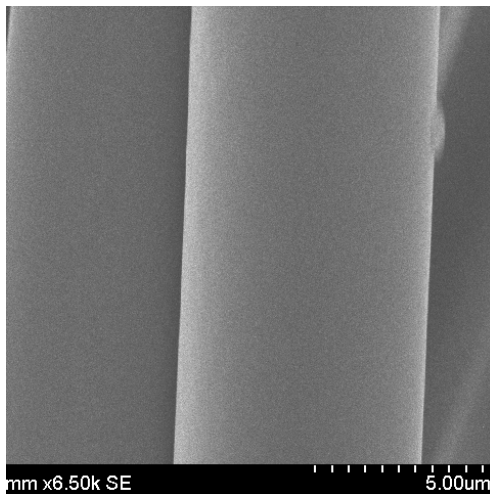
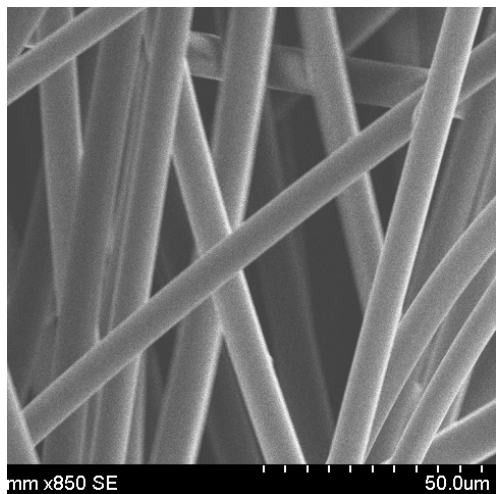
Figure 6.6 shows the SEM images of produced fibers with diameters of 25  $\mu\text{m}$ , 13  $\mu\text{m}$  and 7  $\mu\text{m}$ . From these images, it can be seen that the diameters of the resulting fibers are quite uniform and the fiber surfaces are also smooth. The smallest of the three, the 7  $\mu\text{m}$  fiber, was made from PP115 with processing temperature at 240°C. Note that all these fibers were produced only with jet stretching by cold air attenuation. From the mechanical testing results presented later, it will be seen that these fibers can be further extenuated for about four times or more if a drawing step follows.



25 μm



13 μm



7 μm

Figure 6.6 SEM photographs of fibers.

## 6.2. Fiber Molecular Orientation

The molecular orientation is an important property of fiber since it correlates to fiber crystallinity and mechanical properties. In our process, the fiber is attenuated by air drag force accompanied with cold air cooling. The molecular orientation was built up during the attenuation. To characterize the molecular orientation, two different methods were applied, wide-angle X-ray diffraction and Raman spectroscopy. Raman spectroscopy was chosen as the major technique because of its easy test procedure and data analysis. To validate this application of Raman on fiber molecular orientation, three PP115 fibers with different draw ratio were characterized by both Raman and WXR. The results are shown in Figure 6.7. In this figure, two fibers were made at 220°C with draw ratio 330 and 1600; the other fiber was made at 240°C with draw ratio 360. A Raman spectra of raw PP115 pellet was also included. It was reported the ratio of 841/809  $\text{cm}^{-1}$  band intensity can be used to estimate molecular orientation of isotactic polypropylene fiber [94, 95]. It can be observed that this ratio follows the same trend as the orientation results measured by WXR. These results indicate that Raman spectroscopy is an effective technique for characterizing the molecular orientation of the fibers produced in this study.



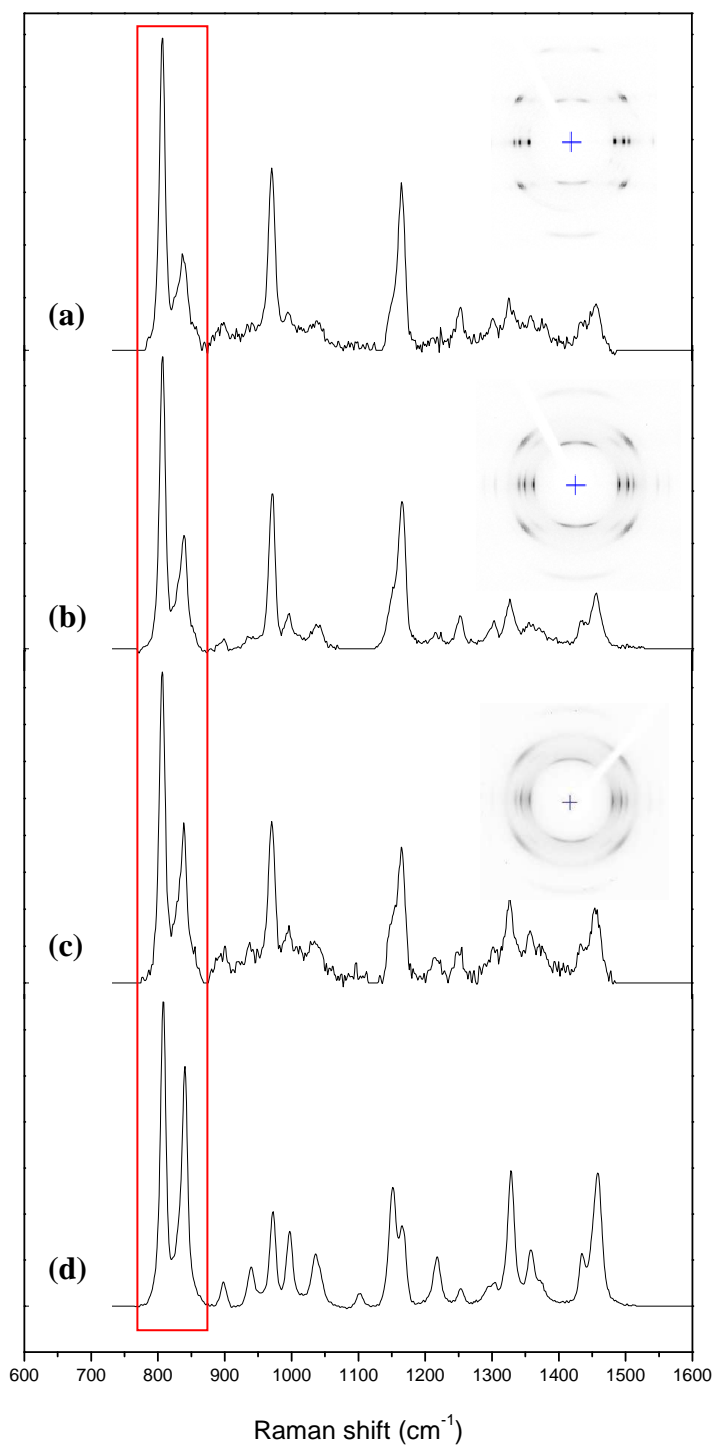


Figure 6.7 Typical ZZ polarized Raman spectra of PP115 fibers, compared with WXRD pattern. Fibers were made with different draw ratio at different temperatures (a) 1600 at 220°C; (b) 330 at 220°C; (c) 360 at 240°C; (d) control (raw PP115 pellet).

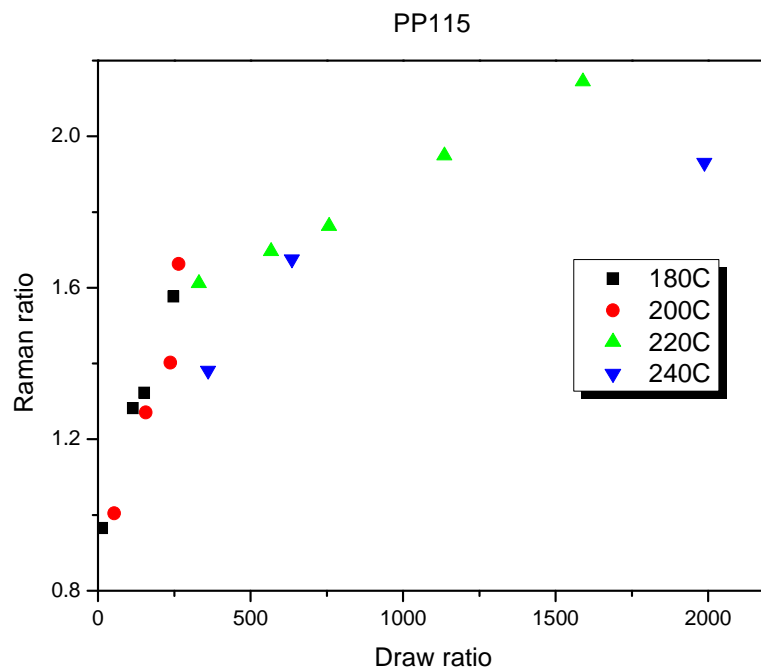


Figure 6.8 PP115 fiber molecular orientation estimated by Raman spectra.

The ratio of  $841/809\text{ cm}^{-1}$  band intensity is referenced to Raman ratio in this study. The Raman ratio of PP115 fibers was calculated from Raman spectra and plotted against draw ratio as shown in Figure 6.8. Based on the results, several trends can be observed: Firstly, at the same processing temperature, the fiber molecular orientation increases with increasing draw ratio resulted from the higher air drag force. As discussed in previous section, the fiber diameter decreases with increasing air/polymer flow ratio. Therefore, it is believed that the fiber molecular orientation also increases with the flow ratio. Secondly, with the same draw ratio, lower processing temperature generally leads to higher orientation because of reduction of relaxation time. Thirdly, the gradient of Raman ratio over draw ratio decreases with increase in processing temperature which may also be explained by the reduction of relaxation time. When the temperature or draw ratio increases, this linear relation either disappears or the slope decreases.

### **6.3. Crystallization Behavior of Resulting Fibers**

As discussed in the literature review section, the polymer crystallization behavior is crucial during structure formation. In this modified melt spinning process, the spinline dynamics is different from that in melt blowing or traditional melt spinning. The new thermal and mechanical environment along the spinline is expected to affect the fiber crystallization behavior which can finally affect the fiber mechanical properties. In this section, the results on the fiber crystallization behavior are presented with discussion provided on crystallinity, crystal form and crystal size.

#### **6.3.1. Crystallinity**

The fiber crystallinity was calculated based on the fusion enthalpy from the DSC tests. Figure 6.9 shows the crystallinity of fibers made from PP115 under various processing conditions. Figure 6.10 shows the results of PP12. No obvious trends were found between the fiber crystallinity and processing conditions. For PP115 fiber, the fiber crystallinity scattered within the region of  $50\% \pm 3\%$ . It decreased to  $42\% \pm 2\%$  for PP12 fiber because high viscosity PP12 has longer molecular chains which make them more difficult to crystallize.

Since the fibers were produced under various conditions with temperature from  $180^{\circ}\text{C}$  to  $240^{\circ}\text{C}$  and air flow rate from 1 cfm to 6 cfm, it is expected that these conditions should somehow affect the fiber crystallinity. The crystallinity measured by DSC may not be accurate because the recrystallization may occur during the heating. Therefore, WXRd test was performed to study the fiber crystallization behavior.

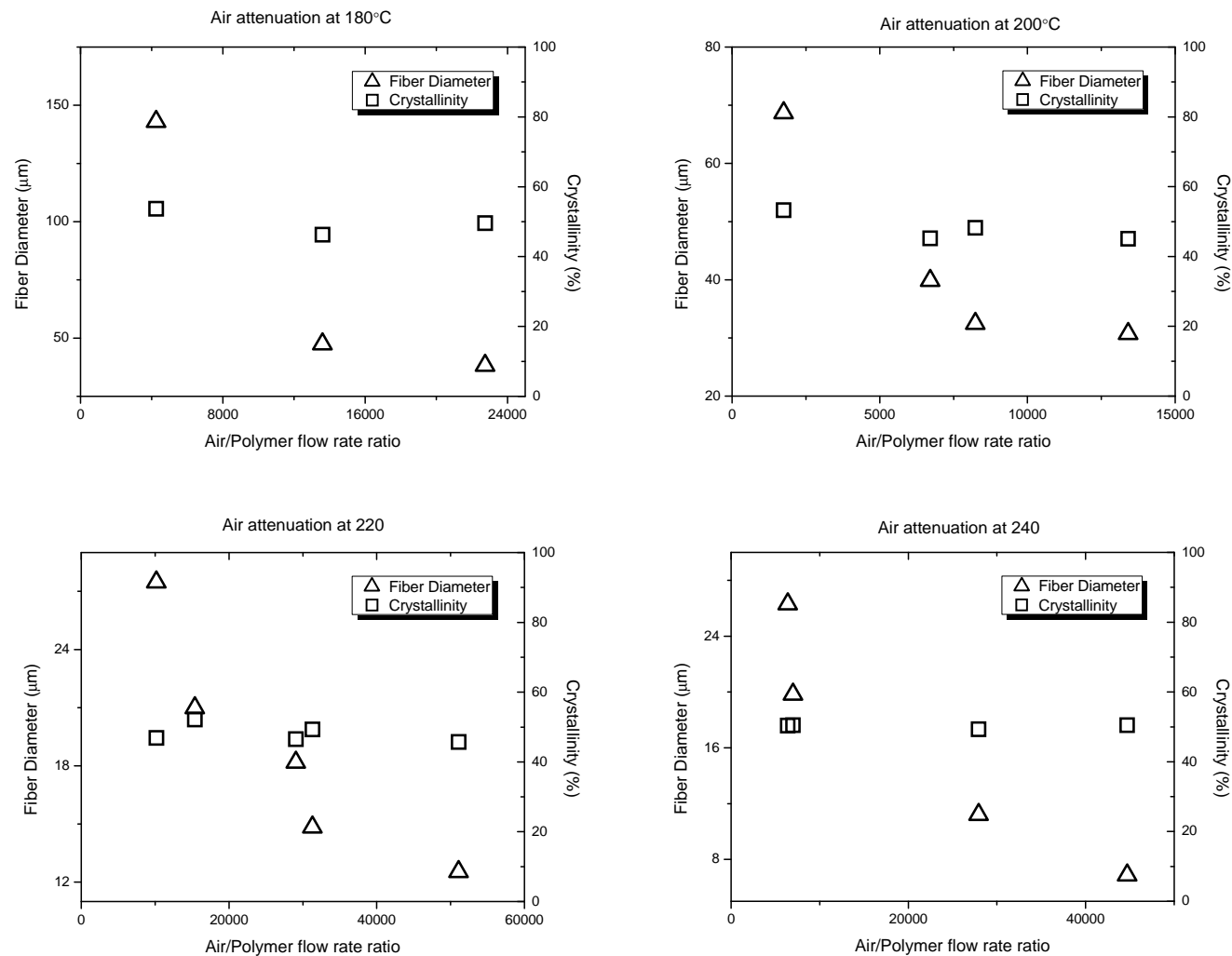


Figure 6.9 Crystallinity of resulting fibers made from PP 115 at different temperatures.

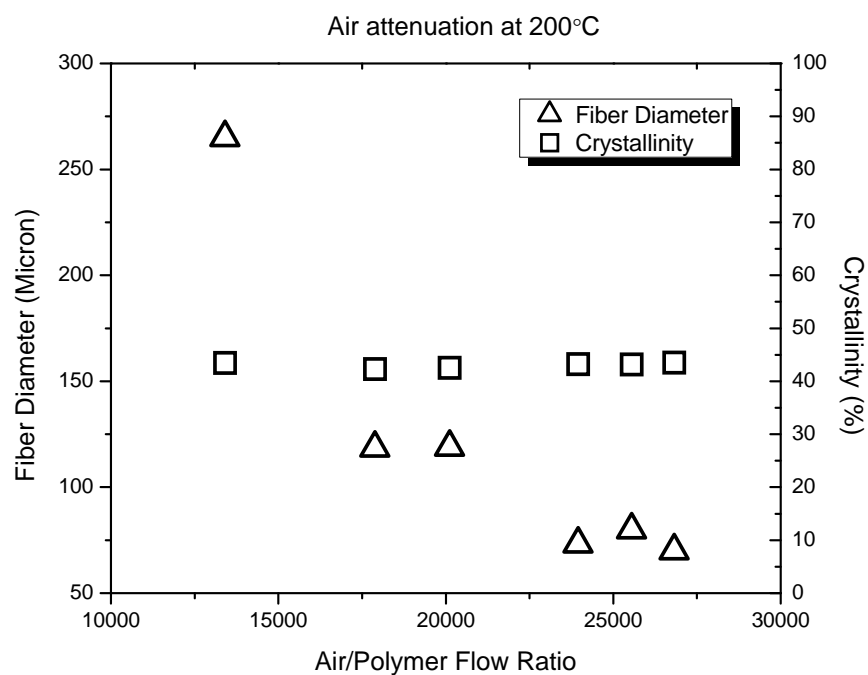
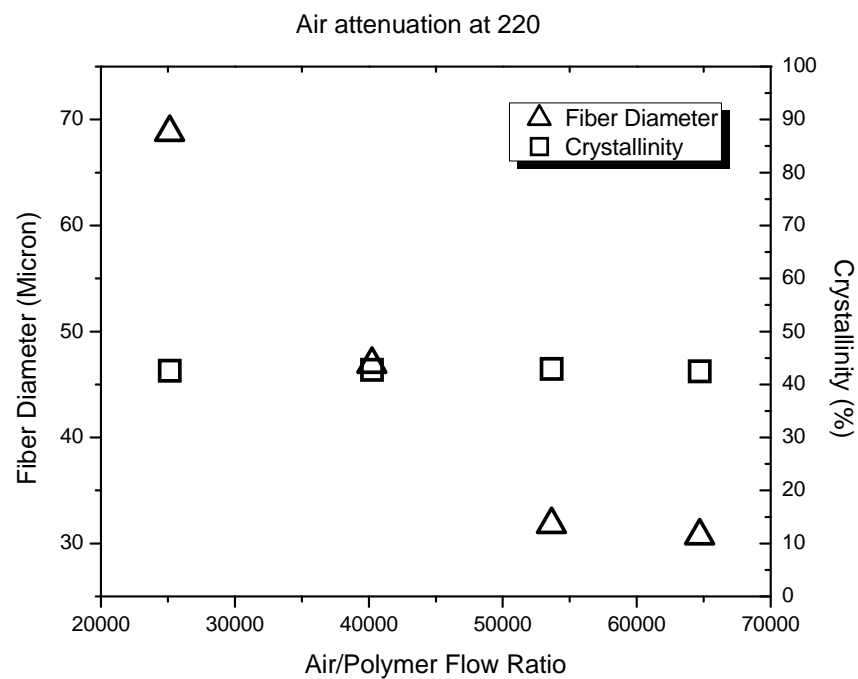


Figure 6.10 Crystallinity of resulting fibers made from PP 12 at different temperatures.

The wide-angle X-ray diffraction patterns of PP115 fibers produced under different conditions are presented in Figure 6.11. In contrast to the DSC results, the WXRd results reveal that fiber crystallinity is related to the processing temperature and the air/polymer flow ratio. The fibers made at three temperatures 180°C, 220°C and 240°C were tested and compared. Although only 2 samples were presented at 180°C, it can be seen that the crystallinity increases when the air/polymer flow ratio increases from 13000 to 23000. The same trend was observed for the crystallinity of fiber made at 240°C. However, at 220°C, the crystallinity remained nearly constant and showed no dependence on the air/polymer flow ratio. In addition, the fibers made at lower temperatures had higher crystallinity than those made at higher temperatures.

It is well known that the crystallization behavior is affected by two competitive factors, the cooling rate and the crystallization rate. In high speed melt spinning, the crystallinity was found to increase with increasing take-up speed because high crystallization rate occurred with high spinning stress and high orientation [87]. In our modified melt spinning process, the high speed cold air temperature is close to the room temperature (25-30°C) which is well above the glass transition temperature of polypropylene. Although the high speed air flow helps to cool the melt filament fast, it is not sufficient to immediately quench the melt filament. Therefore, as a fast crystallization polymer, the polypropylene filaments still undergo crystallization. Furthermore, the high orientation formed during the attenuation with the assist of cold air cooling also plays an important role in fiber crystallization. An empirical equation can be used to explain the

effect of crystallization temperature and degree of orientation on the fiber crystallization behavior [24]:

$$K(T, f) = K(T, 0) \exp(Af^2) = K_{\max}^0 \exp[-4 \ln 2 (T - T_{\max}^0)^2 / D_0^2 + A(T)f^2] \quad (24)$$

where K is crystallization rate, A(T) is a positive parameter, f is orientation factor,  $K_{\max}$  is the maximum crystallization rate,  $T_{\max}$  is the temperature where maximum crystallization occurs, and D is the half width of K(T) curve. For isotactic polypropylene,  $K_{\max}=0.55$ ,  $T_{\max}=65^\circ\text{C}$  and  $D=60$ , and the equation can be rewritten to:

$$K(T, f) = 0.55 \exp[-4 \ln 2 (T - 65)^2 / 3600 + A(T)f^2] \quad (25)$$

In the above equation, there is a negative term and a positive term. The cold air cooling in our process makes the temperature close to  $T_{\max}=65^\circ\text{C}$ . Hence it makes this negative term even smaller. On the other hand, the high orientation will make the positive term even larger. Mathematically, the crystallization rate is increased by the low processing temperature and high molecular orientation. In our process, the orientation increases with increasing air/polymer flow ratio as shown in Figure 6.11. Consequently, the increase of air/polymer flow ratio will cause increasing crystallization rate which finally leads to the increase of crystallinity. At temperature  $180^\circ\text{C}$  and  $240^\circ\text{C}$ , the significant increases in orientation result in an increase of crystallinity with increasing air/polymer flow ratio. At  $220^\circ\text{C}$ , the resulting fibers exhibit relative higher crystallinity due to the extremely high orientation and modest processing temperature. Only slight increases on crystallinity are observed with the increase of air/polymer flow ratio. This is because that the fiber crystallinity may reach some limited value under those processing conditions.

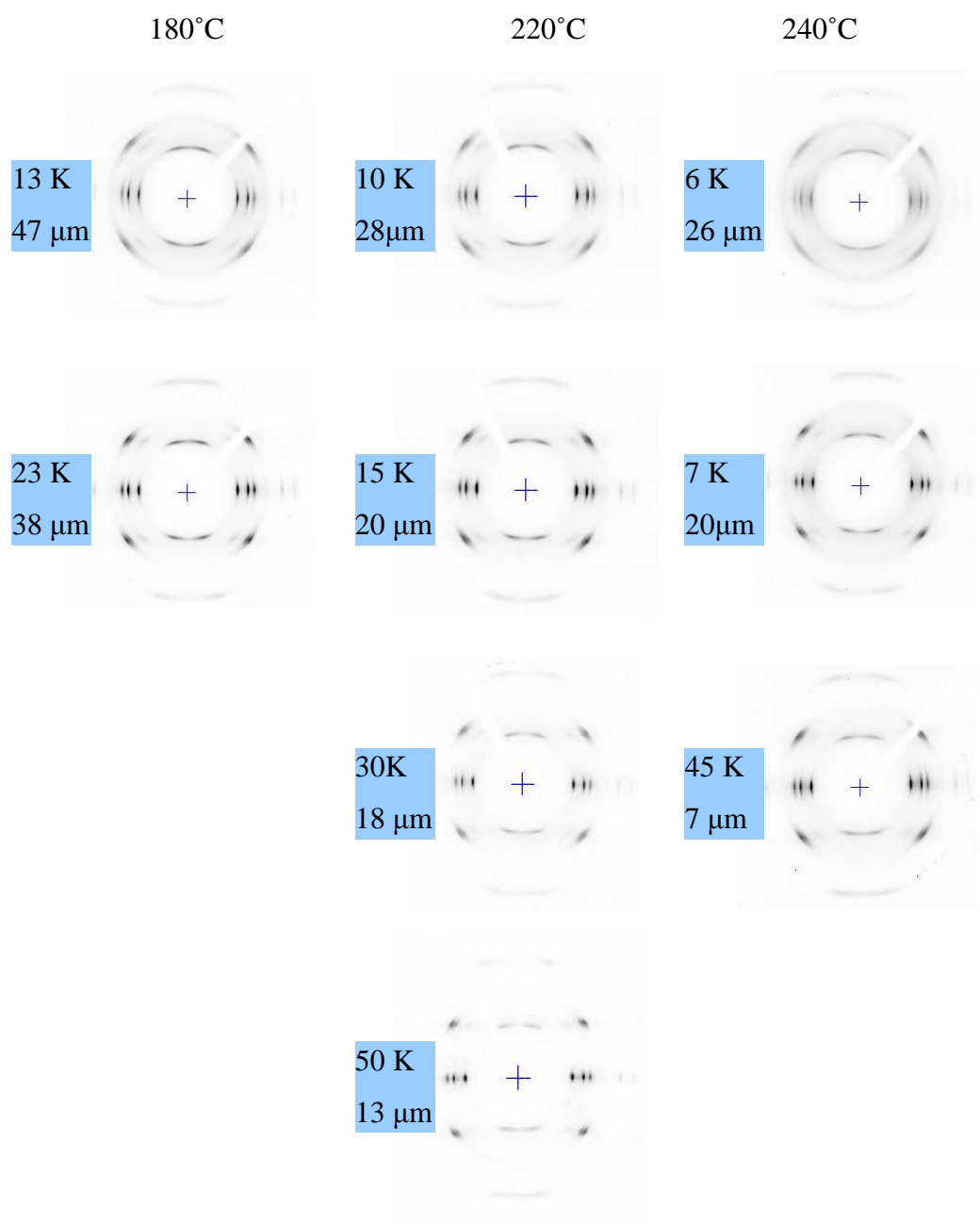


Figure 6.11 Wide-angle X-ray diffraction patterns of PP115 under various processing conditions. Inside the shaded box, the first number indicates the air/polymer flow ratio; the second one is the resulting fiber diameter.



### 6.3.2. Crystal Form and Crystallite Size

The WXRD spectra shown in Figure 6.12 exhibits a typical crystal form for fibers made from isotactic PP. Three strong peaks located at  $2\theta=14.2^\circ$ ,  $17.1^\circ$  and  $18.6^\circ$  indicate the  $\alpha$ -monoclinic reflections of 110, 040 and 130 planes. Crystallization of isotactic polypropylene is a complicated process which can form three different crystal forms,  $\alpha$ -monoclinic,  $\beta$ -hexagonal and  $\gamma$ -triclinic. The  $\beta$ -hexagonal and  $\gamma$ -triclinic may be formed under fast quench or high pressure or by introducing special nucleating agents. In melt spinning,  $\alpha$ -monoclinic is usually obtained under the conditions of mild quench with modest to high spinline stresses. Therefore, the formation of  $\alpha$ -monoclinic crystal indicates that the high speed cold air provides mild quench effect on melt filament.

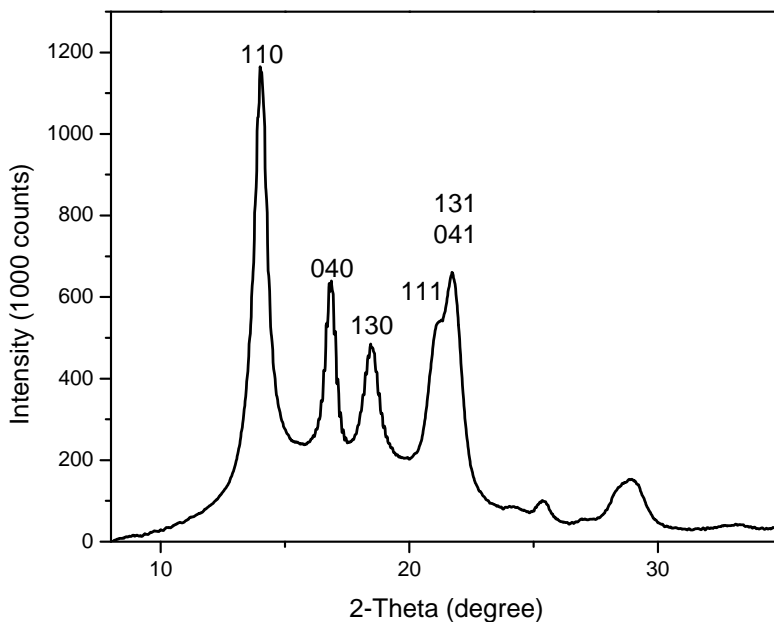


Figure 6.12 WXRD spectra of typical PP115 fibers made at 220°C.

The crystallite size of 110 plane for PP115 fiber was calculated based on Scherer's equation and the results are listed in Table 6-3. The typical crystallite size is about 120Å

for the PP115 fiber made at 220°C.

Table 6-3 Crystallite size and  $2\theta$  value of 110 plane of PP115 fiber made at 220°C.

PP115 fiber with diameter ( $\mu\text{m}$ )	$2\theta$ ( $^\circ$ )	Crystallite size ( $\text{\AA}$ )
27.5	14.050	116.5
21.0	14.022	127.2
18.2	14.028	125.4
12.5	14.014	127.8

#### 6.4. Fiber Mechanical Properties

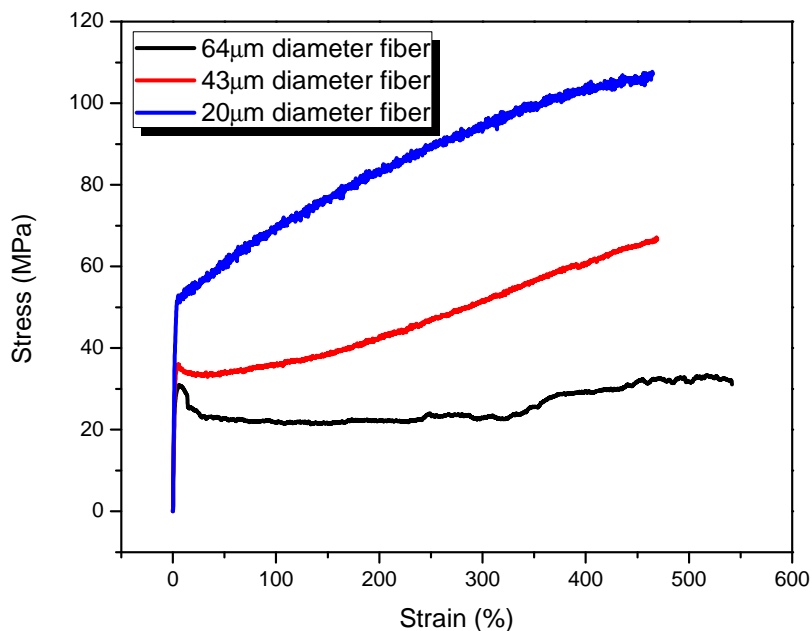


Figure 6.13 Typical stress-strain curves of single filament.

Tensile tests were performed on an Instron machine. The stress-strain curves were recorded for the calculation of tensile strength and tensile modulus. Figure 6.13 shows the typical stress-strain curves observed in a single filament tensile test. With the increase of strain, the fiber undergoes elastic deformation, yielding, necking and strain hardening.

It was observed that the necking deformation becomes insignificant and finally disappear with the decrease of origin fiber diameter. This can be described as a transition from (a) to (b) to (c) as shown in Figure 6.13. In this study, curve (a) usually represents fiber with diameter above 50  $\mu\text{m}$ ; curve (b) corresponds to the fiber with diameter in the regime of 20-50  $\mu\text{m}$ ; and curve (c) is for the fiber with diameter under 20  $\mu\text{m}$ .

The ultimate tensile strength is dependent on the elongation at break because of the strain hardening effect. Therefore, tensile stress at 200% elongation was chosen as the representative strength for comparison in this study. Both strength values were plotted against the initial fiber diameter.

Figure 6.14 and Figure 6.16 show the single undrawn fiber tensile strength results made from PP115 and PP12 respectively.

Figure 6.15 summarizes the tensile modulus of PP115 fibers. For low viscosity PP115, the single filament with diameter of 10  $\mu\text{m}$  can reach tensile strength of 100 MPa and 2.5 GPa. For high viscosity PP12, the tensile strength increases to 140 MPa for single filament with diameter of 25  $\mu\text{m}$ . The tensile strength and modulus showed a dependence on fiber diameter for both PP115 and PP12. This is because fiber mechanical properties strongly depend on molecular orientation and crystallinity which is also a function of molecular orientation in our process as discussed previously. Generally, the increase of orientation will lead to increases in tensile strength and modulus. It was found in our study that the molecular orientation increases as fiber diameter decreases. Consequently, fiber tensile strength and modulus increase with decreasing of fiber diameter. Since the fiber mechanical properties are very sensitive to processing conditions, the tensile strength and modulus scattered around a linear relation with fiber diameter. The outliers

observed at diameter of 25  $\mu\text{m}$  for PP115 and 55  $\mu\text{m}$  for PP12 represent the fibers made at relatively high temperature with low air drag force. Therefore, the resulting low molecular orientation and crystallinity lead to the low tensile strength and modulus.

To obtain high strength fibers, these processing conditions should be optimized in the way to form high molecular orientation: firstly, a modest processing temperature which can provide proper viscosity for enough attenuation and longer relaxation time for overcoming the disorder in molecular orientation; secondly, high air flow to generate high air drag force to enhance molecular orientation.

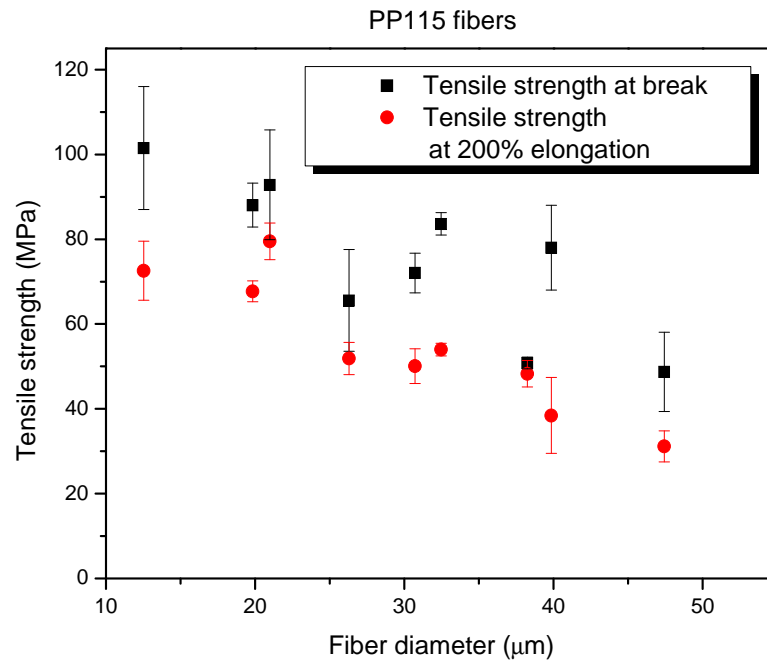


Figure 6.14 Tensile strength of PP115 fibers.

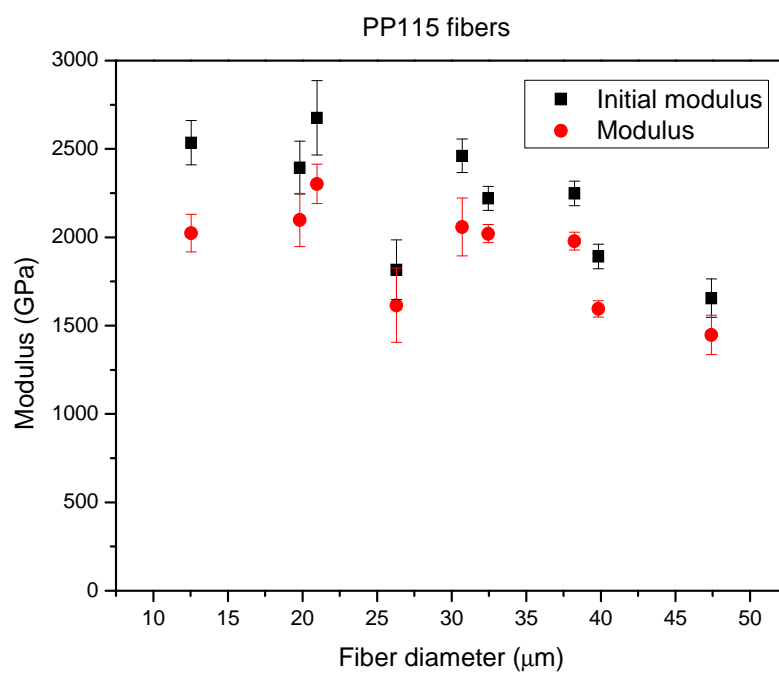


Figure 6.15 Tensile modulus of PP115 fibers.

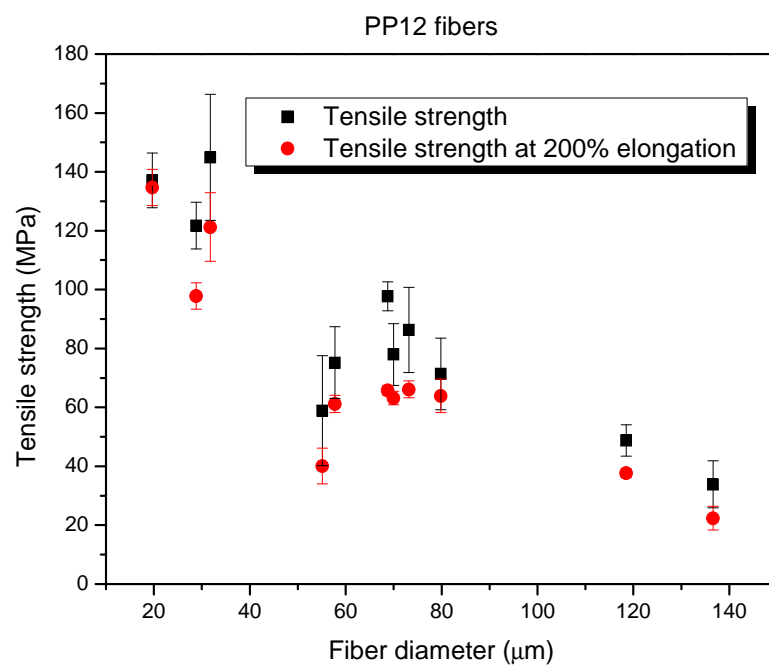


Figure 6.16 Tensile strength of PP12 fibers.

### 6.5. Melting and Crystallization Temperature

The melting and crystallization temperature of PP115 fiber were measured by DSC and listed in Table 6-4. The crystallization temperature varies between 113.93°C and 120.66°C with heating and cooling rate at 20°C/min in DSC. There is no apparent correlation between the processing temperature and fiber diameter. The melting temperature shows some dependence with the processing conditions. At lower processing temperature 180°C and 200°C, the melting temperature slightly increases by about 1°C when the fibers diameter decreases from 70  $\mu\text{m}$  or larger to 30  $\mu\text{m}$ . When processing temperature further increases to 220°C, uneven broad endotherm peaks with peak maximum at lower temperature side were observed. The uneven broad endotherm peaks were observed to clearly split into two peaks for the fibers produced at 240°C with diameters less than 15  $\mu\text{m}$ . The first peak located at 165°C corresponds to the normal melting point of PP115 and the second one appears at about 170°C.

Figure 6.17 shows all types of endotherm peak shapes described. The second endotherm peak located at 169°C is gradually developed as processing temperature increases and fiber diameter decrease. The appearance of two melting points was also reported in previous studies as discussed in the literature review chapter. Usually, it is caused by the formation of different crystal forms and crystallite size under certain processing conditions, or by the recrystallization during the heating and cooling environment in DSC scanning.

Table 6-4 Melting and crystallization temperatures of resulting fibers.

Processing temperature (°C)	Fiber diameter (μm)	T <sub>m</sub> (°C)	T <sub>c</sub> (°C)
180	143	164.50	120.66
180	47	166.19	115.70
180	38	166.00	118.48
200	69	164.81	118.47
200	40	165.62	116.13
200	32	165.85	118.80
200	31	165.67	113.93
220	27	164.62*	115.89
220	21	164.89*	120.05
220	18	164.75*	116.75
220	15	164.89*	118.05
220	13	165.10*	116.93
240	26	165.54*	118.38
240	20	164.88*	119.15
240	11	164.72 170.51	118.27
240	7	163.98 169.27	116.84

\*a broad endotherm peak observed

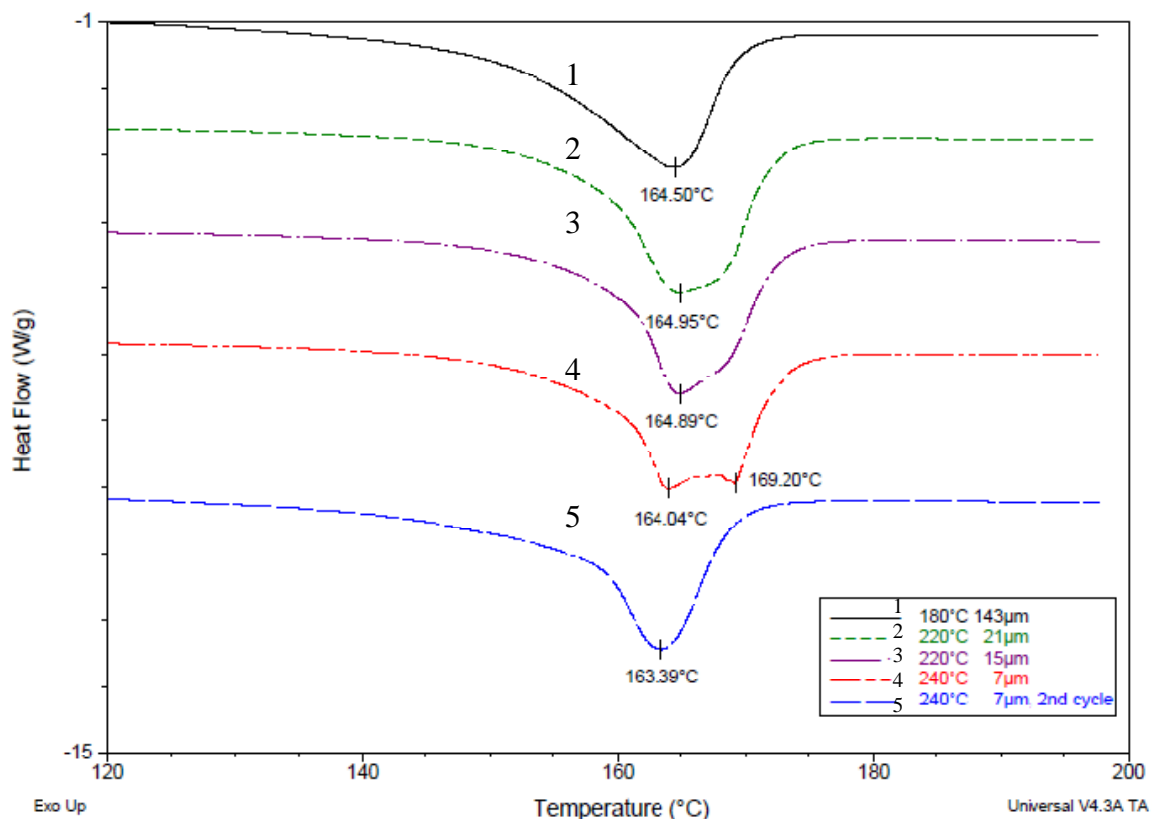


Figure 6.17 DSC heating thermograms of PP115 fibers with different endotherm peak shapes.

WXR D was performed on the fibers with and without double melting peaks to determine if there are new crystalline forms developed. The WXR D spectra patterns are shown in Figure 6.18. Both WXR D spectra patterns exhibit the typical  $\alpha$ -monoclinic crystalline form with strong reflection at  $2\theta=14.2^\circ$ ,  $17.1^\circ$  and  $18.6^\circ$ . Usually, isotactic polypropylene has  $\beta$ -hexagonal and  $\gamma$ -triclinic crystalline forms with character reflections at  $2\theta=16.08^\circ$  for  $\beta$  300 plane and  $2\theta=20.1^\circ$  for  $\gamma$  130 plane respectively. However, neither of these two reflection peaks was observed in our sample. Therefore, it can be concluded that there is no new crystalline form developed in the resulting fibers.



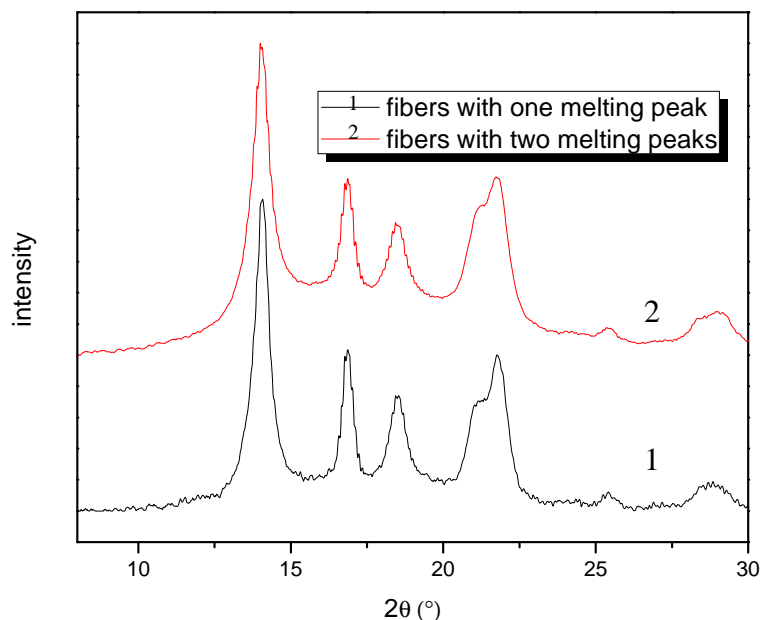


Figure 6.18 WAXRD spectra patterns of fibers with one or two melting peak(s) in DSC.

We further investigated whether this double melting peaks phenomenon was caused by the DSC testing thermal environment. Firstly, the sample fiber was heated and then cooled for two cycles at the same rate of 20°C/min. As shown in Figure 6.17, the double peaks were only observed at the first heating cycle, indicated by the line 4. After another cooling and heating cycle, the double peaks disappeared and only one normal endotherm peak appeared with peak maximum at 163.39°C as indicated by the line 5. Secondly, the sample fibers were tested under different heating rate with the range from 5°C /min to 40°C /min. The DSC curves are presented in Figure 6.19. At small heating rate 5°C /min, only an uneven endotherm peak was observed. With the increase of heating rate, another peak at higher temperature starts to split out and becomes more obvious at heating rate of 20°C/min. Then the second peak becomes blunt again as the heating rate increases to 40°C/min. Overall, the double endotherm peaks can be observed under different heating

rate in DSC. The recrystallization effect may weaken the appearance of the second endotherm peak under low heating rate. Moreover, the blunt appearance of the second peak under fast heating rate may result from the low resolution at extremely high heating rate since the sample does not have enough time to react. With the two previous steps, it can be confirmed that the formation of double melting peaks is not caused by the DSC testing thermal environment. In other word, the double melting peaks do not result from the recrystallization during the heating process in DSC.

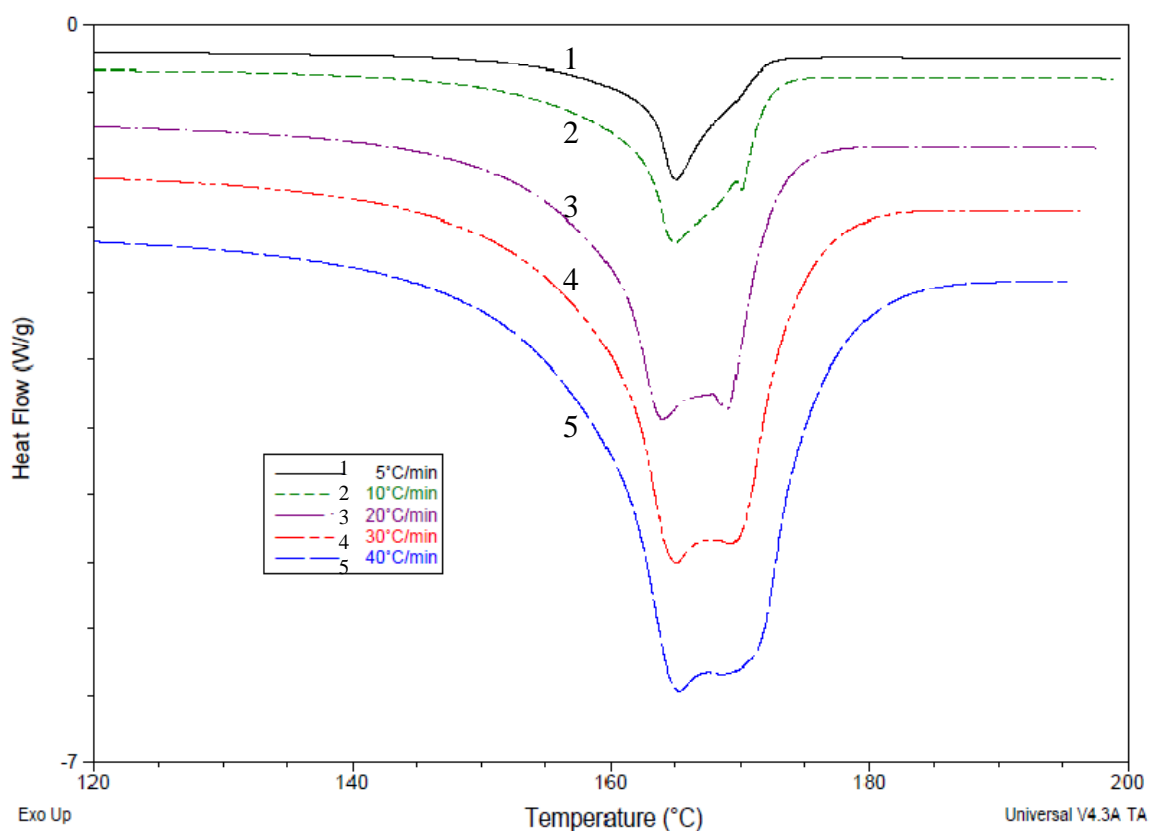


Figure 6.19 DSC heating thermograms of PP115 fibers made with various heating rate.

Based on previous conclusions, it is expected that the double melting peaks may result from the high orientation in those fibers with diameter under 15  $\mu\text{m}$ . A test was designed to prove this hypothesis. Fibers with only one melting peak were manually drawn about 3 times at room temperature to reach a final diameter of 15  $\mu\text{m}$ . Then the

same DSC scanning procedure was performed on both the drawn and original undrawn fibers. The results are presented in Figure 6.20 for both fibers with 2 heating and cooling cycles. Compared with the original undrawn fiber, the cold drawn fibers showed a broader endotherm peak appears in the first cycle. This broad peak has maximum covering from 165°C to 170°C which can be assumed to be the double peak's maximum with further drawing. After another cooling and heating cycle in DSC scanning, the broad melting peak is replaced by a normal single melting peak which is the same as the undrawn fibers.

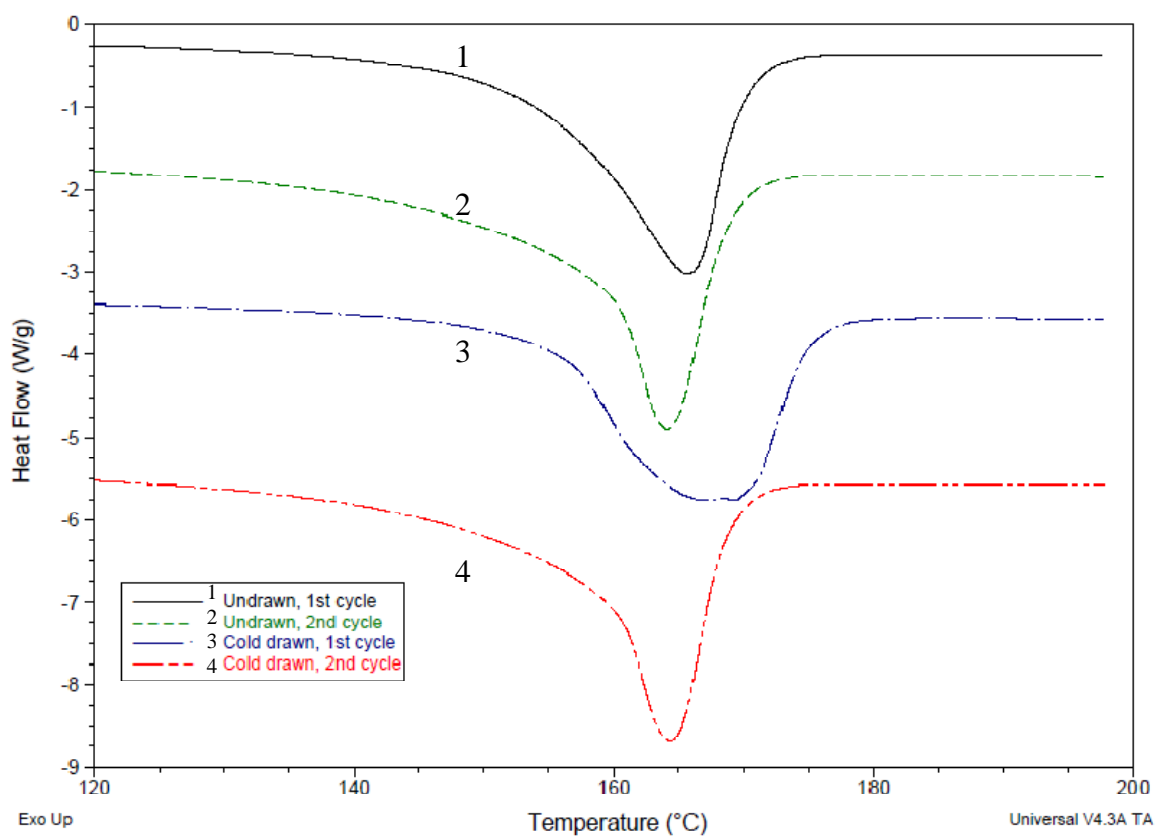


Figure 6.20 DSC heating thermograms of cold drawn and original undrawn PP115 fibers.

With all these evidences, it is believed that the appearance of double endotherm peaks in DSC is related to the fiber's high molecular orientation. A high orientation may cause some modification on the  $\alpha$ -monoclinic crystal structure which is reflected as double

melting peaks. Moreover, this kind of modification on crystal structure does not lead to a new crystal form.

## 6.6. Comparisons with Traditional Melt Spinning

### 6.6.1. Fiber Properties

Table 6-5 Fiber properties of fibers made by traditional melt spinning.

Processing temperature (°C)	Fiber diameter (μm)	Raman ratio (°C)	Crystallinity (%)	Tensile strength at 200% elongation (MPa)	Tensile strength at break (MPa)
180	63.9	1.44	47.8	20.7	34.3
200	21.7	1.75	48.9	62.7	95.8
200	13.7	2.01	49.2	95.5	107.3

For comparison, traditional melt spun fibers were produced on our fiber extruder with mechanical drawing. The resulting fibers were characterized to determine their properties, including fiber diameter, crystallinity, tensile strength and molecular orientation. Table 6-5 summarizes these properties of fibers made from PP115 with processing temperature at 180 and 200°C. These fibers exhibit similar properties as those made by cold air attenuation process. Compared with traditional melt spinning process, the new process could produce continuous filaments with comparable properties.

### 6.6.2. Cost Analysis and Possibility of Scale up

The use of compressed cold air introduces an additional cost in this new process as compared with traditional melt spinning process. In previous section, the relationship between fiber diameter and air/polymer volume flow ratio was investigated. For example,

to produce PP115 fibers with diameters of 8 to 25  $\mu\text{m}$  at processing temperature 240°C, the air/polymer volume flow ratio varied from about 63000 to 450000 for the air nozzle with tunnel diameter of 5 mm. Respectively, 0.07m<sup>3</sup> air is needed to produce 1 g continuous fibers with diameter of 25  $\mu\text{m}$  and 0.5 m<sup>3</sup> air is needed to produce the same amount of fibers with diameter of 8  $\mu\text{m}$ . The usage of air can be significantly reduced by using a smaller diameter air nozzle or using an extrusion die with multiple orifices. With multiple orifices on a slot die, this new process may be scaled up for industry application to produce continuous filaments or yarns.

### 6.7. Fibers Made from Nylon 6

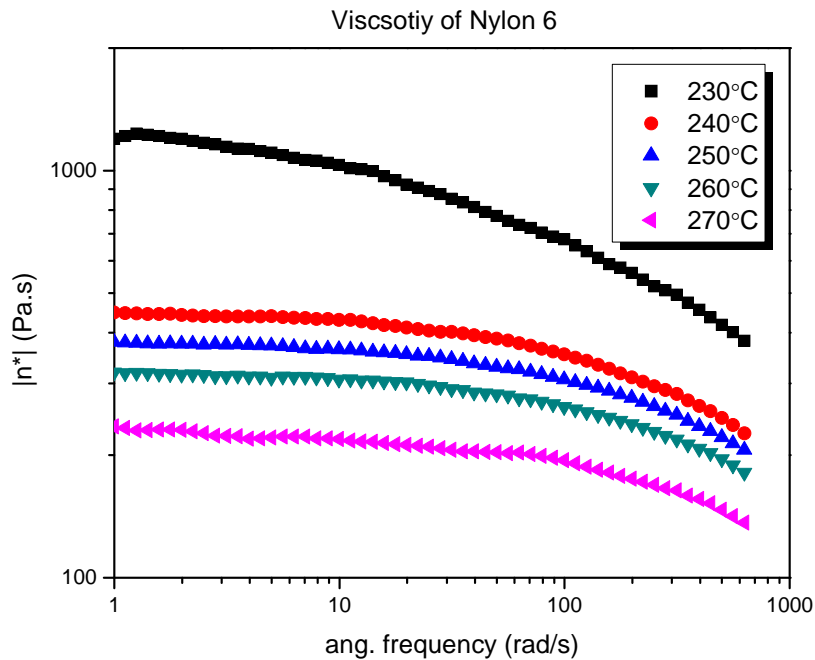


Figure 6.21 Viscosity of Nylon-6 at different temperatures and angular frequencies.

For demonstration, this process was also successfully applied to other polymer materials, including Nylon-6, a widely used polymer in the fiber industry. The melting point of Nylon-6 is about 225°C according to the DSC test. Figure 6.21 shows the

viscosity data of Nylon-6 tested at different temperatures. Compared with the viscosities of PP35 at the temperature in the region of 180°C-240°C, Nylon-6 has similar viscosities at the temperature in the region of 230°C-270°C. Based on previous polypropylene results, fiber diameter is majorly determined by the polymer viscosity. It is believed that the Nylon-6 fibers with diameter of 10-20  $\mu\text{m}$  can be produced at the temperature in the range of 230°C-270°C.

Since the processing temperature is limited by the Teflon insulation piece to below 260°C, the experiments were conducted at three different temperatures: 240°C, 250°C and 255°C. As expected, the fibers produced at low temperatures will have relatively large diameters. Therefore, the major experiments were conducted at 255°C with various air/polymer flow ratios for comparison. The resulting fiber properties are listed in Table 6-6.

Fiber diameters were plotted against the air/polymer flow ratio as shown in Figure 6.22. The fiber diameter decreases with the increase in flow ratio before it reaches some minimum value at a high air/polymer flow ratio. Both fiber tensile strength and tensile modulus also increase with the increase of flow ratio. The single filament with diameter of 10  $\mu\text{m}$  has a tensile strength of 216 MPa and modulus of 1.2 GPa. Figure 6.23 shows a polarized microscopy image of a single fiber with diameter about 25  $\mu\text{m}$ . It also indicates a uniform distribution of molecular orientation along the fiber surface.

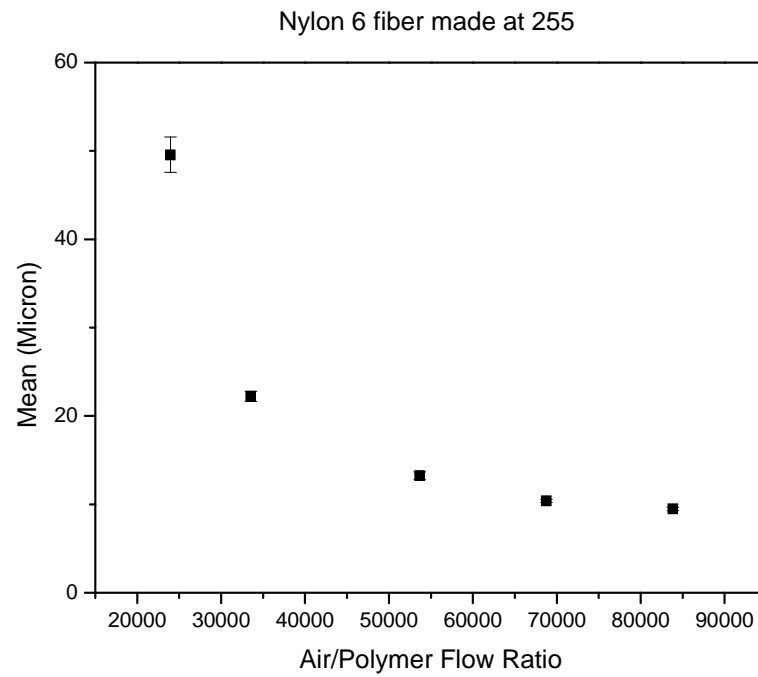


Figure 6.22 Nylon-6 fiber diameter versus air/polymer flow ratio.

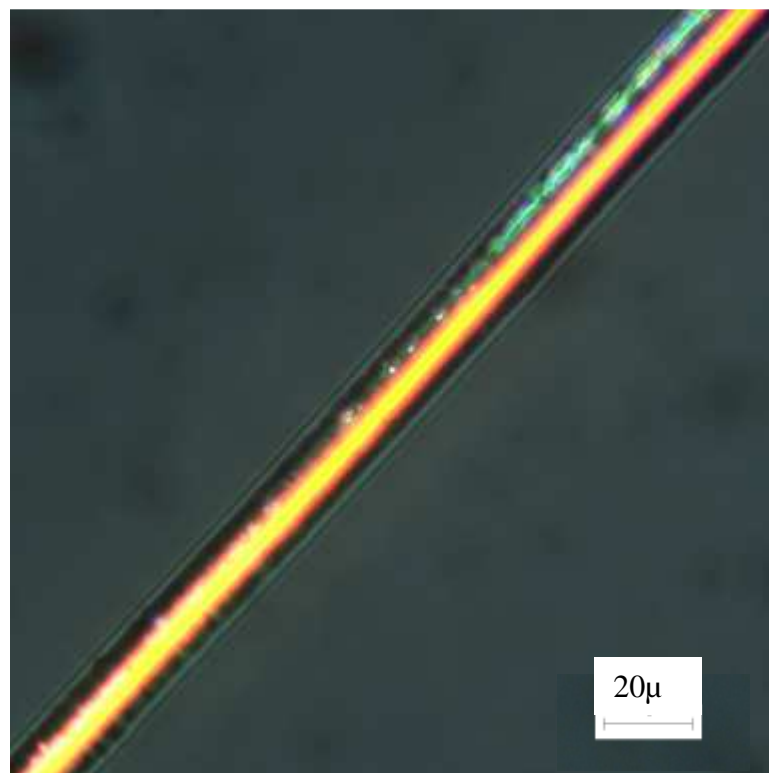


Figure 6.23 Polarized microscopy image of Nylon-6 fiber.

Table 6-6 Processing conditions and resulting fiber properties of Nylon-6 fibers.

Temperature (°C)	Air/ Polymer Ratio	Fiber Diameter (μm)	Crystallinity (%)	Tensile Strength at Break (MPa)	Elongation Ratio at Break (%)	Tensile Stress at 40% Elongation (MPa)	Modulus at 4% strain (MPa)
240	12418	179	29.95	79.7	354	44.3	944.4
250	4064	83	33.24	39.6	203	15.1	231.8
255	2395	50	36.94	74.6	391	19.0	300.9
255	3353	22	35.46	86.7	83	49.3	436.3
255	5364	13	36.36	199.2	71	134.9	861.4
255	8941	9	37.61	216.7	57	171.8	1171.2



## **CHAPTER 7**

### **THEORETICAL ANALYSIS AND MODELING OF COLD AIR ATTENUATION IN MELT SPINNING PROCESS**

#### **7.1. Introduction and Objectives**

As discussed in the previous chapter, the experimental results showed that the final fiber diameter depends on the polymer viscosity, processing temperature, polymer and air volume flow rates. Although in Chapter 4, CFD simulations were conducted to analyze the fiber attenuation mechanism under cold air drawing, the mechanism is still not clear because of the limitations of the CFD model. Firstly, it is difficult to incorporate implicit flow and thermal boundary conditions in the CFD model, such as the air drag force and heat transfer on the moving interface between air and polymer which are both related to fiber diameter and air velocity. Secondly, it was observed experimentally that fiber solidification point varies with different processing conditions and material properties which means an iteration of different geometries is needed. Since each specific CFD model has to be based on a fixed geometry. It is not efficient to create these geometries and solve for each model, especially for geometry with high length to width aspect ratio which typically needs a tremendously large number of elements.

To address these limitations, we developed a 1-D non-isothermal Newtonian fluid model by solving three basic governing equations numerically using Matlab. The specific objectives of this theoretical modeling were to:

- Design and validate a computation method to solve the ordinary differential equations derived from basic fluid dynamics governing equations.

- Formulate a 1-D model for the fiber attenuation process under cold air drawing, and obtain reasonable values for input parameters, such as viscosity, air drag coefficient and heat transfer coefficient.
- Use the formulated model to analyze the fiber attenuation mechanism, mainly the effects of polymer viscosity, processing temperature, polymer and air volume flow rate on resulting fiber diameter.
- Use the model to predict the final fiber diameter and compare the predicted values with experimental results.

## **7.2. Literature Review**

As discussed in Chapters 1, the melt blowing process was developed based on the melt spinning process. In both processes, the polymer melt is extruded out of the extrusion orifice to form a filament, and it is immediately attenuated by external forces. In melt spinning, the external force is the drag force applied by a drawing roller. The air surrounding the fiber applies a retarding force on the fiber. In melt blowing, the external force is provided by a high speed air stream with air frictional force on the fiber surface. Numerical models for melt spinning with air flow as retarding force have been available for some decades. The models for melt blowing were mostly derived from the same governing equations by applying inverse air drag force and different boundary conditions. In this section, the background on modeling melt spinning is introduced first, and a comparison between melt spinning and melt blowing modeling is then presented.

The original studies on melt spinning modeling mainly focused on how the fiber is cooled along the spinline during the attenuation process. Andrews [97] set up groups of heat flow equations and solved them approximately with the aid of empirical data. With

this model, he predicted the temperature profile with the distance from the spinneret for both surface and centerline of the filament. The results were quite accurate, although the predicted radial temperature distribution was only correct to within 20%.

A seminal work in this filed was contributed by Kase and Matsuo [57, 58]. They developed fundamental equations on the dynamics of melt spinning. Then steady-state and transient solutions of these fundamental equations were derived and compared with experimental results. The fundamental equations used in their study are:

Equation of heat balance:

$$v \frac{\partial t}{\partial x} + \frac{\partial t}{\partial \tau} = - \frac{2\sqrt{\pi} h (t - t^*)}{\rho C_p \sqrt{A}} \quad (26)$$

Equation of force balance:

$$\frac{\partial v}{\partial x} = \frac{F}{\beta A} \quad (27)$$

Equation of material balance:

$$v \frac{\partial A}{\partial x} + \frac{\partial A}{\partial \tau} = -A \frac{\partial v}{\partial x} \quad (28)$$

In the above equations, ‘x’ is the distance from the spinneret and  $\tau$  is the time. Both of them are independent variables. Temperature ‘t’, cross-sectional area ‘A’ and local velocity ‘v’ are the dependent variables. In their calculations, the tensile viscosity ‘ $\beta$ ’ is assumed only to be a function of temperature t as well as the spinning tension F.

One important contribution of their work is the correction of heat transfer coefficient for melt spinning process. They experimentally measured the heat transfer coefficient by hanging a heated wire with diameter of 0.2 mm in an air flow. By recording and converting the cooling of the wire, the Nusselt number was fitted with Reynolds number

and was compared with other research results as shown in Figure 7.1. The data fitting turned out a relation of  $Nu=0.764Re^{0.38}$ .

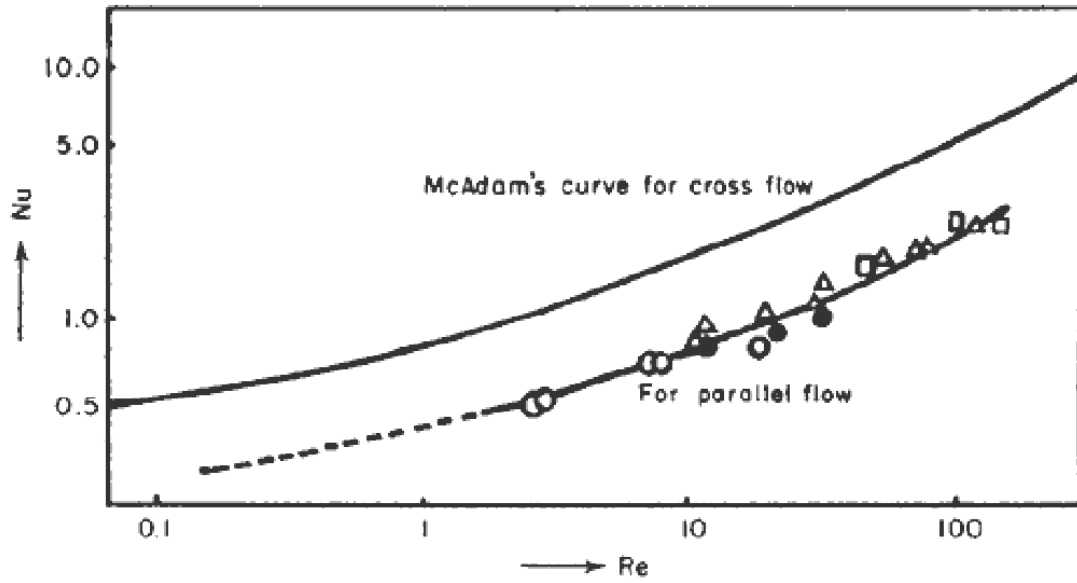


Figure 7.1 Nu vs. Re in cooling by forced convection of cylindrical body; (●) data of Simmons; (○) data of Mueller; (△) data of Sano and Nishikawa; (□) Kase and Matsuo's work [57].

However, it was realized by the authors that this calculation method can not exactly represent the real heat transfer phenomenon of melt spinning process because the wire was stationary. With further efforts, the authors derived a new Nu-Re relation  $Nu=0.42Re^{0.334}$  for parallel air flow of melt spinning with Reynolds number within the range of 0.5-50. Additionally, a corrective coefficient  $(1+K)$  was multiplied to the heat transfer coefficient for the contribution of a transverse air velocity correction. The heat transfer coefficient used in their model was constructed as:

$$h = 0.21k_F \sqrt{\frac{\pi}{A}} \left( \frac{2G}{\sqrt{\pi} A \rho v_F} \right)^{0.334} (1 + K) \quad (29)$$

where  $K_F$  is the heat conductivity of polymer;  $G$  is the polymer flow rate;  $\rho$  is the polymer density and  $\mu_F$  is the kinematic viscosity of ambient air.

Both steady-state and transient solutions were obtained by solving the listed partial differential equations with the corrected heat transfer coefficient. The results showed a good agreement with the measured experimental data of temperatures and fiber thickness along the spinline. Furthermore, the effects of material properties and processing conditions on final fiber thickness and temperature distributions were also studied. Finally, the steady-state solutions were related to the yarn properties. Specifically, the yarn density, birefringence, crystallinity and molecular orientation were predicted based on the filament temperature and cross-section area.

Spruiell et al. [98, 99] developed an ‘inverse model’ to calculate the heat transfer coefficient and elongational viscosity for high speed melt spinning of Nylon 6. In this inverse model, the fiber diameter, temperature profile and tension at the bottom of the spinline were experimentally measured and used to calculate the rheological force as a function of position along the spinline. The equation used for calculation is:

$$F_{rheo}(z) = F_L - \int_z^L \rho_{air} C_d V^2 \pi D dz - W[V(L) - V(z)] + \int_z^L \rho g \pi (D^2 / 4) dz \quad (30)$$

where  $W$  is mass throughput,  $V$  is fiber velocity,  $F_L$  is take-up force and  $C_d$  is air drag coefficient. Then a regression analysis was used to fit a smooth function for the fiber diameter and temperature profile. The continuity equation was used to calculate fiber velocity. Finally, the velocity and temperature gradients were obtained by differentiating the smoothed velocity and temperature profiles, and then they were used to calculate the elongational viscosity and heat transfer coefficient. The regression analysis confirmed that the heat transfer coefficient involved in this melt spinning process is not a material

property. By fitting the calculated heat transfer data versus the ratio of fiber velocity over cross-section area, an empirical equation for heat transfer coefficient was given by:

$$h = 1.43 \times 10^{-4} (V / A)^{0.256} \quad (31)$$

The air drag coefficient is an important coefficient for describing the air drag force applied on the filament during melt spinning and melt blowing. Matsui [100] developed a relationship between the air drag coefficient  $C_f$  and the Reynolds number  $Re_D$  based on the turbulent boundary layer theory.

$$C_f = \beta Re_D^{-n} \quad (32)$$

$$Re_D = \frac{\rho_a U D}{\mu_a} \quad (33)$$

where  $\beta$  and  $n$  are constant coefficient,  $\rho_a$  is the air density,  $\mu_a$  is the air viscosity,  $U$  the velocity of the filaments, and  $D$  the diameter of filament. With  $\beta=0.37$  and  $n=0.61$ , a satisfactory agreement between theoretical analysis and this empirical relation was observed for spinning speed in the range of 300-6000 m/min in melt spinning. Shambaugh and Majumdar [44] designed an instrument to experimentally measure the air drag force under a wide range of conditions. The filament diameter varied from 13 to 305  $\mu\text{m}$  and the air velocity changed from 36 to 300 m/s. The experimental results were found to fit well with an empirical relation:

$$C_f = 0.78 Re_D^{-0.61} \quad (34)$$

In this study, they also summarized representative values of  $\beta$  that were determined by various investigators listed in Table 7-1.

Based on Kase and Matsuo's effort, more recent studies on modeling of melt spinning expanded the 1-D model to 2-D models. These 2-D models also included the

combined effects of flow induced crystallization, molecular orientation, non-isothermal viscoelasticity, and air drag.

Differential constitutive models were widely used to analyze the melt spinning process, such as upper-convected Maxwell (UCM) model, Phan-Thien/Tanner (PTT) model and Kaye/Bernstein-Kearsley-Zapas (K-BKZ) model. For example, Mitsoulis and Beaulne [101] studied the rheological effects in fiber spinning using numerical simulation with K-BKZ model. The non-isothermal unidirectional model was constructed by the following mass, momentum and energy equations respectively:

$$\rho(\pi r^2)u = \rho Q \quad (35)$$

$$\frac{d}{dz} \left( \frac{\tau_{zz} - \tau_{rr}}{\rho u} \right) - \frac{du}{dz} + \frac{g}{u} - C_f u \left( \frac{\rho_a}{\rho} \right) \sqrt{\frac{\pi u}{Q}} = 0 \quad (36)$$

$$\rho C_p Q \frac{dT}{dz} + 2\pi \sqrt{\frac{Q}{\pi u}} h_c (T - T_\infty) + 2\pi \sqrt{\frac{Q}{\pi u}} \sigma_{SB} \mathcal{E} (T^4 - T_\infty^4) = 0 \quad (37)$$

with boundary conditions:

$$\begin{aligned} 1. \quad & u = u_0 \quad \text{at} \quad z = 0 \\ 2. \quad & T = T_0 \quad \text{at} \quad z = 0 \\ 3. \quad & u = u_L \quad \text{at} \quad z = L \end{aligned} \quad (38)$$

Table 7-1 Value of  $\beta$  and  $n$  from literature [44].

Case	$\beta$	$n$	Maximum $V_{rel}$ (m/min)	Fiber diameter ( $\mu\text{m}$ )	$Re_D$	Comments
1	0.37	0.61	6000	29-86	10-330	Single filament melt spinning into stagnant air
2	0.41	0.61	6000	17-300	20-200	Single and multiple stationary filament inside a tube; tensioned and untensioned
3	0.90	0.61	1060	26-45	10-60	Single stationary filament in a tube; untensioned
4	1.3	0.61	...	50-400	25-310	Single stationary filament in a tube; filament not tensioned
5	0.49	0.61	6000	19-93	40-250	Single filament melt spinning with no guide at take up roll
6	0.39	0.61	1000	38-60	25-50	Single filament melt spinning with guide at take up roll
7	0.23	0.61	6000	10-23	5-60	Simultaneous melt spinning of 16 filaments
8	0.77	0.61	...	45-74	50-400	Single stationary filament in wind tunnel or single melt spun filament in wind tunnel
9	0.91	0.61	6480	80-222	280-1530	Drag exerted by aspirator jet on a filament
10	0.78	0.61	18000	13-305	15-3000	Drag exerted upon filament by a free annular jet



where  $\rho$  is the density,  $u$  is the fiber velocity,  $Q$  is polymer volume flow rate,  $\tau$  represents extra stresses,  $g$  is the acceleration of gravity,  $C_f$  is the air drag force coefficient,  $C_p$  is the specific heat capacity,  $h_c$  is the heat transfer coefficient,  $T$  is the filament temperature,  $T_\infty$  is the ambient air temperature,  $\varepsilon$  is the emissivity,  $\sigma_{SB}$  is the Stefan-Boltzmann constant, and  $L$  is the spinline length.

Both isothermal and non-isothermal cases were simulated in this study. In the non-isothermal case of PET study, the results showed that PTT and K-BKZ have similar predictive capabilities. It was also concluded that the inertia, gravity, and air drag are important in the simulation. In the case of LDPE study, die swell was found to be very important for predicting the take-up force.

Usually, the 1-D model is sufficient to simulate the melt spinning process because the fiber diameter is relatively small compared with the spinline length. In 1-D simulation, the filament temperature is only a function of axial distance from spinneret which means there is no temperature variance in the radial direction. Henson et al. [102] indicated that neglecting the radial temperature variation led to an overestimate of the forced heat convection on the filament surface. This overestimation on heat transfer can cause inaccuracy of the fiber velocity and finally influence the simulation results. Additionally, the radial temperature variation also yielded radially non-uniform tensile stress, which results in non-uniform molecular orientation and crystallinity.

Sun et al. [103] confirmed Henson's finding by simulating a 2-D non-isothermal melt spinning case with ongoing crystallization using the commercial software Polyflow. The constitutive equation used in this simulation was the PTT model, which was converted from its isothermal form with a time-temperature superposition algorithm. The simulation

results showed that the non-uniform thermal history gave rise to a strong radial variation of viscoelastic stress which finally led to a strong effect on the resulting fiber properties, such as crystallinity and molecular orientation.

Doufas et al. [61-63, 104] also successfully used a 2-D model to simulate melt spinning including flow-induced crystallization for many polymers, such as PET, PLLA, and rPLA. Their results showed good agreement between simulated results and experimental spinline data for the relation between processing conditions and fiber microstructure.

Unlike melt spinning, melt blowing is quite difficult to simulate since its lower boundary is a moving boundary and needs to be determined during the simulation. Extensive modeling studies were conducted by Shambaugh and his group [45, 70, 71]. Their first attempt [70] was to develop a 1-D model based on the following continuity, momentum and energy equations:

Continuity

$$A_z v_{fz} = Q = \text{constant} \quad (39)$$

where  $A_z$  is fiber cross-section area,  $V_{fz}$  is fiber velocity and  $Q$  is polymer volume flow rate.

Momentum

$$\frac{d}{dz} \left[ \pi \frac{d_z^2}{4} (\tau^{zz} - \tau^{rr}) \right] = j \pi d_z C_f \rho_a \frac{V_{rel}^2}{2} + \rho_f Q \frac{dv_{fz}}{dz} - \frac{\pi d_z^2}{4} \rho_f g \quad (40)$$

where  $z$  is axial position,  $\tau$  are extra stresses,  $C_f$  is air drag coefficient,  $\rho_a$  is air density,  $v_{rel}$  is difference in velocity between the filament and air,  $\rho_f$  is polymer density,  $d_z$  is fiber diameter and  $g$  is gravitational acceleration.

Energy

$$\rho_f C_{pf} v_{fz} \frac{dT_{fz}}{dz} = -\frac{4h_z}{d_z} (T_{fz} - T_{az}) \quad (41)$$

where  $h_z$  is convective heat transfer coefficient,  $T_{fz}$  is filament temperature,  $T_{az}$  is air temperature and  $C_{pf}$  is heat capacity of the fiber.

These governing equations are almost the same as those used in melt spinning simulation. The only difference is the air drag force in the momentum equation, which plays a dominant role on fiber attenuation in melt blowing process. For the boundary conditions, the upper boundary is identical to that of melt spinning, where a constant known value of fiber velocity and temperature are imposed. A “freeze point” method was used in their study to define the lower boundary condition. The position of fiber freeze was specified at  $z=5$  cm where the attenuation of fiber becomes negligible. It was claimed that the selection of  $z=5$  cm gives good fit to the data and a better converged solution. Compared with the experiments data, this model provided an excellent prediction of fiber diameter profile in the region of high fiber attenuation and slight under prediction on final fiber diameter. The Phan-Thien/Tanner viscoelastic model was also applied in this model to compare with the Newtonian fluid model, but only little difference was found between these two constitutive models.

It was pointed out by Shambaugh et al that the high prediction of final fiber diameter in the 1-D model results from the fiber vibration at the distance far away from spinneret. To consider this vibration effect, a 2-D model was developed by Rao and Shambaugh [71]. The previous ‘freeze point’ method cannot be applied to the lower boundary condition since this 2-D model included fiber vibration. Therefore, a new method called ‘stop point’ was assumed. At this ‘stop point’, the fiber velocity is equal to the air

velocity. The predictions based on these two different methods were virtually identical and thus proved the accuracy of the ‘stop point’ method. By comparing with their previous 1-D model results, the new 2-D model actually made little differences in diameter or temperature predictions. The reason of over prediction of fiber final diameter was attributed to the under predicted fiber vibration amplitudes. However, this model provided a method to estimate the experimental conditions that can cause the fiber breakage.

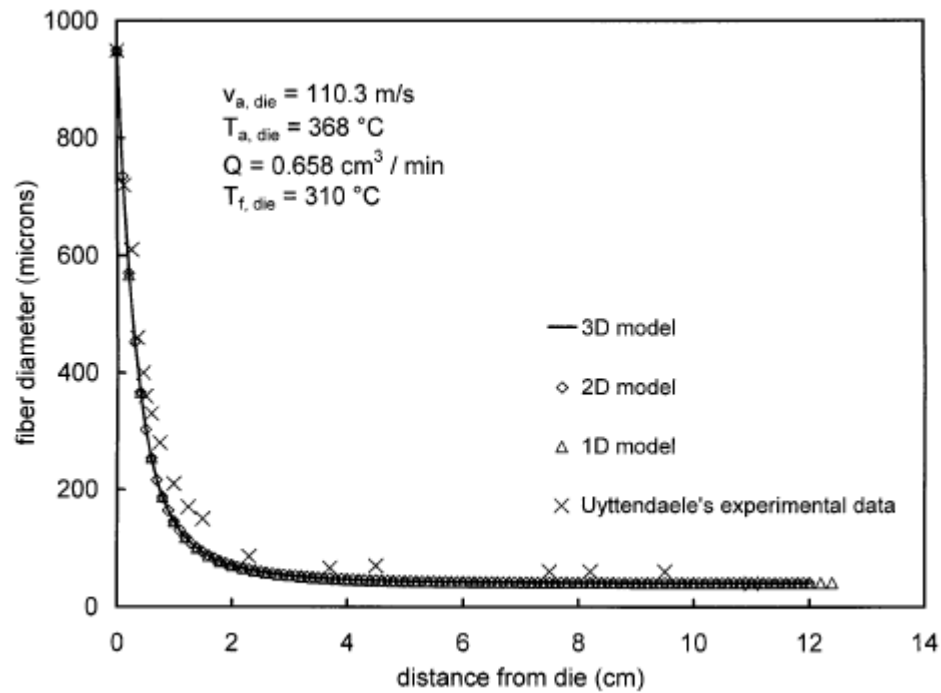


Figure 7.2 Comparison of the predictions of the 3D model with those of the 2D and 1D models [45].

This 2-D model was then expanded to a 3-D model to predict the 3-D motion of a fiber in the melt blowing process. However, the 3-D model still gave similar predictions results as compared with the previous 1-D and 2-D models as shown in Figure 7.2. The turbulence effects was concluded as a possible reason for the under predicted fiber

vibration amplitude. Both Newtonian and Phan-Thien/Tanner models were used in this study, and the predictions of fiber diameter and temperature showed similar results.

In conclusion, the model used in melt spinning can be applied to the simulation of melt blowing process with two modifications:

1. Change the retarding air drag force into forward direction;
2. Use a moving boundary condition for the lower boundary, either ‘stop point’ method or ‘freeze point’ method.

Based on the literature, 1-D model is satisfactory to simulate the melt blowing process. 2-D and 3-D models do not give better predictions on the fiber diameter and temperature profile although they dramatically increase the computation time. For polypropylene, the Newtonian constitutive model can provide similar predictions as that using the Phan-Thien and Tanner model.

### **7.3. Model Formulation**

#### **7.3.1. Model Description**

In this study, a 1-D non-isothermal Newtonian fluid model was chosen to simulate the melt spinning process under cold air attenuation. Figure 7.3 describes the process and forces acting on the single filament. The air drag force applied on the fiber surface is in the same direction as the gravity force. These two forces are counterbalanced by the rheological force and inertia force. Since cold air was used in this process, forced convection heat transfer occurs on the interface between polymer melt and cold air.

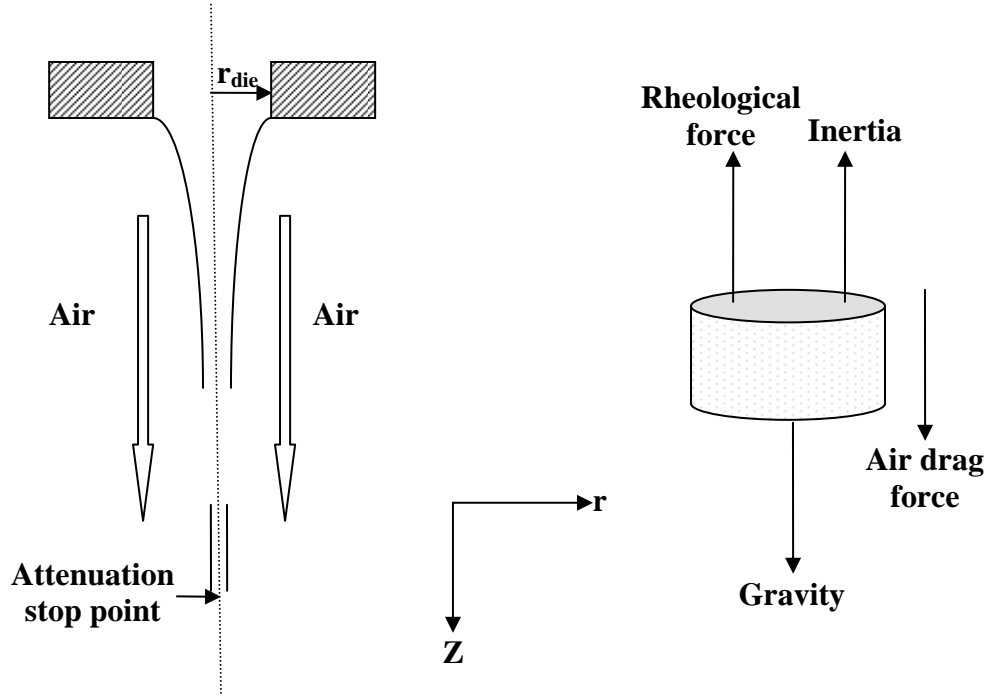


Figure 7.3 Schematic of the melt spinning process by cold air attenuation and the force balance on fibers.

### 7.3.2. Governing Equations

The continuous filament obeys mass conservation at any position beneath the spinneret orifice. The density of polymer only changes about 10% between the melt and the solid state. Only considering a constant polymer density, the mass conservation can be simplified to volume conservation which means the polymer volume flow rate remain constant anywhere.

$$\rho_f \pi r^2 V_f = \rho_f Q \quad (42)$$

where  $\rho_f$  is the polymer density,  $r$  is the fiber radius,  $V_f$  is the fiber velocity and  $Q$  is the polymer volume flow rate.

The differential form of the momentum equation can be formulated based on the force balance:

$$\frac{d}{dz} \left[ \pi r^2 (\tau_{zz} - \tau_{rr}) \right] + \pi (2r) C_f \rho_a \frac{(V_a - V_f)^2}{2} - \rho_f Q \frac{dV_f}{dz} + \pi r^2 \rho_f g = 0 \quad (43)$$

where  $\tau_{zz}$  and  $\tau_{rr}$  are the extra stresses in z and r direction,  $C_f$  is the air drag coefficient,  $\rho_a$  is the air density,  $V_a$  is the air velocity, and  $g$  is the gravitational acceleration.

The air drag coefficient,  $C_f$ , is defined by Matsui [100]:

$$C_f = \beta \text{Re}_D^{-n} \quad (44)$$

where  $\text{Re}_D$ , the Reynolds number, is defined by:

$$\text{Re}_D = \frac{\rho_a V_a (2r)}{\mu_a} \quad (45)$$

where  $\beta$  and  $n$  are constant coefficient,  $\rho_a$  is the air density, and  $\mu_a$  is the air viscosity.  $\beta=0.78$  and  $n=0.61$  are appropriate value for melt blowing based on Shambaugh and Majumdar's study [44]. These parameters are also applicable in our process since air dynamics environment is similar.

A simplified steady state energy equation was used in this study:

$$\rho_f C_{pf} V_f \frac{dT_f}{dz} = -\frac{4h_c}{2r} (T_f - T_a) \quad (46)$$

where  $C_{pf}$  is the polymer heat capacity,  $T_f$  is the fiber temperature,  $T_a$  is the air temperature and  $h_c$  is the convective heat transfer coefficient. Because the forced convective heat transfer is dominant, the heat transfer effects resulted from conduction, radiation, viscous heating are neglected.

The heat transfer coefficient,  $h_c$ , can be determined with the following correlation:

$$\text{Nu} = \gamma \text{Re}_D^m \quad (47)$$

where  $\text{Nu}$ , the Nusselt number is defined as:

$$Nu = \frac{h_c(2r)}{k_a} \quad (48)$$

where  $k_a$  is the thermal conductivity of air, and the Reynolds number has the same definition as that in Equation (45).  $\gamma$  and  $m$  are constants which are equal to 0.764 and 0.38 respectively according to Matsuo and Kase's study [57].

### 7.3.3. Constitutive Equations

For a Newtonian fluid, the stress tensor  $\tau_{zz}$  and  $\tau_{rr}$  are defined as:

$$\tau_{zz} = 2\eta \frac{dV_f}{dz} \quad (49)$$

$$\tau_{rr} = -\eta \frac{dV_f}{dz} \quad (50)$$

where  $\eta$  is the zero shear rate viscosity of the polymer. As a non-isothermal model, the temperature dependence of viscosity is considered using the Arrhenius law by the following equation:

For PP115

$$\eta = 0.002087 \exp\left(\frac{5530}{T_f}\right) \quad (51)$$

For PP12

$$\eta = 0.002946 \exp\left(\frac{6347}{T_f}\right) \quad (52)$$

where  $T_f$  is the filament temperature in Kelvin.

### 7.3.4. Boundary Conditions

Two boundary conditions can be specified for this model. The upper boundary located just beneath the die orifice can be defined as:



$$\begin{aligned} V_f &= V_{f0} & \text{at} & \quad z = 0 \\ T_f &= T_{f0} & \text{at} & \quad z = 0 \end{aligned} \quad (53)$$

The lower boundary is located at where the fiber solidifies and the fiber attenuation stops. Unlike the traditional melt spinning whose lower boundary condition is fixed by take-up speed, the low boundary presented in this model is a moving boundary and need to be determined during the calculation. Two conditions based on temperature and velocity are used to define the lower boundary:

$$\begin{aligned} \frac{dV_f}{dz} &= 0 & \text{at} & \quad z = L \\ T_f &= T_s & \text{at} & \quad z = L \end{aligned} \quad (54)$$

where L is an unknown variable defining the position where the fiber solidifies,  $T_s$  is the fiber solidification temperature which is equal to 135°C for polypropylene in this study as discussed in the previous part. This lower boundary condition is appropriate to describe the fiber solidification phenomenon since it determines the solidification point based on two variables, the temperature and velocity gradient.

#### 7.4. Method of Solution

The governing equations with the substitutions described were solved numerically using MATLAB by finite element method. The detail calculation procedures are:

1. In momentum equation (43), substitute the air drag coefficient with equation (44), the extra stresses with equations (49) and (50).
2. In energy equation (46), substitute the heat transfer coefficient with equation (48).
3. Simplify the substituted momentum and energy equations with mass conservation equation (42), replacing the variable  $r$  with function of  $V_f$  by equation:

$$r = \sqrt{\frac{Q}{\pi V_f}} \quad (55)$$

Then the momentum and energy equations can be simplified in the forms of:

$$\frac{d^2 V_f}{dz^2} = f_1(V_f) \left( \frac{dV_f}{dz} \right)^2 + f_1(T_f, V_f) \left( \frac{dV_f}{dz} \right) + f_2(T_f, V_f) \quad (56)$$

$$\frac{dT_f}{dz} = f_2(V_f)(T_f - T_a) \quad (57)$$

where  $f(V_f)$  are functions of variable  $V_f$  and other constant variables,  $f(T, V_f)$  are functions of variables  $T, V_f$  and other constant variables.

4. Equation (56) is a second order ordinary differential equation. Since it is a one-dimensional model,  $V_f$  and  $T_f$  are only the functions of spinline position  $z$ . Taking:

$$\begin{aligned} y_1(z) &= y(z) = V_f \\ y_2(z) &= y'(z) = \frac{dV_f}{dz} \\ y_3(z) &= T_f \end{aligned} \quad (58)$$

The second order ordinary differential equation can be downgrade to first order. The new momentum and energy equations will form a system of three first order differential equations which are solvable in MATLAB with its built-in boundary value problems solver.

$$\begin{aligned} y_1'(z) &= y_2(z) \\ y_2'(z) &= f_1(y_1(z)) y_2^2(z) + f_1(y_1(z), y_3(z)) y_2(z) + f_2(y_1(z), y_3(z)) \\ y_3'(z) &= f_2(y_1(z))(y_3(z) - T_a) \end{aligned} \quad (59)$$

5. Two separate iteration schemes were applied during the calculation. The first one is based on the fiber velocity. The iteration will converge on a result that satisfies the initial fiber velocity at upper boundary and velocity gradient at lower

boundary. In second iteration, the fiber length will be increased step by step. At each step, the fiber temperature at lower boundary will be compared with fiber solidification temperature 135°C. The iteration will stop if the fiber temperature is lower or equal to 135°C. Otherwise, the fiber length will be increased for next iteration until the fiber temperature reaches that solidification temperature.

### 7.5. Validation of Computation Method

The MATLAB built-in solver ‘bvp4c’ was used to solve the system of three first order ordinary differential equations. This computation method was validated using commercial CFD software Polyflow. A simple model was created which can be simulated by both methods. In this model, the fiber freely falls down after extruded out of the die orifice. The only external force acting on the fiber is the gravity force which is the driven force for fiber attenuation. An isothermal incompressible Newtonian fluid was considered to simplify this validation process.

The governing equations were formulated as follows for the calculation in MATLAB:

Mass conservation

$$\rho_f Q = \rho_f \pi r^2 V_f \quad (60)$$

Momentum conservation

$$\frac{d}{dz} [\pi r^2 (\tau_{zz} - \tau_{rr})] = \rho_f Q \frac{dV_f}{dz} - \pi r^2 \rho_f g \quad (61)$$

Where the extra stresses is defined as:

$$\tau_{zz} = 2\eta \frac{dV_f}{dz} \quad (62)$$

$$\tau_{rr} = -\eta \frac{dV_f}{dz} \quad (63)$$

A fixed fiber length was used for each validation case. The upper boundary at the die orifice is  $V_f=0.003$  m/s for the initial fiber velocity. The lower boundary at bottom geometry is  $dV_f/dz=0$  which means the stop of fiber attenuation.

In Polyflow, a rectangular geometry was created and imported as shown in Figure 7.4. An isothermal Newtonian fluid model was chosen and polymer density and viscosity are assumed constant. The width of the geometry was calculated according to the mass conservation equation using the same volume flow rate as that in MATLAB calculation. Four different geometry lengths were generated for the validation, 3 cm, 4 cm, 5 cm and 10 cm.

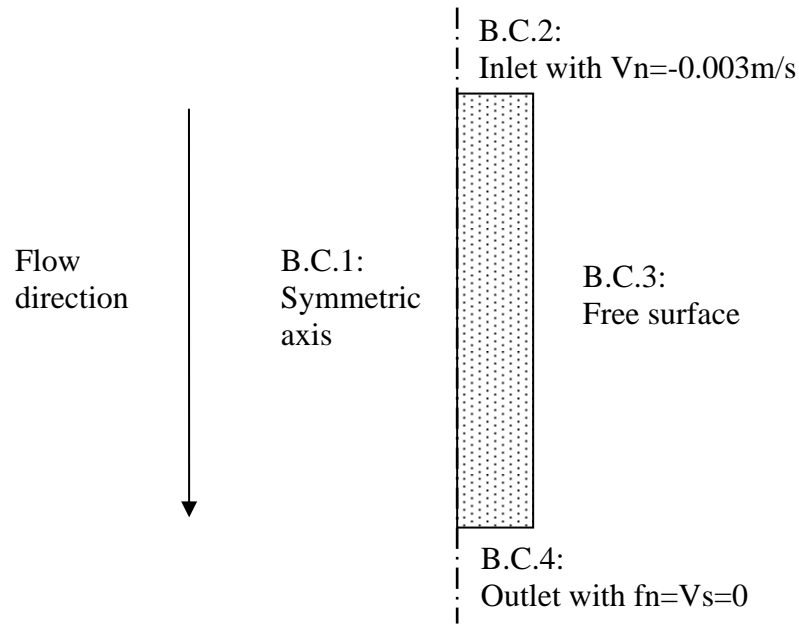


Figure 7.4 Model description of geometry and boundary conditions of freely fall down fiber in Polyflow.

The simulation results obtained from Polyflow are shown in Figure 7.5. The fiber geometry was rescaled to get the full view. Under the same external force, gravity, the fiber velocity increases with the increasing of origin geometry length. In other word, the

longer initial geometry length will lead to higher fiber acceleration and finally results in a finer fiber. When the initial geometry length increases from 3 cm to 4 cm, 5 cm and 10 cm, the final fiber velocity increases from 0.0065 m/s to 0.0087 m/s, 0.0114 m/s and 0.0310 m/s respectively.

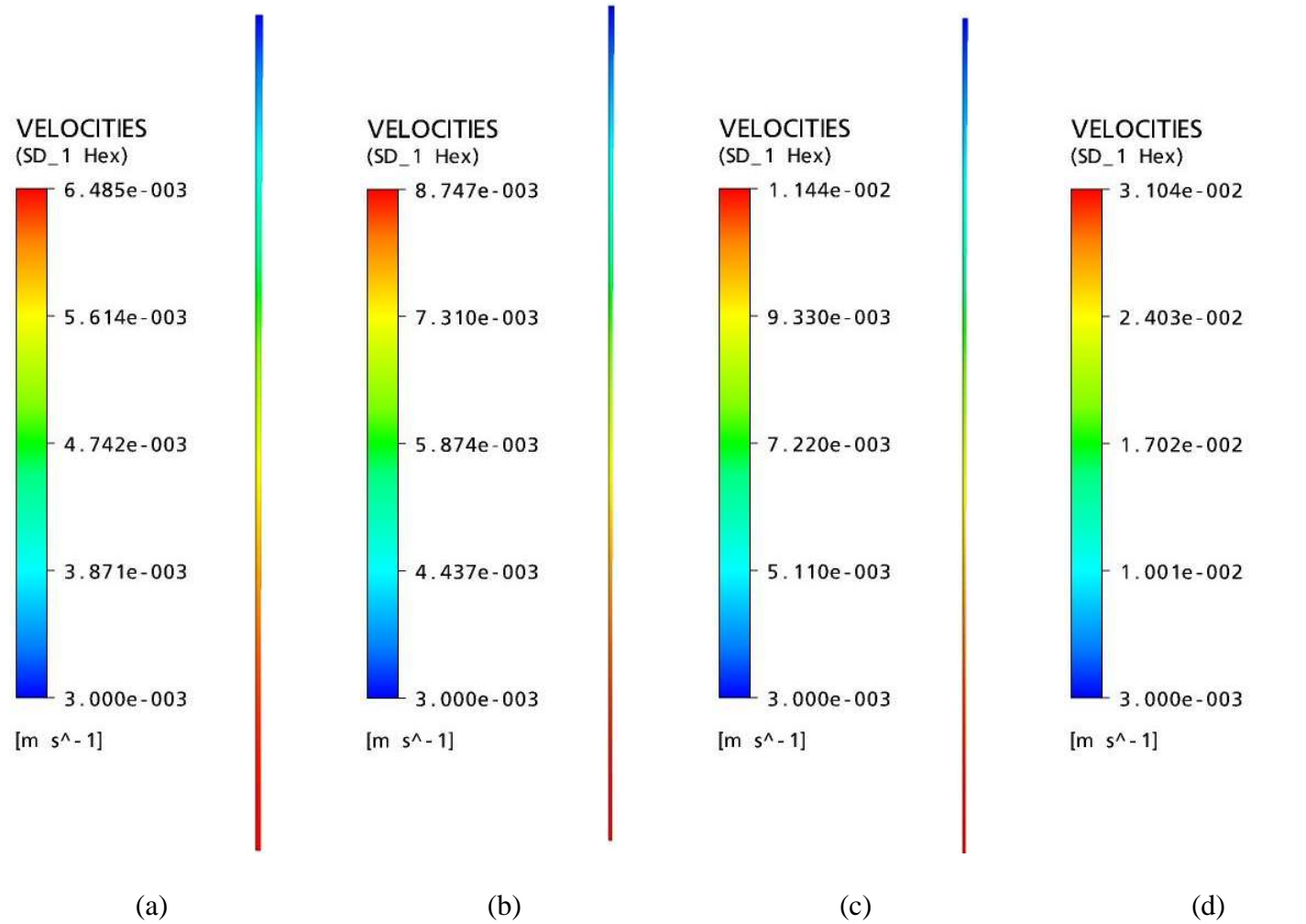


Figure 7.5 Polyflow simulation results for freely fall down fiber model with different model geometry in length, (a) 3 cm, (b) 4 cm, (c) 5 cm and (d) 10 cm.

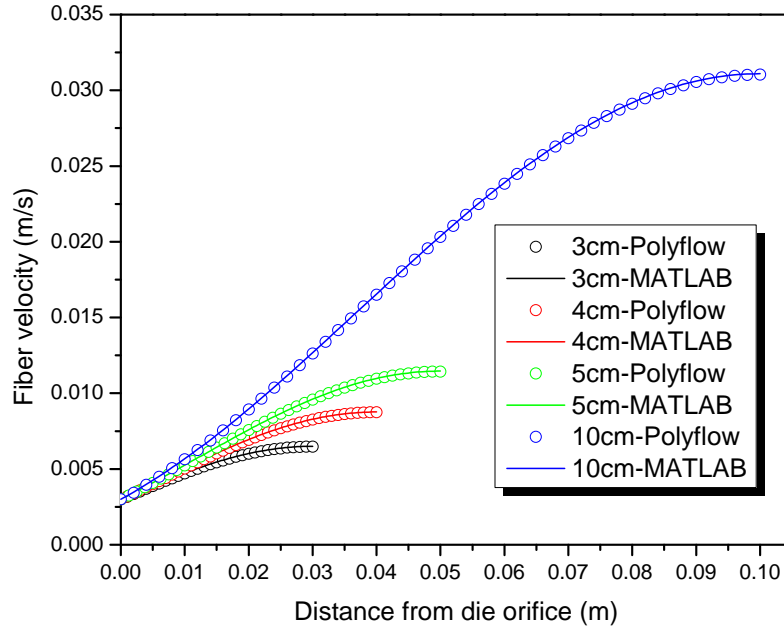


Figure 7.6 Comparison between the results obtained by Polyflow and MATLAB for different initial geometry length, 3 cm, 4 cm, 5 cm and 10 cm.

The simulation results obtained from MATLAB are presented in Figure 7.6 and are compared with the results from Polyflow. In the figure, the circles represent the Polyflow results and the lines represent the MATLAB results. The two results are essentially identical which means the computational methods used in MATLAB are as accurate as that in Polyflow for the test cases. This validation procedure confirms that the calculations based on the model implemented in MATLAB are free from computational errors.

## 7.6. Isothermal Model

Although the objective of this theoretical modeling is to build a non-isothermal model, it is desirable to develop an the isothermal model first for the following two reasons:

Firstly, the isothermal model provides a better understanding of the effect of processing conditions. With a non-isothermal model, the effects of processing conditions are coupled. For example, the air flow velocity influences both heat transfer coefficient and air drag coefficient. When the air flow velocity increases, the heat transfer coefficient increases and makes the fiber cooled faster which prevents fiber attenuation, whereas the air drag force increases with the increase of air flow velocity thus promoting fiber attenuation.

Secondly, it is easier to study the effect of the attenuation stop position in the isothermal model. Usually,  $dV_f/dz=0$  is defined as one of the boundary conditions at the attenuation stop point. The second condition on this boundary is to define the position where the attenuation stops. It is expected that different stop positions will generate different fiber velocity profiles and thus affect the whole simulation results. Excluding the effects from energy equation will make it easier to analyze this mechanism.

The material properties and processing conditions used in the isothermal model are listed in Table 7-2 except for some specialized individual case. A position with a distance of 5cm from the orifice was chosen initially as the model geometry length.

Table 7-2 Material properties and processing conditions for the isothermal model with

5cm model geometry length.

	Density ( <b>Kg/m<sup>3</sup></b> )	Viscosity ( <b>Pa·s</b> )	Velocity ( <b>m/s</b> )
<b>Polymer</b>	900	100	0.01
<b>Air</b>	1.2	0.00002	100



### **7.6.1. Effect of Model Geometry Length**

As discussed earlier, the simulation results showed that the fiber velocity depends on the model geometry length. Therefore, we first studied the effect of model geometry length on the fiber final diameter. Six different model geometry lengths with range from 1cm to 6cm were simulated and the results were compared in Figure 7.7. The fibers were attenuated to smaller diameters with increase of model geometry length. Within a very short distance from the die orifice, all six cases follow the same trend of fiber diameter versus distance. Then some curves start to split out in sequence with the increase of model geometry length which means that the fiber velocity profile also changes with the variation of model geometry length. This is because the longer model geometry length causes more acceleration in fiber velocity before it reaches the lower boundary. It was observed that the differences between fiber diameters are not significant when the model geometry length goes beyond 3cm which means a converged simulation result. Further investigation indicated that this critical model geometry length varies with material properties and processing conditions.

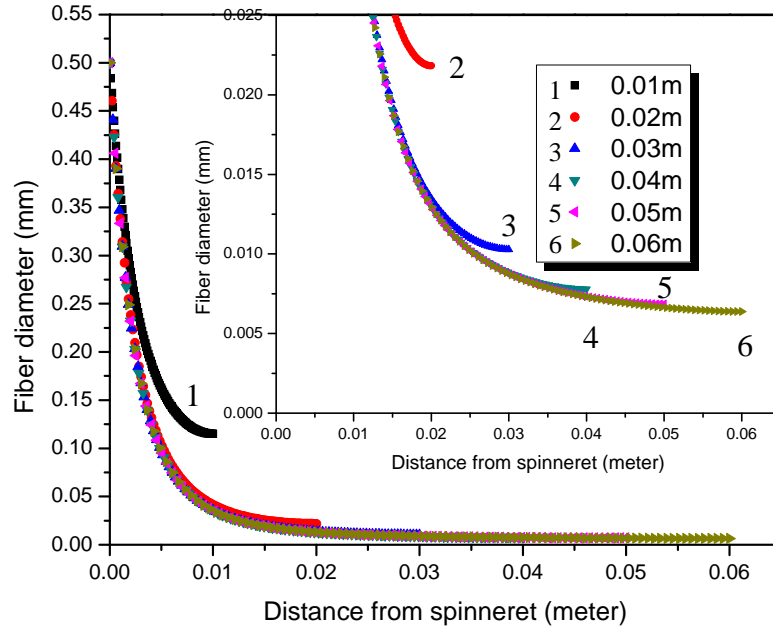


Figure 7.7 Isothermal model: fiber diameter profiles with different stop point positions  
(Inset: magnified view).

There is another important observation based on the results from Figure 7.7. Most of the fiber attenuation occurs within about 1 to 2 cm distance from the spinneret orifice in the simulations of different model geometry lengths. For example, in the case of model geometry length of 6 cm, the fiber diameter decreased to about 25  $\mu\text{m}$  after 1cm and reached about 10  $\mu\text{m}$  after 2 cm. After 3cm, the attenuation became insignificant and a flattened region appeared. Within this plateau region, the fiber diameter only changed from about 7 to 6  $\mu\text{m}$ . The plateau regions were also observed in the other cases with different model geometry lengths. The starting position of the plateau region varied with different value of model geometry length.

### 7.6.2. Effect of Polymer Viscosity

As shown in Figure 7.9, the fiber diameter was found to increase with the increase of polymer viscosity because higher viscosity means higher rheological force. As it counterbalances the air drag force, its high value makes fiber hard to be attenuated. It was found that the fiber diameter is not sensitive to polymer viscosity under simulated isothermal conditions. When polymer viscosity increased from 50 to 500 Pa·s, the final fiber diameter only increased from about 7 to 17  $\mu\text{m}$ . This is because a very high air flow velocity was used in this simulation. The high air velocity leads to high air drag force which is dominant over the rheological force. This agrees with the results shown in Figure 7.9. When the air velocity decreased to 20 m/s, a more significant difference of fiber diameter was revealed.

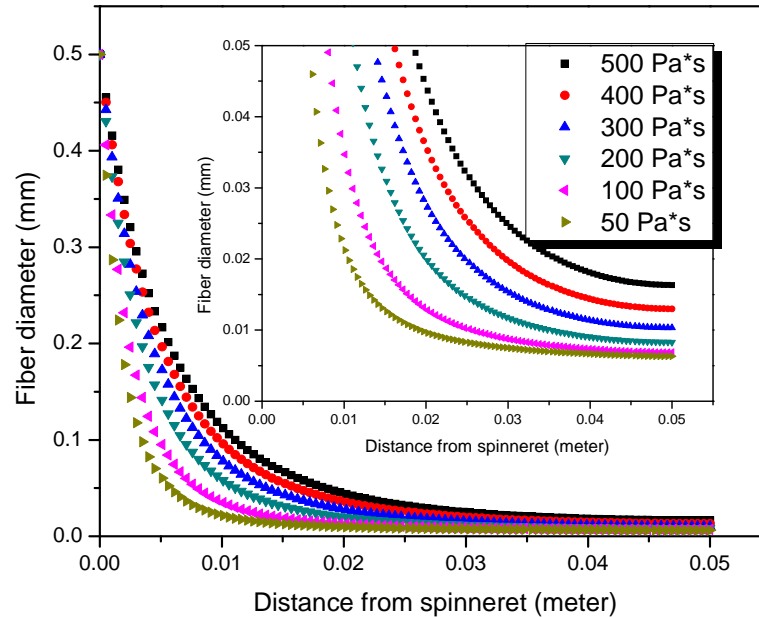


Figure 7.8 Isothermal model: fiber diameter profiles with different polymer viscosity with air flow velocity at 100 m/s (Inset: magnified view).

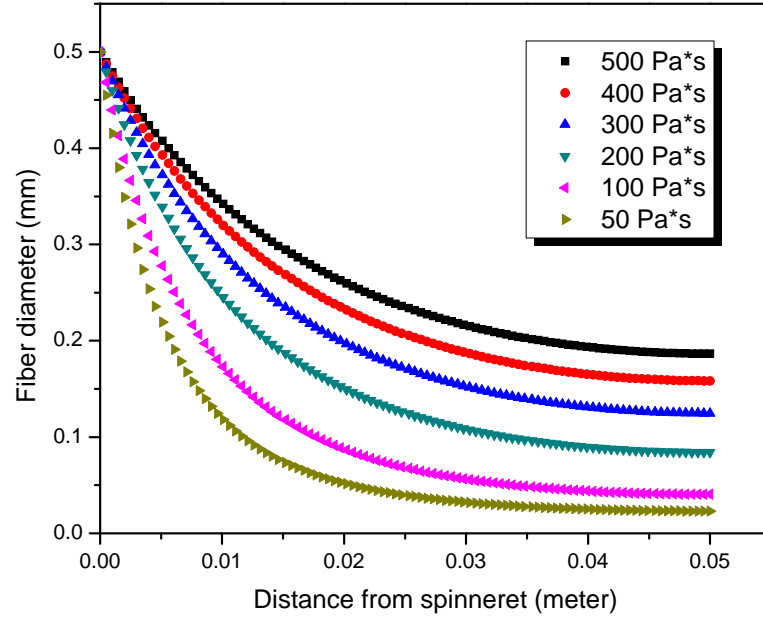


Figure 7.9 Isothermal model: fiber diameter profiles with different polymer viscosity with air flow velocity at 20 m/s.

### 7.6.3. Effect of Initial Fiber Velocity

As shown in Figure 7.10, the fiber diameter increases with the increase of initial fiber velocity. The fiber diameter is determined by the equation:

$$D = D_0 \sqrt{\frac{V_{f0}}{V_f}} \quad (64)$$

where the  $D_0$  is the original die orifice diameter which remains constant in our study. Therefore, the fiber diameter is dependent on the velocity ratio  $V_{f0}/V_f$ . Figure 7.11 indicates that the fiber velocity increases with the decrease of initial fiber velocity. As a result, the low initial fiber velocity makes the velocity ratio even smaller and results in a smaller fiber diameter.

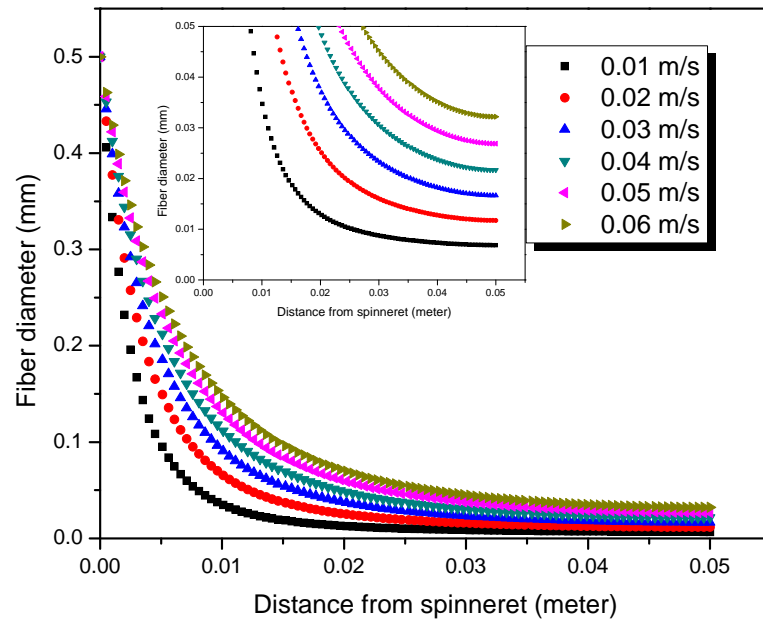


Figure 7.10 Isothermal model: fiber diameter profiles with different initial fiber velocity  
(Inset: magnified view).

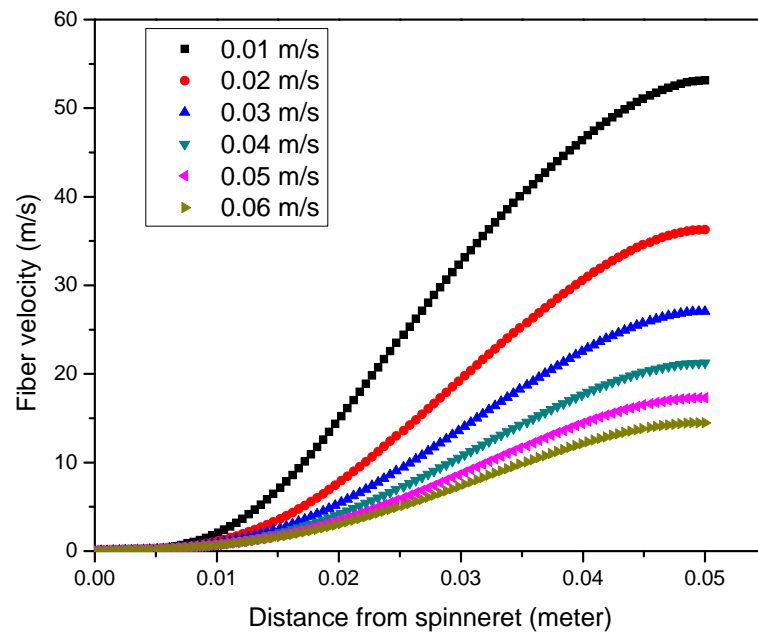


Figure 7.11 Isothermal model: fiber velocity profiles with different initial fiber velocity.

#### 7.6.4. Effect of Air Flow Velocity

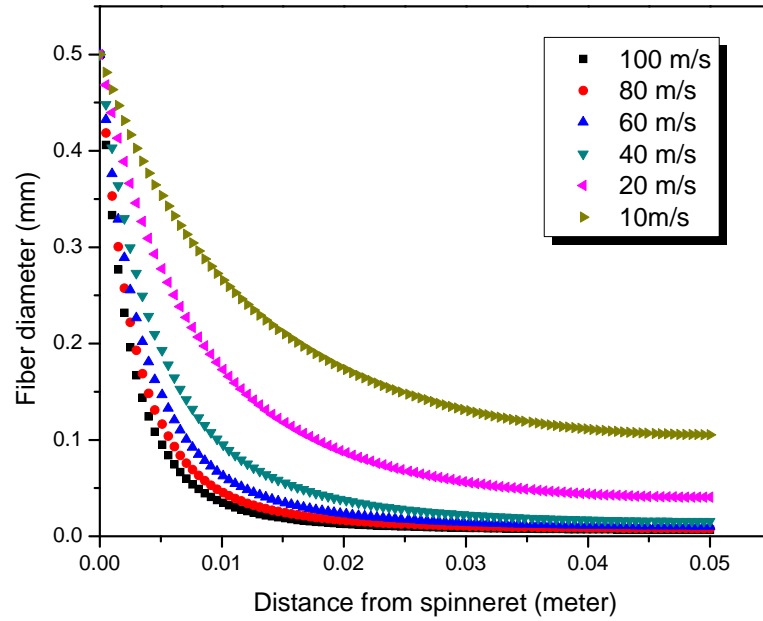


Figure 7.12 Isothermal model: fiber diameter profiles with different air flow velocity.

The fiber diameter also decreases with the increase of air flow velocity as presented in Figure 7.12. This is because the higher air flow velocity provides higher air drag force which causes more attenuation on fiber. The final fiber diameter did not show a linear variation with change of air flow velocity. At low velocity range, from 10 to 40 m/s, large variation in final fiber diameter was observed. When the air velocity increases from 60 to 100 m/s, only slight change in final fiber diameter was observed.

### 7.7. Non-isothermal Model

Although the isothermal model provides some understanding of the fiber attenuation mechanism under cold air drag, it is not sufficient to predict the entire process since the heat transfer plays an important role on fiber attenuation. Based on the isothermal model, three modifications were made to develop the non-isothermal model:

1. Introduce the polymer viscosity dependence of temperature by the Arrhenius law.
2. Introduce the energy equation by considering the convection heat transfer.
3. Determine the fiber solidification point by comparing the fiber temperature with polymer solidification temperature.

### 7.7.1. Modification of Calculation Method

The iteration method described previously was used to simulate one case of the non-isothermal model of fiber attenuation. The material properties and processing conditions are listed in Table 7-3.

Table 7-3 Material properties and processing conditions for non-isothermal case.

	<b>Density (Kg/m<sup>3</sup>)</b>	<b>Viscosity (Pa·s)</b>	<b>Thermal conductivity (W/K·m)</b>	<b>Heat capacity (J/K·kg)</b>	<b>Initial temperature (K)</b>	<b>Initial velocity (m/s)</b>
<b>Polymer</b>	900	$0.002087e^{5530/T}$	0.12	2000	513	0.005
<b>Air</b>	1.2	0.00002	0.027	1000	300	22

\*T is the polymer temperature

Figure 7.13 shows the simulation results of fiber diameter and temperature profile along the spinline. It was found that the fiber stops attenuation at a distance of 4 mm from the spinneret orifice and the final fiber diameter is just 0.473 mm which is far bigger than the experiment result, 8μm. This discrepancy must be caused by calculation mistake or improper calculation method. As discussed in section 7.6.1, the model geometry length has a significant influence on the fiber velocity profile. In this calculation, the model geometry length was initiated at 1mm and then increased gradually with a step size of 1mm. Therefore, the large simulated final fiber diameter is caused by the short model

geometry length. In the simulation, the fiber velocity gradient initially increases to some maximum value and then decreases to converge to the lower boundary condition ( $dV_f/dz=0$ ). When a short model geometry length is used, the velocity gradient can only reach a very small maximum value and then has to start to decrease to the value 0. On the other hand, the short model geometry length also causes fast cooling on the fiber. The equation below shows the reorganized energy equation:

$$\frac{dT_f}{dz} = -0.764 \cdot \frac{\pi K_a}{\rho_f C_{pf} Q} \cdot \left( \frac{2\rho_a V_a}{\mu_a} \right)^{0.38} \cdot r^{0.38} \cdot (T_f - T_a) \quad (65)$$

The variable in this equation is  $r$ ,  $T_f$  and  $z$ . The remaining parameters are constant. It is obvious that the large  $r$  value will draw a large temperature gradient which makes the cooling faster. With the short model geometry length, the fiber is quickly cooled down to the solidification temperature, which stops the iterative calculation. Therefore this kind of iteration method is not appropriate to simulate this process.

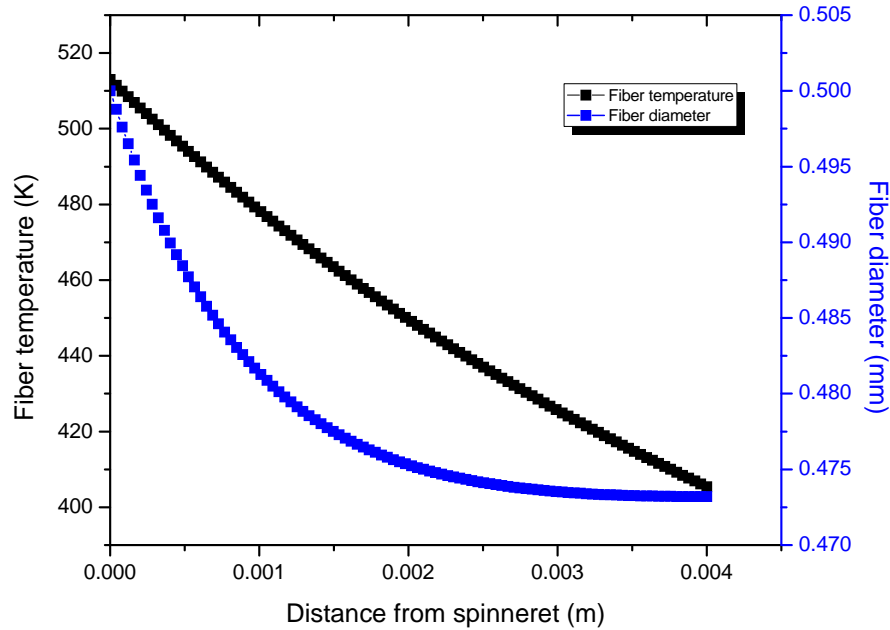


Figure 7.13 Non-isothermal model: fiber diameter and temperature.



As discussed in the isothermal model, the fiber attenuation nearly stops after its diameter reaches the plateau region which usually starts at some position very close to the die orifice. Therefore, it is reasonable to use the starting position of this plateau region as the fiber attenuation stop point. To address the problem in the previous model, a manual iteration method was developed. In this method, an initial value of the model geometry length is guessed. Then a non-isothermal model is simulated based on this guessed model geometry length. The simulated fiber temperature profile will then be used to identify the solidification point. If this solidification point exactly falls on the starting position of the fiber diameter plateau region, it proves that the initially guessed model geometry length is correct. If it falls on the attenuation region, it means the initially guessed model length is too small. The value of model geometry length needs to be increased gradually until it matches the value of solidification point. On the other hand, the initial value of model geometry length needs to be decreased if the solidification point falls after the starting position of the fiber diameter flatten region.

With this new method, an initial model geometry length was set to 5 cm for the previous case. The selection of 5cm is based on the study of Shambaugh and Uyttendaele [70] whose simulation results showed that it provides a good fit and permits the solution to converge. The simulated results are shown in Figure 7.14. The solidification temperature of 135°C corresponding to a solidification position of 1 cm is also the starting position of the fiber diameter flatten region. Based on this method, the final fiber diameter was determined as 7.5  $\mu\text{m}$  which is very close to the experiment result of 6.8  $\mu\text{m}$ . The favorable match with experiment data suggests that the modified method is reasonable to represent our process.

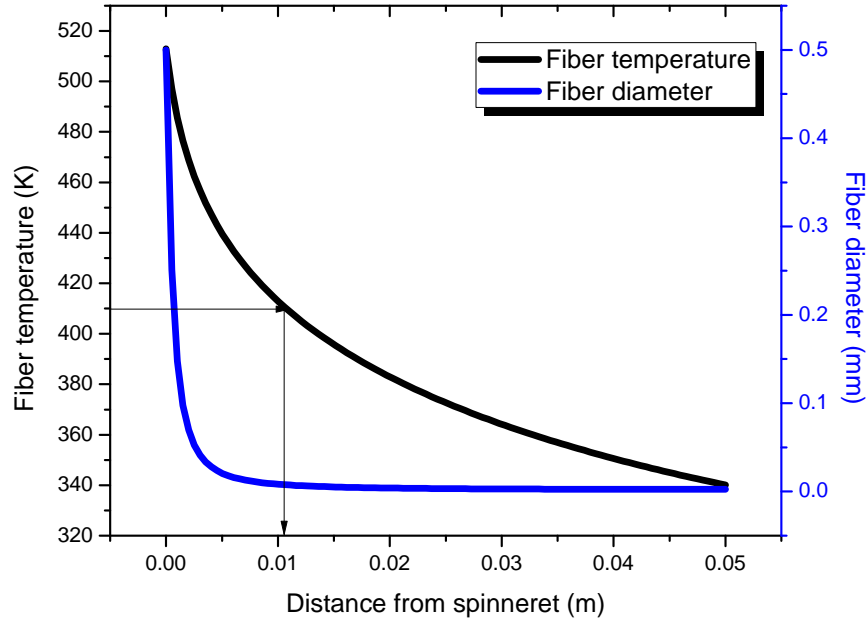


Figure 7.14 Non-isothermal model: fiber diameter and temperature with processing temperature at 240°C and stop point position set at 5 cm.

### 7.7.2. Effect of Processing Temperature

Figure 7.15 shows the simulation results based on previous case but with a 20°C decrease in processing temperature. The iteration indicates that 4.5 cm is a proper value for the model geometry length. The decrease in processing temperature causes an increase in polymer viscosity which restrains the fiber attenuation. Hence, the model geometry length shifts from 5 cm to 4.5 cm when the temperature decreases by 20°C. As expected, the final fiber diameter increases to 11  $\mu\text{m}$ . Therefore, the non-isothermal model also predicts that the fiber diameter decreases with the increase of processing temperature.

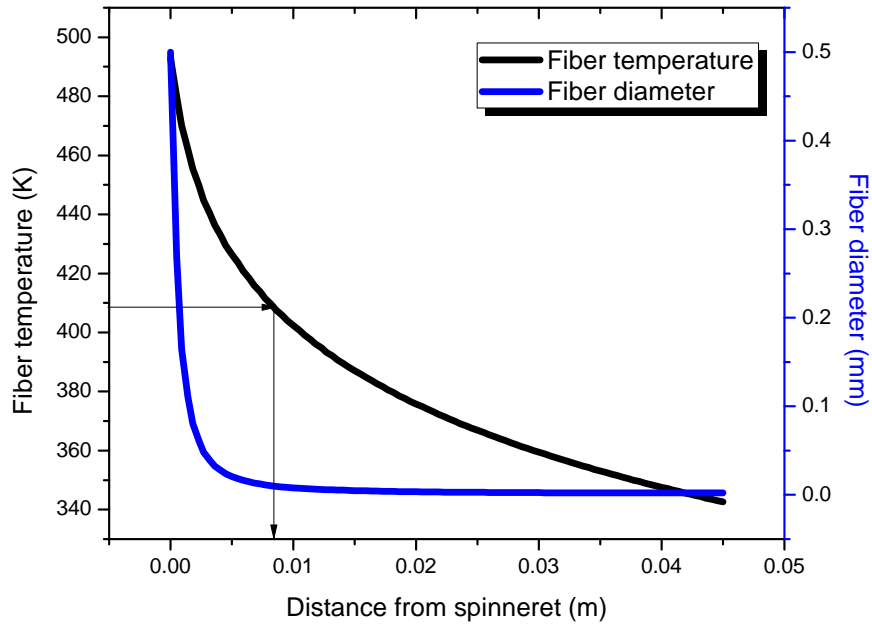


Figure 7.15 Non-isothermal model: fiber diameter and temperature with processing temperature at 220°C and stop point position set at 4.5 cm.

### 7.7.3. Effect of Air Flow Speed

The experiments results showed that the fiber diameter decreases with the increase of air flow velocity. Once the air flow velocity exceeds some critical value, the fiber does not attenuate anymore and has reached the final diameter. This is because that the air velocity affects two competing factors: the air drag force and the cooling rate. Both factors increase with the increase of the air velocity. When the air velocity or air/polymer velocity ratio is low to median, the increase of air drag force is dominant over that of cooling rate. Once some critical point is exceeded, the increase of cooling rate becomes significant and comparable with the increase of air drag force. Hence, the competitive effects resulted from these two factors may counterbalance each other and show a negligible influence on fiber attenuation.

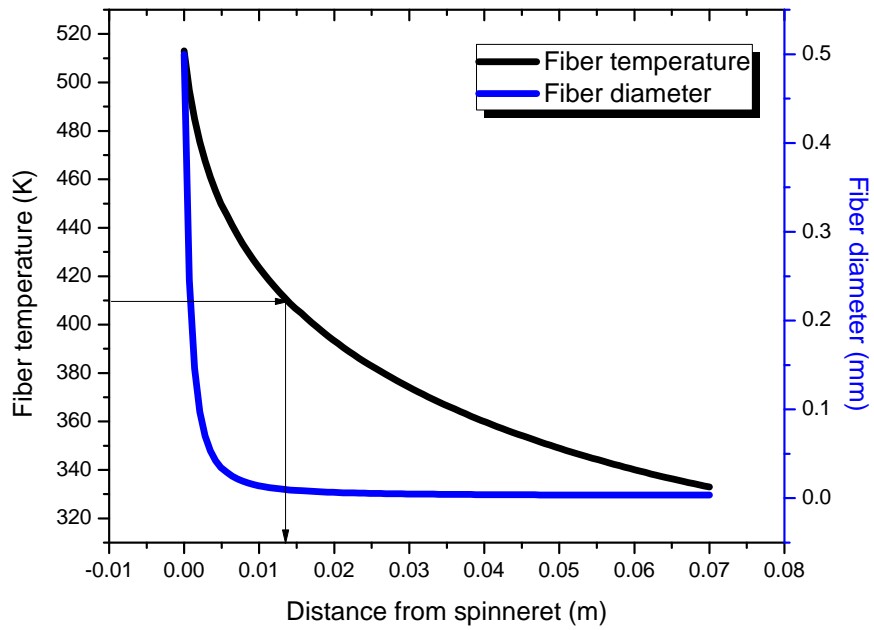


Figure 7.16 Non-isothermal model: fiber diameter and temperature with air velocity of 10 m/s and stop point position set at 7 cm.

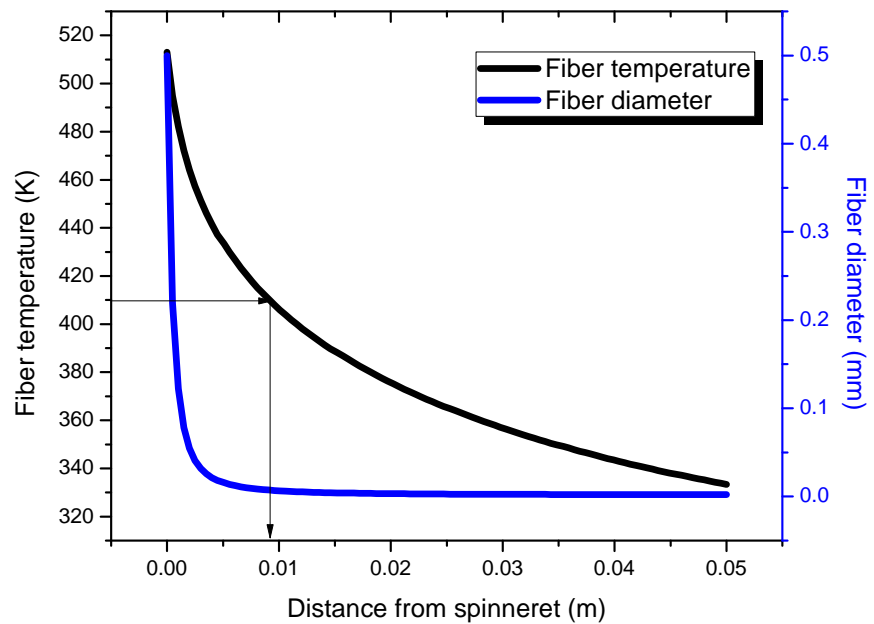


Figure 7.17 Non-isothermal model: fiber diameter and temperature with air velocity of 35 m/s and stop point position set at 5 cm.

The experiment data used here has extremely small polymer flow velocity which means that the air/polymer velocity ratio is extremely high even with air velocity at 20 m/s. Three different levels of air velocity (10 m/s, 22 m/s and 35 m/s) were chosen for the comparative studies, while the other parameters were kept the same as those shown in Table 7-3. The case of 22 m/s was simulated in the previous section and the final diameter was about 7.5 $\mu$ m. For air velocity of 10 m/s, the simulated final fiber diameter was 9.5  $\mu$ m as shown in Figure 7.16. When the air speed increases to 35 m/s, the final fiber diameter is 7.0  $\mu$ m as shown in Figure 7.17. The simulation results agree with the experimental observations that only a minor change on the final diameter occurs when the air velocity increases from 10 m/s to 22 m/s and to 35 m/s. In addition, the solidification point with temperature of 135°C was found shifted from 1.4 cm to 1.1 cm and to 0.9 cm when the air velocity increased from 10 m/s to 22 m/s and to 35 m/s. This phenomenon also indicates that the cooling rate increases with the increase of air velocity.

#### 7.7.4. Effect of Initial Fiber Velocity

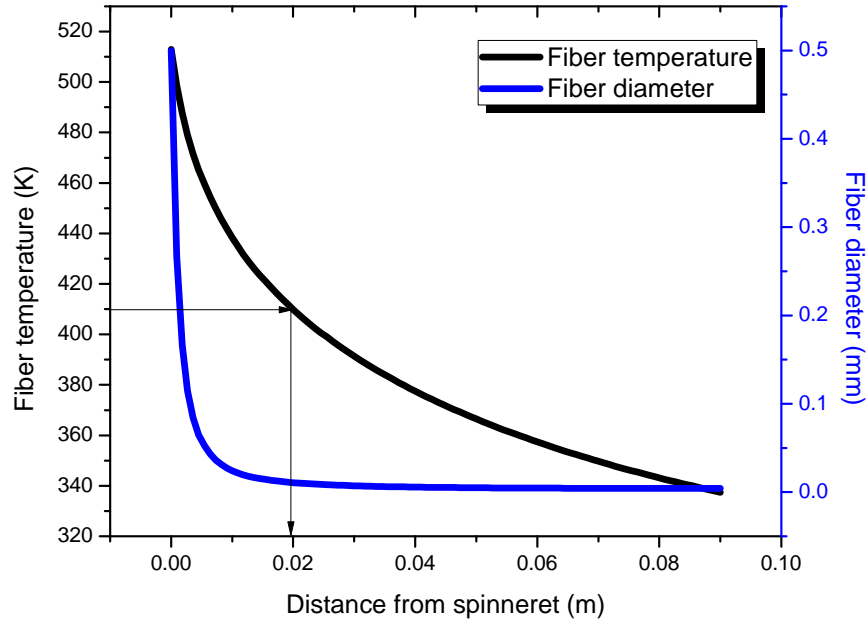


Figure 7.18 Non-isothermal model: fiber diameter and temperature with initial fiber velocity at 0.01 m/s and stop point position set at 9 cm.

Figure 7.18 shows the simulation results when the initial fiber velocity increased to 0.01 m/s from 0.005 m/s. The simulation results of the original case with initial fiber velocity 0.005 m/s is shown in Figure 7.14. By doubling the initial fiber velocity, the final fiber diameter is found to increase from 7.5  $\mu\text{m}$  to 10.5  $\mu\text{m}$ . As concluded in the isothermal model studies, an increase of initial fiber velocity will cause an increase of final fiber diameter. Meanwhile, the increase of initial fiber velocity also slows down the cooling rate. As indicated in the simulation results, the solidification point shifts from 1.1 cm to 1.9 cm which means a slow cooling rate has occurred. The resulting higher fiber temperature improves the fiber attenuation but limits the decrease of final fiber diameter to 3  $\mu\text{m}$  in this study.

#### **7.7.5. Comparisons Between Experimental Results and Model Simulation Results**

The non-isothermal Newtonian model was carried out to predict the fiber final diameter based on the processing temperature, initial fiber velocity and air velocity, as listed in Table 7-4. The data of material properties are listed in Table 7-3, including the density, viscosity, thermal conductivity and heat capacity for both air and polypropylene.

Most of the simulated results are close to the experimental results except for the case 1 and 4 which show large deviation from the experiment values. Compared with the remaining cases, these two cases are observed with relatively small air velocity and air/polymer velocity ratio. The small air velocity and air/polymer velocity ratio cause a slow cooling of the filament as observed in the experimental studies. This slow cooling phenomenon was also observed in the simulation. For those two cases, the solidification point with temperature at 135°C was found located outside of the air nozzle which is about 2 cm in length. Once the air escapes the nozzle channel and exposes to the atmosphere, its velocity will start to decrease dramatically and the air drag force will also vanish after a short distance. In this case, the fiber attenuation stops very quickly and results in a large fiber diameter. However, in the simulation, the fiber will keep being attenuated under the same air velocity outside the nozzle until the temperature reaches the solidification temperature because of a constant air velocity is used in this model. Therefore a smaller diameter was obtained in simulation compared with that in the experimental study. This problem has little effect on the results of cases with high air velocity and high air/polymer velocity ratio. In these cases, the solidification points were found inside the air nozzle by measuring the fiber temperature experimentally and the fiber attenuation was already terminated beyond the fiber solidification point.

Table 7-4 Comparisons between experimental results and simulation results on final fiber diameter under various processing conditions.

Case	Processing temperature (°C)	Air velocity (m/s)	Initial fiber velocity (m/s)	Air/polymer velocity ratio	Tested fiber diameter (μm)	Predicted fiber diameter (m/s)
1	180	24	0.056	429	143	47
2	180	56	0.035	1600	47	43
3	180	80	0.032	2500	38	42
4	200	24	0.069	348	69	30
5	200	24	0.036	667	40	30
6	200	56	0.036	1556	31	25
7	220	24	0.024	1000	27	20
8	220	24	0.016	1500	21	18
9	220	24	0.008	3000	18	16
10	220	56	0.009	6222	13	11
11	240	24	0.038	632	26	18
12	240	56	0.068	824	20	17
13	240	56	0.017	3294	11	13
14	240	24	0.005	4800	7	7.5

One approach to address this problem is to take the fiber diameter at the position of actual nozzle length as the final fiber diameter. With this approach, the final fiber diameter is 97 μm for case 1 and 52 μm for case 4 which are closer than the previous predictions. To achieve a better prediction for the cases with small air velocity and air/polymer velocity ratio, the air velocity value used in the simulation needs to be corrected with the actually measured value of air velocity outside the air nozzle. A data



fitting procedure may be used to correlate the air velocity with its position. With this adjustment, better predictions would be expected.

## **CHAPTER 8**

### **CONCLUSIONS AND SUGGESTIONS FOR FUTURE STUDIES**

#### **8.1. Conclusions**

An apparatus has been developed to melt-spin ultra fine continuous filaments with only cold air drawing. Parametric experimental studies were carried out to study the effects of processing conditions on the resulting fiber properties. A theoretical process model was established and used to study the fiber attenuation mechanism under cold air drawing. Polypropylene was used as a model polymer in these studies. From the experimental and theoretical studies, the following conclusions can be drawn:

1. The fibers produced by the new process showed a uniform diameter and a smooth surface appearance. The fiber diameter is highly dependent on the polymer viscosity and the processing conditions, including the processing temperature and the air/polymer flow ratio. The fiber diameter was found to decrease with increasing of air/polymer flow ratio and processing temperature, and with decreasing of polymer viscosity and initial fiber velocity. Fibers with diameter of 7 $\mu$ m were successfully produced from a spinneret with a 0.5 mm diameter orifice.
2. Fiber molecular orientation increases with the increase of air/polymer flow ratio. The maximum molecular orientation was observed at mild processing temperature (200-220°C). The fiber mechanical properties were found to correlate with the molecular orientation. The tensile strength and modulus increase with the increase of air/polymer flow ratio. The single filament with diameter of 10  $\mu$ m (without

post drawing) exhibits moderately high mechanical properties with a tensile strength of 100 MPa and a tensile modulus of 2.5 GPa.

3. Orientation induced crystallization was found to be dominant in our process. The fiber crystallinity increases with the increase of air/polymer flow ratio accompanied by an increase in molecular orientation. Low crystallinity fibers were found to associate with high processing temperature at relatively low air/polymer flow ratio. Only  $\alpha$ -monoclinic crystalline was formed for the produced polypropylene fibers.
4. For further demonstration, this process was also successfully applied to other polymer materials, including Nylon-6.
5. An isothermal Newtonian fluid model was developed to analyze the single factor effect of processing conditions on fiber diameter. A non-isothermal Newtonian fluid model was implemented to predict the fiber final diameter under different processing conditions. The predicted values compare favorably with the experimental data.

## **8.2. Suggestions for Future Studies**

The future studies are suggested for the experimental apparatus, experimental studies and theoretical modeling.

Apparatus: the processing temperature is limited to below 260°C because it is the maximum operation temperature of Teflon which is used in the spinneret pack as a thermal insulation. In addition, the fiber is surrounded by the stainless steel spinneret pack which makes it impossible to measure the fiber diameter and temperature online. To

overcome these limitations, a new design of spinneret pack is proposed to satisfy the following requirements.

1. A high-temperature insulation piece with operation temperature over 400°C will allow processing some high melting point polymer materials with broad processing temperatures, such as Nylon and PET.
2. A transparent air chamber and air nozzle with access to a high speed camera and an Infrared camera would facilitate online measurement of the fiber diameter and the temperature distribution along the spinline.
3. Several air nozzles with different channel length would provide various cooling times at the same air flow velocity.

Experimental studies: with a new experimental setup, a series of experiments can be carried out to study the PET fiber crystallization behavior under cold air cooling and attenuation. As a slowly crystallizing polymer, PET is anticipated to have different crystallization behavior resulted from the different thermal environment provided by cold air cooling. Specifically, the crystallinity of PET fiber can be controlled by changing the air flow speed and the length of nozzle. Theoretically, with high air flow, highly orientated amorphous PET fibers may be obtained.

Theoretical modeling:

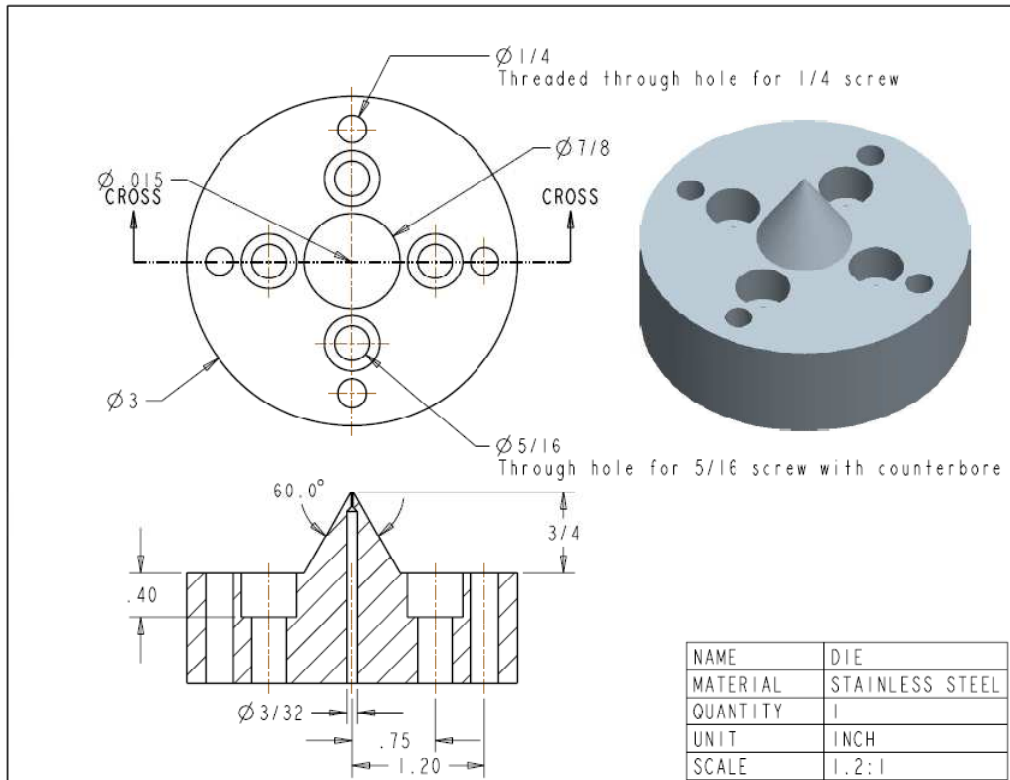
1. Adjust the air velocity in the model with more accurate air velocity profile inside and outside air nozzle for better predictions.
2. The data from online measurements of fiber diameter and temperature profile can be used to validate the modeling results. The air drag coefficient and convection

heat transfer coefficient may be modified for better predictions based on online measurement data.

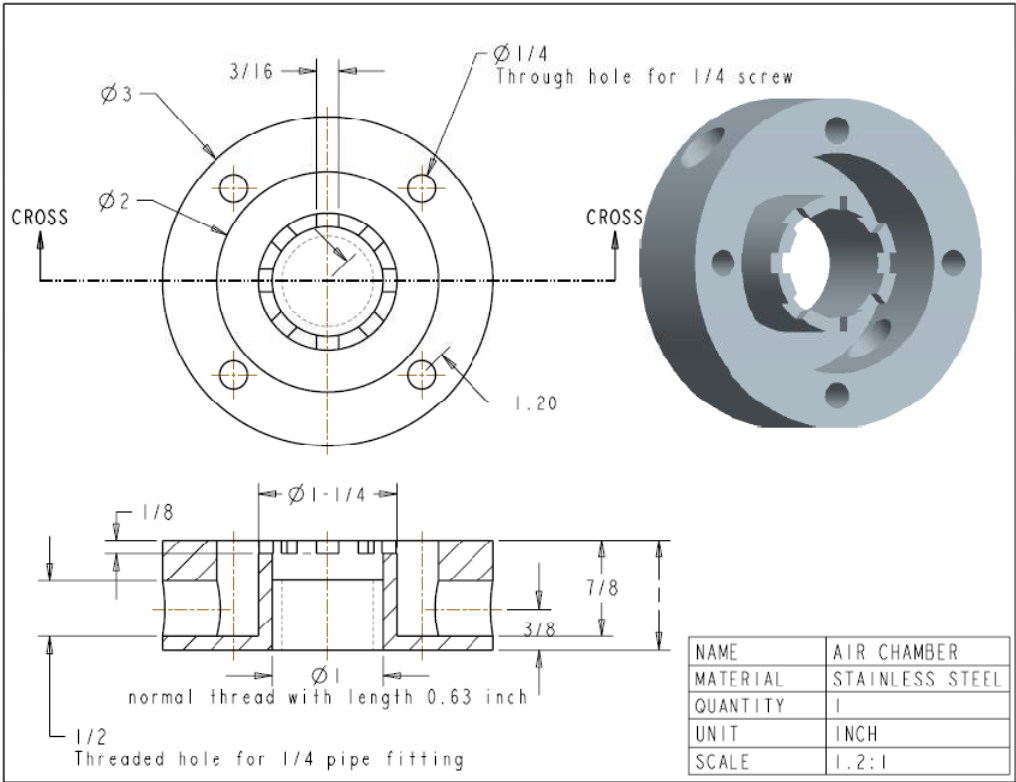
# APPENDIX A

## DRAWING OF SPINNERET PACK

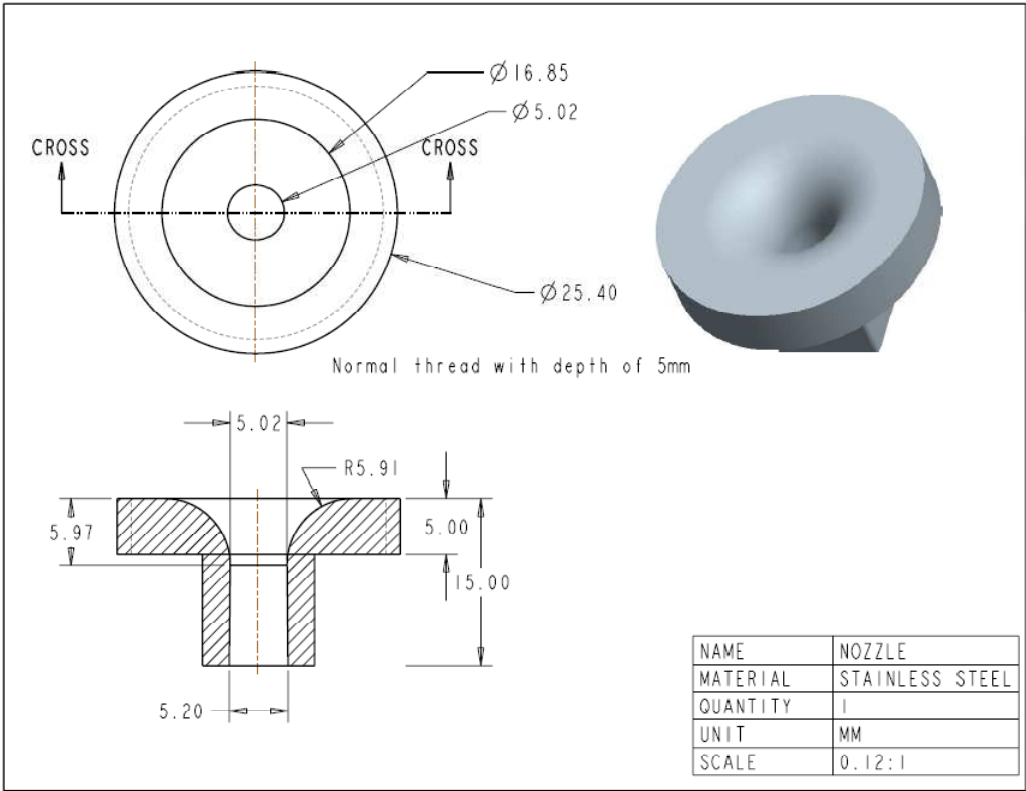
### A.1. Spinneret Die



### A.2. Air Chamber

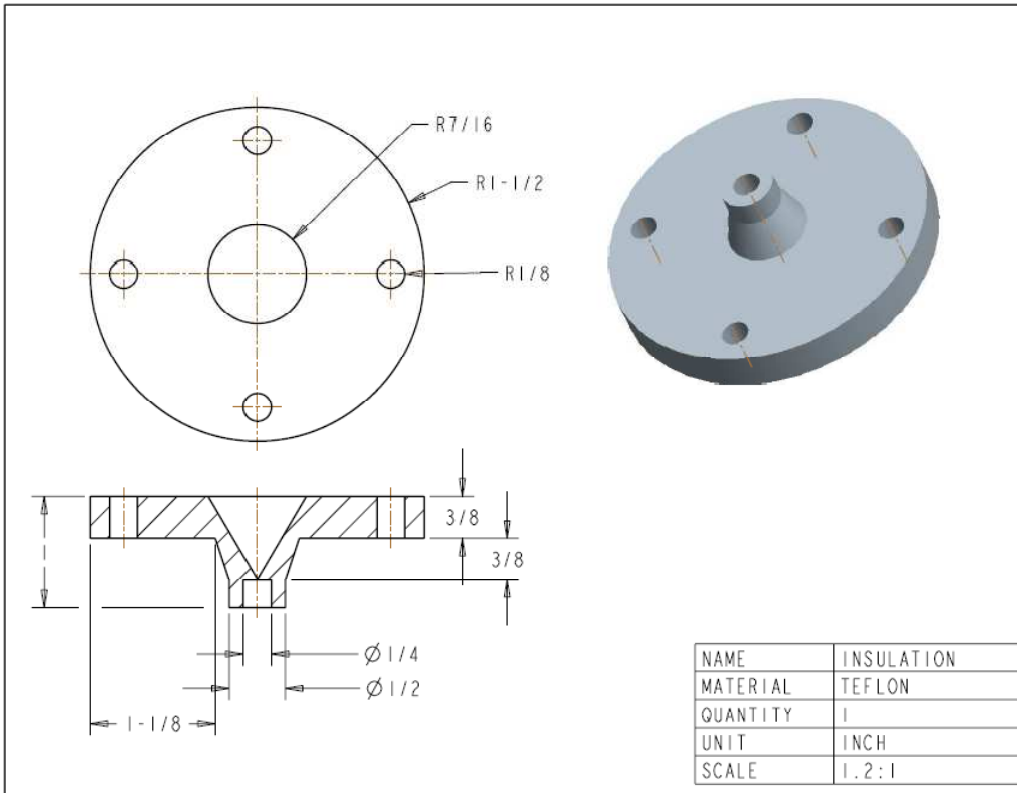
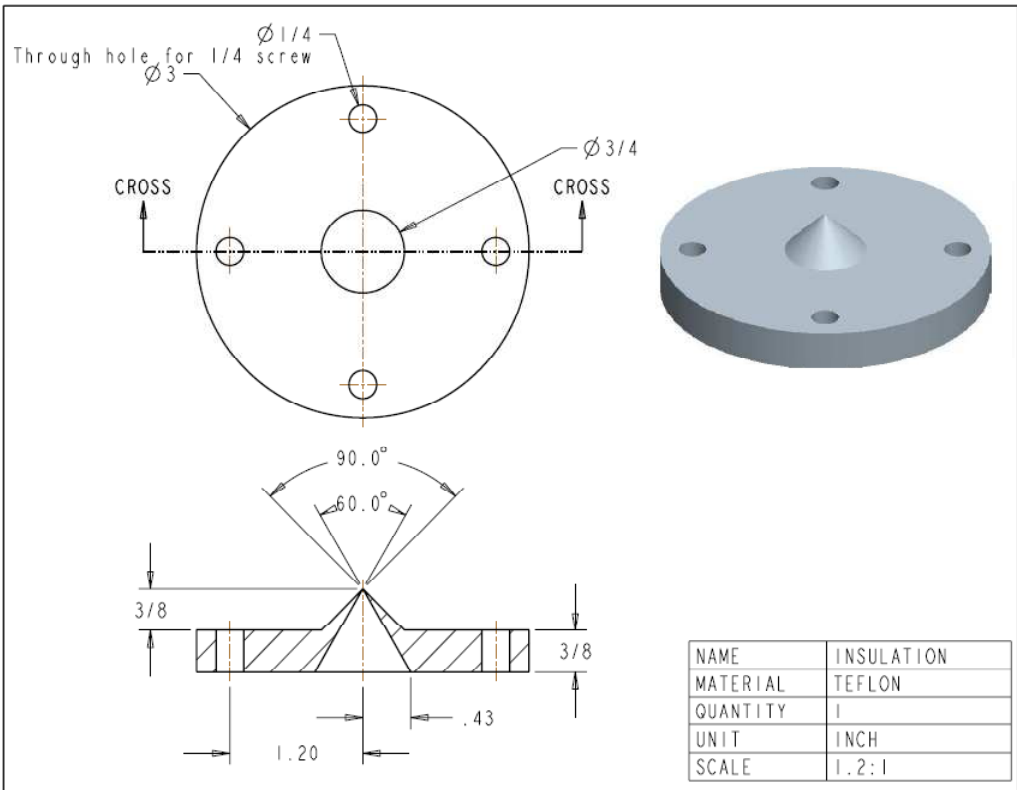


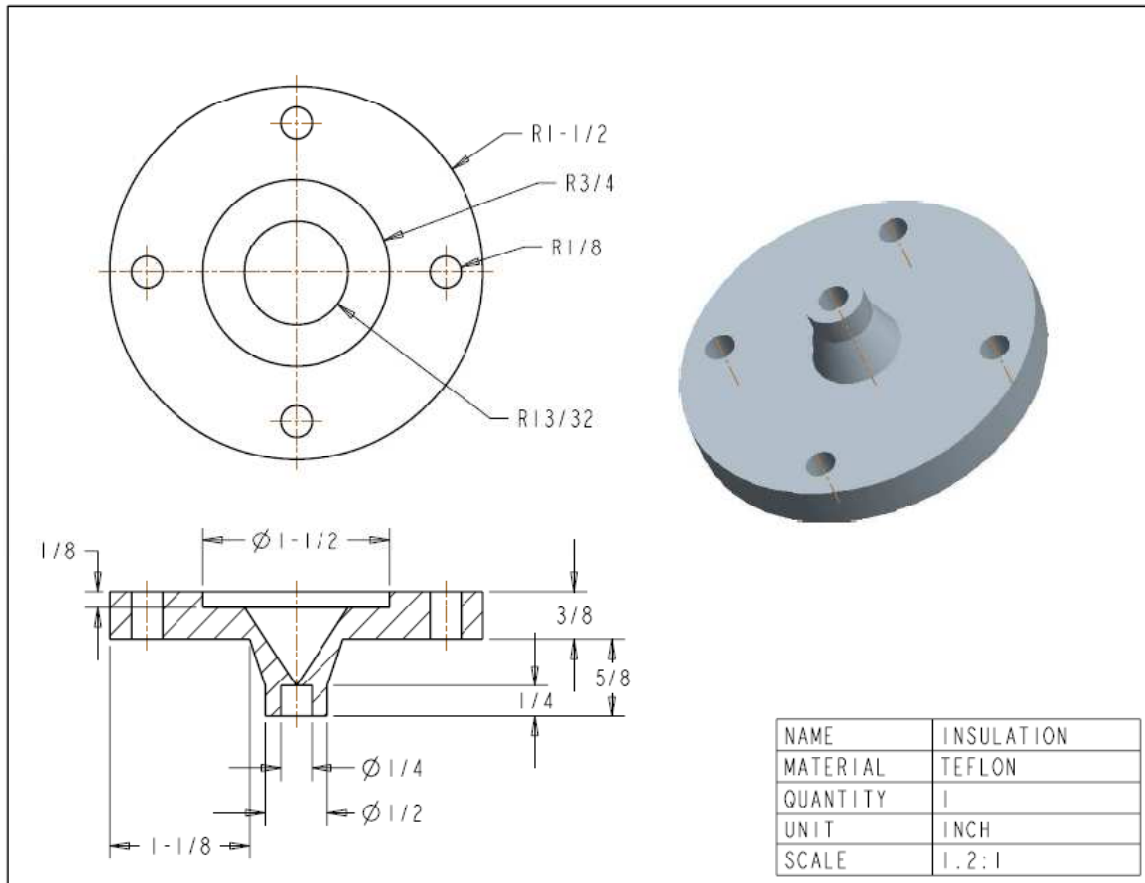
A.3. Air Nozzle





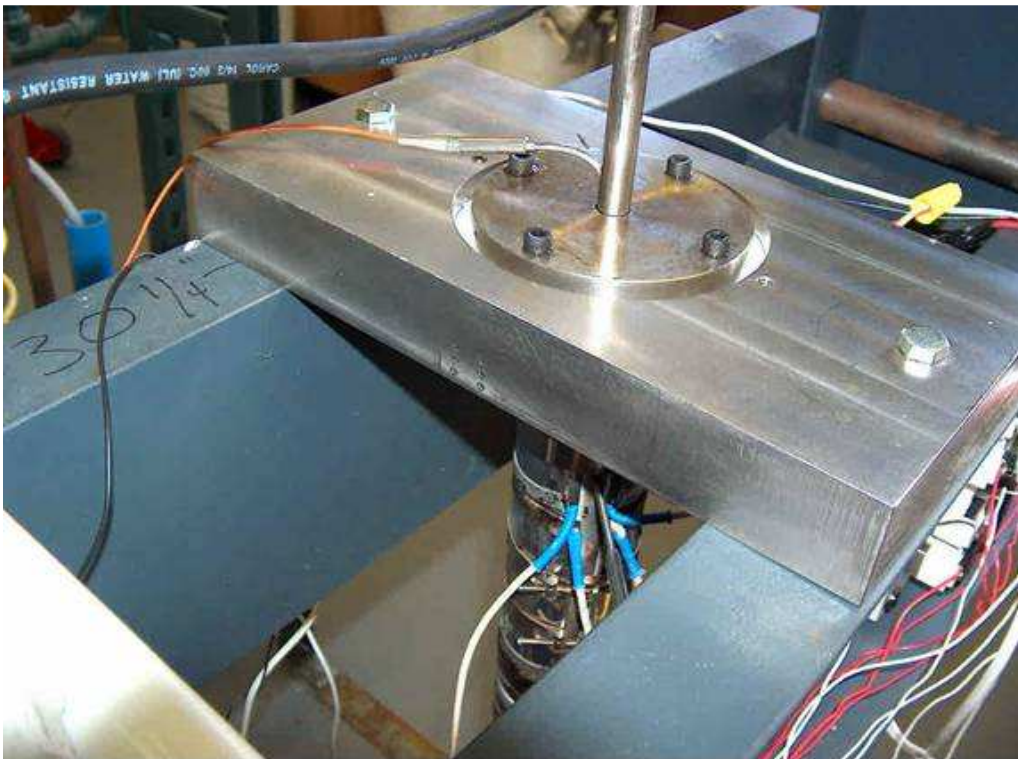
#### A.4. Insulation Piece

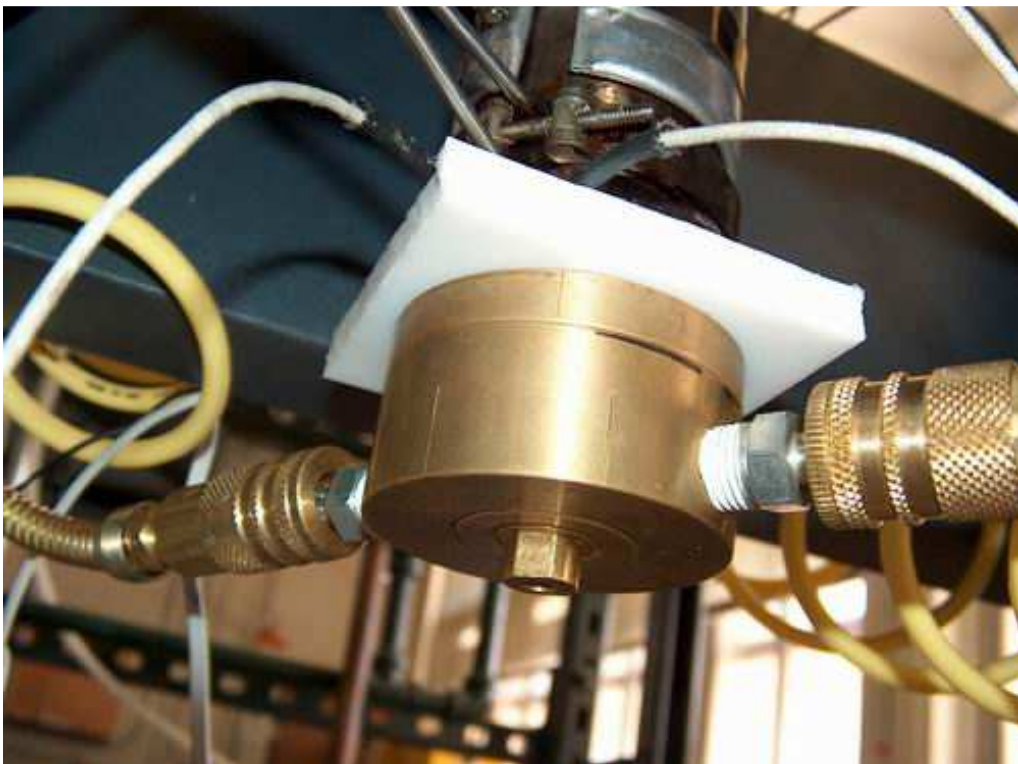




## APPENDIX B

### PICTURE OF FIBER EXTRUDER







## APPENDIX C

### MATLAB CODES FOR THEORETICAL MODELING

#### C.1. Validation Model

Simplified ODE equation:

$$\frac{d^2V_f}{dz^2} = \frac{1}{V_f} \cdot \left( \frac{dV_f}{dz} \right)^2 + \frac{\rho_f}{3\eta} \cdot V_f \cdot \frac{dV_f}{dz} - \frac{\rho_f}{3\eta} \cdot g \quad (66)$$

```
vf0=0.003;  
rhof=900;  
muf=300;  
b=rhof/3/muf;  
L=0.1;  
x=linspace(0,L,10);  
yinit=@(x)[10;10];  
solinit = bvpinit(x,yinit);  
odefun=@(x,y)[y(2);y(2)^2/y(1)-9.8*b+y(1)*y(2)*b];  
bcfun=@(ya,yb)[ya(1)-vf0;yb(2)];  
sol = bvp4c(odefun,bcfun,solinit);  
xint = linspace(0,L);  
Sxint = deval(sol,xint);  
plot(xint,Sxint(1,:));  
[xint' Sxint(1,:)']
```

#### C.2. Isothermal Model

Simplified ODE equation:

$$\frac{d^2V_f}{dz^2} = \frac{1}{V_f} \left( \frac{dV_f}{dz} \right)^2 - 0.78 \frac{\rho_a}{3\eta} \left( \frac{2V_a\rho_a}{\mu_a} \right)^{-0.61} \left( \frac{\pi V_f}{Q} \right)^{0.805} (V_a - V_f)^2 + V_f \frac{\rho_f}{3\eta} \frac{dV_f}{dz} - g \frac{\rho_f}{3\eta} \quad (67)$$

```
va=100;  
vf0=0.01;
```

```

rhoa=1.2;
rhof=900;
Qf=pi*vf0*0.00025^2;
muf=100;
mua=2e-5;
a=0.78*(2^-.61)*(mua/rhoa)^.61*(pi/Qf)^.805*rhoa*va^-.
.61/3/muf;
b=rhof/3/muf;
L=0.05;
x=linspace(0,L,10);
yinit=@(x)[100;100];
solinit = bvpinit(x,yinit);
odefun=@(x,y)[y(2);y(2)^2/y(1)-a*y(1)^0.805*(va-y(1))^2-
9.8*b+y(1)*y(2)*b];
bcfun=@(ya,yb)[ya(1)-vf0;yb(2)];
sol = bvp4c(odefun,bcfun,solinit);
xint = linspace(0,L);
Sxint = deval(sol,xint);
plot(xint,Sxint(1,:));
z=2*(Qf/pi./Sxint(1,:)).^0.5;
plot(xint,z);

```

### C.3. Non-isothermal Model

Simplified ODE equations:

$$\begin{aligned}
\frac{d^2 V_f}{dz^2} = & \frac{1}{V_f} \cdot \left( \frac{dV_f}{dz} \right)^2 + \frac{dV_f}{dz} \cdot \frac{dT_f}{dz} \cdot \frac{5530}{T^2} \\
& + \frac{1}{3 \times 0.002087} \cdot e^{\frac{-5530}{T}} \left[ \rho_f V_f \frac{dV_f}{dz} - \rho_f g - 0.78 \rho_a \left( \frac{2V_a \rho_a}{\mu_a} \right)^{-0.61} \left( \frac{\pi V_f}{Q} \right)^{0.805} (V_a - V_f)^2 \right]
\end{aligned}
\tag{68}$$

$$\frac{dT_f}{dz} = -\frac{0.4 \times 0.764 \kappa_a \left( \frac{2V_a \rho_a}{\mu_a} \right)^{0.38} \left( \frac{\pi}{Q} \right)^{0.81} V_f^{-0.19} (T_f - T_a)}{\rho_f C_{pf}} \quad (69)$$

### **Method 1:**

```

va=24;
vf0=0.005;
rhoa=1.2;
rhof=900;
Qf=pi*vf0*0.00025^2;
m=0.002087;
mua=2e-5;
ka=0.027;
cp=2000;
a=0.78*(mua/2/rhoa/va)^.61*(pi/Qf)^.805*rhoa/3/m;
b=rhof/3/m;
c=0.4*0.764*ka*(2*rhoa*va/mua)^.38*(pi/Qf)^.81/rhof/cp;
i=1;
while 1
d=0.001*i;
x=linspace(0,d,10);
yinit=@(x)[20;100;520];
solinit = bvpinit(x,yinit);
odefun=@(x,y)[y(2);y(2)^2/y(1)-a*y(1)^0.805*(va-
y(1))^2/exp(5530/y(3)))-
9.8*b/exp(5530/y(3))+y(1)*y(2)*b/exp(5530/y(3))-
c*y(2)*(y(3)-300)*y(1)^(-.19)*5530/y(3)^2;-c*(y(3)-
300)*y(1)^-.19];
bcfun=@(ya,yb)[ya(1)-vf0;yb(2);ya(3)-513];
sol = bvp4c(odefun,bcfun,solinit);
xint = linspace(0,d);
Sxint = deval(sol,xint);
i=i+1;

```

```

if (Sxint(3,100)-410<=0),break,end
end
plot(xint,Sxint(1,:));
z=2*(Qf/pi./Sxint(1,:)).^0.5;
plotyy(xint,Sxint(3,:),xint,z);

```

## **Method 2**

```

va=22;
vf0=0.01;
rhoa=1.2;
rhof=900;
Qf=pi*vf0*0.00025^2;
m=0.002087;
mua=2e-5;
ka=0.027;
cp=2000;
a=0.78*(mua/2/rhoa/va)^.61*(pi/Qf)^.805*rhoa/3/m;
b=rhof/3/m;
c=0.4*0.764*ka*(2*rhoa*va/mua)^.38*(pi/Qf)^.81/rhof/cp;
d=0.09;
x=linspace(0,d,10);
yinit=@(x)[100;200;350];
solinit = bvpinit(x,yinit);
odefun=@(x,y)[y(2);y(2)^2/y(1)-a*y(1)^0.805*(va-
y(1))^2/exp(5530/y(3)) -
9.8*b/exp(5530/y(3))+y(1)*y(2)*b/exp(5530/y(3)) -
c*y(2)*(y(3)-300)*y(1)^(-.19)*5530/y(3)^2;-c*(y(3)-
300)*y(1)^-.19];
bcfun=@(ya,yb)[ya(1)-vf0;yb(2);ya(3)-513];
sol = bvp4c(odefun,bcfun,solinit);
xint = linspace(0,d);

```



```
Sxint = deval(sol,xint);  
plot(xint,Sxint(1,:));  
z=2*(Qf/pi./Sxint(1,:)).^0.5;  
plotyy(xint,Sxint(3,:),xint,z);  
[xint' Sxint(3,:) z'*1000]
```

## REFERENCES

1. Hongu, T., Phillips, G.O., and Takigami, M., *New millennium fibers*. 2005, Cambridge, England: Woodhead Publishing Limited.
2. Wentz, V.A., *Superfine thermoplastic fibers*. Industrial and Engineering Chemistry, 1956. **48**(8): p. 1342-1346.
3. Burger, C., Hsiao, B.S., and Chu, B., *Nanofibrous materials and their applications*. Annual Review of Materials Research, 2006. **36**: p. 333-368.
4. Huang, Z.M., et al., *A review on polymer nanofibers by electrospinning and their applications in nanocomposites*. Composites Science and Technology, 2003. **63**(15): p. 2223-2253.
5. Suzuki, A. and Hasegawa, T., *High temperature zone-drawing of nylon 66 microfiber prepared by CO<sub>2</sub> laser-thinning*. Journal of Applied Polymer Science, 2006. **101**(1): p. 42-47.
6. Suzuki, A. and Hasegawa, T., *Superstructure and mechanical properties of nylon 66 microfiber prepared by carbon dioxide laser-thinning method*. Journal of Applied Polymer Science, 2006. **99**(3): p. 802-807.
7. Suzuki, A. and Ishihara, M., *Application of CO<sub>2</sub> laser heating zone drawing and zone annealing to nylon 6 fibers*. Journal of Applied Polymer Science, 2002. **83**(8): p. 1711-1716.
8. Suzuki, A. and Kamata, K., *Nylon 6 microfiber prepared by carbon dioxide laser heating*. Journal of Applied Polymer Science, 2004. **92**(3): p. 1449-1453.
9. Suzuki, A. and Kamata, K., *Nylon 6 microfiber obtained method with a carbon dioxide laser*. Journal of Applied Polymer Science, 2004. **92**(3): p. 1454-1458.
10. Suzuki, A. and Mizuochi, D., *Zone-drawing and zone-annealing of poly(L-lactic acid) microfiber prepared by CO<sub>2</sub> laser-thinning method*. Journal of Applied Polymer Science, 2006. **102**(1): p. 472-478.

11. Suzuki, A. and Mochiduki, N., *Mechanical properties and superstructure of poly(ethylene terephthalate) fibers zone-drawn and zone-annealed by CO<sub>2</sub> laser heating*. Journal of Applied Polymer Science, 2001. **82**(11): p. 2775-2783.
12. Suzuki, A. and Mochizuki, N., *Mechanical properties and microstructure of poly(ethylene terephthalate) microfiber prepared by carbon dioxide laser heating*. Journal of Applied Polymer Science, 2003. **90**(7): p. 1955-1958.
13. Suzuki, A. and Mochizuki, N., *PET microfiber prepared by carbon dioxide laser heating*. Journal of Applied Polymer Science, 2003. **88**(14): p. 3279-3283.
14. Suzuki, A. and Narusue, S., *Isotactic polypropylene microfiber prepared by carbon dioxide laser-heating*. Journal of Applied Polymer Science, 2004. **92**(3): p. 1534-1539.
15. Suzuki, A. and Narusue, S., *Isotactic polypropylene microfiber prepared by continuous laser-thinning method*. Journal of Applied Polymer Science, 2006. **99**(1): p. 27-31.
16. Suzuki, A. and Ohnishi, H., *Isotactic polypropylene hollow microfibers prepared by CO<sub>2</sub> laser-thinning*. Journal of Applied Polymer Science, 2006. **102**(3): p. 2600-2607.
17. Suzuki, A. and Okano, T., *Zone drawing and zone annealing of poly(ethylene terephthalate) microfiber prepared by CO<sub>2</sub> laser thinning*. Journal of Applied Polymer Science, 2004. **92**(5): p. 2989-2994.
18. Ye, J.P., Hasegawa, T., and Suzuki, A., *Evaluation of the microstructure and melting behavior of drawn polypropylene fibers with a microthermal analyzer*. Journal of Applied Polymer Science, 2006. **100**(2): p. 1306-1311.
19. Huang, B., Tucker, P.A., and Cuculo, J.A., *High performance poly(ethylene terephthalate) fibre properties achieved via high speed spinning with a modified liquid isothermal bath process*. Polymer, 1997. **38**(5): p. 1101-1110.
20. Wu, G., Tucker, P.A., and Cuculo, J.A., *High performance PET fibre properties achieved at high speed using a combination of threadline modification and traditional post treatment*. Polymer, 1997. **38**(5): p. 1091-1100.

21. Kikutani, T., et al., *Effect of spinline quenching on structure development in high-speed melt spinning of PET- diameter profiles in the spinline*. International Polymer Processing, 1990. **5**(1): p. 20-24.
22. Ledbetter, M., Cuculo, J., and Tucker, P., *Structure and properties of poly(ethylene terephthalate) crystallized by converging flow and high pressure*. Journal of Polymer Science Part a-Polymer Chemistry, 1984. **22**(6): p. 1435-1459.
23. Hotter, J.F., Cuculo, J.A., and Tucker, P.A., *Effects of modified air quenches on the high-speed melt spinning process*. Journal of Applied Polymer Science, 1991. **43**(8): p. 1511-1520.
24. Ziabicki, A., *Fundamentals of fibre formation : the science of fibre spinning and drawing*. 1976: John Wiley & Sons, Ltd.
25. Pinchuk L S, S.L., *Melt blowing : equipment, technology, and polymer fibrous materials*. 2002, Berlin: Springer.
26. Shambaugh, R.L., *A macroscopic view of the melt-blowing process for producing microfibers*. Industrial & Engineering Chemistry Research, 1988. **27**(12): p. 2363-2372.
27. McCulloch, W.J.G. and Jones, A.M. *Recent advances in the Exxon melt blowing process*. 1987. Houston, TX, USA: Soc of Plastics Engineers, Brookfield Center, CT, USA.
28. Robert R. Butin, J.P.K., John W. Harding, in *US Patent*. 1974.
29. Ellison, C.J., et al., *Melt blown nanofibers: Fiber diameter distributions and onset of fiber breakup*. Polymer, 2007. **48**(11): p. 3306-3316.
30. Ainslie, K.M., et al., *Cell adhesion on nanofibrous polytetrafluoroethylene (nPTFE)*. Langmuir, 2007. **23**(2): p. 747-754.
31. Sen, A., et al., *Polytetrafluoroethylene nano/microfibers by jet blowing*. Polymer, 2006. **47**(25): p. 8337-43.

32. Podgorski, A., Balazy, A., and Gradon, L., *Application of nanofibers to improve the filtration efficiency of the most penetrating aerosol particles in fibrous filters*. Chemical Engineering Science, 2006. **61**(20): p. 6804-6815.
33. Bansal, V. and Shambaugh, R.L., *On-line determination of density and crystallinity during melt spinning*. Polymer Engineering and Science, 1996. **36**(22): p. 2785-2798.
34. Bansal, V. and Shambaugh, R.L., *On-line determination of diameter and temperature during melt blowing of polypropylene*. Industrial & Engineering Chemistry Research, 1998. **37**(5): p. 1799-1806.
35. Bansal, V. and Shambaugh, R.L., *On-line density and crystallinity of polyethylene terephthalate during melt spinning*. Polymer Engineering and Science, 1998. **38**(12): p. 1959-1968.
36. Beard, J.H., et al., *On-line measurement of fiber motion during melt blowing*. Industrial & Engineering Chemistry Research, 2007. **46**: p. 7340-7352.
37. De Rovere, A., Shambaugh, R.L., and O'Rear, E.A., *Investigation of gravity-spun, melt-spun, and melt-blown polypropylene fibers using atomic force microscopy*. Journal of Applied Polymer Science, 2000. **77**(9): p. 1921-1937.
38. Kayser, J.C. and Shambaugh, R.L., *The manufacture of continuous polymeric filaments by the melt-blowing process*. Polymer Engineering and Science, 1990. **30**(19): p. 1237-1251.
39. Krutka, H.M., Shambaugh, R.L., and Papavassiliou, D.V., *Analysis of a melt-blowing die: Comparison of CFD and experiments*. Industrial & Engineering Chemistry Research, 2002. **41**(20): p. 5125-5138.
40. Krutka, H.M., Shambaugh, R.L., and Papavassiliou, D.V., *Effects of die geometry on the flow field of the melt-blowing process*. Industrial & Engineering Chemistry Research, 2003. **42**(22): p. 5541-5553.
41. Krutka, H.M., Shambaugh, R.L., and Papavassiliou, D.V., *Effects of temperature and geometry on the flow field of the melt blowing process*. Industrial & Engineering Chemistry Research, 2004. **43**(15): p. 4199-4210.

42. Krutka, H.M., Shambaugh, R.L., and Papavassiliou, D.V., *Effects of the polymer fiber on the flow field from an annular melt-blowing die*. Industrial & Engineering Chemistry Research, 2007. **46**(2): p. 655-666.
43. Krutka, H.M., Shambaugh, R.L., and Papavassiliou, D.V., *Effects of the polymer fiber on the flow field from a slot melt blowing die*. Industrial & Engineering Chemistry Research, 2008. **47**: p. 935-945.
44. Majumdar, B. and Shambaugh, R.L., *Air drag on filaments in the melt blowing process*. Journal of Rheology, 1990. **34**(4): p. 591-601.
45. Marla, V.T. and Shambaugh, R.L., *Three-dimensional model of the melt-blowing process*. Industrial & Engineering Chemistry Research, 2003. **42**(26): p. 6993-7005.
46. Marla, V.T. and Shambaugh, R.L., *Modeling of the melt blowing performance of slot dies*. Industrial & Engineering Chemistry Research, 2004. **43**(11): p. 2789-2797.
47. Marla, V.T., Shambaugh, R.L., and Papavassiliou, D.V., *Modeling the melt blowing of hollow fibers*. Industrial & Engineering Chemistry Research, 2006. **45**(1): p. 407-415.
48. Shambaugh, R.L., *Modeling of the next generation of melt blowing*. Tappi Journal, 1997. **80**(9): p. 163-166.
49. Shambaugh, R.L. and Chhabra, R., *Fiber vibrations and distributions in melt blowing*. Tappi Journal, 1998. **81**(3): p. 199-201.
50. Tate, B.D. and Shambaugh, R.L., *Temperature fields below melt-blowing dies of various geometries*. Industrial & Engineering Chemistry Research, 2004. **43**(17): p. 5405-5410.
51. Gupta, V.B. and Kothari, V.K., *Manufactured fibre technology*. 1997, London, England: Springer-Verlag New York, LLC.
52. Hingmann, R. and Marcinke, B.L., *Shear and elongational flow properties of polypropylene melts*. Journal of Rheology, 1994. **38**(3): p. 573-587.

53. Ishizuka, O. and Koyama, K., *Elongational viscosity at a constant elongational strain rate of polypropylene melt*. Polymer, 1980. **21**(2): p. 164-170.
54. Nakajima, T., *Advanced fiber spinning technology*. 1994, Cambridge, England: Woodhead Publishing Ltd.
55. Dees, J.R. and Spruiell, J.E., *Structure development during melt spinning of linear polyethylene fibers*. Journal of Applied Polymer Science, 1974. **18**(4): p. 1053-1078.
56. Keller, A., *Unusual orientation phenomena in polyethylene interpreted in terms of the morphology*. Journal of Polymer Science, 1955. **15**(79): p. 31-49.
57. Kase, S. and Matsuo, T., *Studies on melt spinning. I. Fundamental equations on the dynamics of melt spinning*. Journal of Polymer Science Part a-General Papers, 1965. **3**(7PA): p. 2541-&.
58. Kase, S. and Matsuo, T., *Studies on melt spinning. II. Steady-state and transient solutions of fundamental equations compared with experimental results*. Journal of Applied Polymer Science, 1967. **11**(2): p. 251-&.
59. Morrison, M.E., *Numerical evaluation of temperature profiles and interface position in filaments undergoing solidification*. Aiche Journal, 1970. **16**(1): p. 57-&.
60. Moutsoglou, A., *On the cooling of fibers*. Journal of Heat Transfer-Transactions of the Asme, 1983. **105**(4): p. 830-834.
61. Doufas, A.K. and McHugh, A.J., *Two-dimensional simulation of melt spinning with a microstructural model for flow-induced crystallization*. Journal of Rheology, 2001. **45**(4): p. 855-879.
62. Doufas, A.K., McHugh, A.J., and Miller, C., *Simulation of melt spinning including flow-induced crystallization - Part I. Model development and predictions*. Journal of Non-Newtonian Fluid Mechanics, 2000. **92**(1): p. 27-66.
63. Doufas, A.K., et al., *Simulation of melt spinning including flow-induced crystallization - Part II. Quantitative comparisons with industrial spinline data*. Journal of Non-Newtonian Fluid Mechanics, 2000. **92**(1): p. 81-103.

64. Kim, K.H., Isayev, A.I., and Kwon, K., *Simulation and experimental verification of crystallization and birefringence in melt spinning of PET*. International Polymer Processing, 2006. **21**(1): p. 49-63.
65. Lee, Y. and Wadsworth, L.C., *Effects of melt-blowing process conditions on morphological and mechanical properties of polypropylene webs*. Polymer, 1992. **33**(6): p. 1200-1209.
66. Cheng, C.Y., Malkan, S.R., and Wadsworth, L.C., *Study of process-structure-property relationships in melt blowing of different melt flow rate polypropylene resins*. Abstracts of Papers of the American Chemical Society, 1988. **195**: p. 63-CELL.
67. Ellison, C.J., et al., *Melt blown nanofibers: Fiber diameter distributions and onset of fiber breakup (vol 48, pg 3306, 2007)*. Polymer, 2007. **48**(20): p. 6180-6180.
68. Swiatek, J., Jarzebowski, J., and Cichon, J., *Investigation of Fibre Diameter Distribution in Non-Woven Textiles for Medical Applications in Melt-Blown Polyester Technology*. Fibres & Textiles in Eastern Europe, 2008. **16**(3): p. 14-16.
69. Lee, Y.C. and Wadsworth, L.C., *Structure and filtration properties of melt blown polypropylene webs*. Polymer Engineering and Science, 1990. **30**(22): p. 1413-1419.
70. Uyttendaele, M.A.J. and Shambaugh, R.L., *Melt blowing - General equation development and experimental verification*. Aiche Journal, 1990. **36**(2): p. 175-186.
71. Rao, R.S. and Shambaugh, R.L., *Vibration and stability in the melt blowing process*. Industrial & Engineering Chemistry Research, 1993. **32**(12): p. 3100-3111.
72. Chen, T., Wang, J., and Huang, X.B., *Artificial neural network modeling for predicting melt-blowing processing*. Journal of Applied Polymer Science, 2006. **101**(6): p. 4275-4280.
73. Boye, C.A., Watson, M.T., and Patton, H.W., *Comment on the structure of quenched isotactic polypropylene*. Journal of Polymer Science, 1959. **39**(135): p. 534-535.



74. Choi, C.H. and White, J.L., *Correlation and modeling of the occurrence of different crystalline forms of isotactic polypropylene as a function of cooling rate and uniaxial stress in thin and thick parts*. Polymer Engineering and Science, 2000. **40**(3): p. 645-655.
75. Arvidson, S.A., Khan, S.A., and Gorga, R.E., *Mesomorphic-alpha-Monoclinic Phase Transition in Isotactic Polypropylene: A Study of Processing Effects on Structure and Mechanical Properties*. Macromolecules. **43**(6): p. 2916-2924.
76. Broda, J., *Polymorphism in polypropylene fibers*. Journal of Applied Polymer Science, 2003. **89**(12): p. 3364-3370.
77. Al-Raheil, I.A., Qudah, A.M., and Al-Share, M., *Isotactic polypropylene crystallized from the melt. I. Morphological study*. Journal of Applied Polymer Science, 1998. **67**(7): p. 1259-1265.
78. Al-Raheil, I.A., Qudah, A.M., and Al-Share, M., *Isotactic polypropylene crystallized from the melt. II. Thermal melting behavior*. Journal of Applied Polymer Science, 1998. **67**(7): p. 1267-1271.
79. Lotz, B., Graff, S., and Wittmann, J.C., *Crystal morphology of the gamma-(triclinic) phase of isotactic polypropylene and its relation to the alpha-phase*. Journal of Polymer Science Part B-Polymer Physics, 1986. **24**(9): p. 2017-2032.
80. Li, Y.B. and Shen, K.Z., *The beta- and gamma-form distributions of isotactic Polypropylene injection molding controlled via melt vibration*. Journal of Macromolecular Science Part B-Physics, 2008. **47**(5): p. 1000-1007.
81. Somani, R.H., et al., *Orientation-induced crystallization in isotactic polypropylene melt by shear deformation*. Macromolecular Symposia, 2002. **185**: p. 105-117.
82. Yan, R.J. and Jiang, B.Z., *Melting behavior of drawn polypropylene*. Journal of Polymer Science Part B-Polymer Physics, 1993. **31**(9): p. 1089-1094.
83. Kim, Y.C., Ahn, W., and Kim, C.Y., *A study on multiple melting of isotactic polypropylene*. Polymer Engineering and Science, 1997. **37**(6): p. 1003-1011.

84. Pae, K.D. and Sauer, J.A., *Effect of thermal history on isotactic polypropylene*. Journal of Applied Polymer Science, 1968. **12**(8): p. 1901-&.
85. Yadav, Y.S. and Jain, P.C., *Melting behaviour of isotactic polypropylene isothermally crystallized from the melt*. Polymer, 1986. **27**(5): p. 721-727.
86. Guerra, G., et al., *Crystalline order and melting behavior of isotactic polypropylene (alpha-form)*. Journal of Polymer Science Part B-Polymer Physics, 1984. **22**(6): p. 1029-1039.
87. Jinan, C., et al., *Non-isothermal orientation-induced crystallization in melt spinning of polypropylene*. Journal of Applied Polymer Science, 1989. **37**(9): p. 2683-2697.
88. Brucato, V., Piccarolo, S., and La Carrubba, V., *An experimental methodology to study polymer crystallization under processing conditions. The influence of high cooling rates*. Chemical Engineering Science, 2002. **57**(19): p. 4129-4143.
89. Achtsnick, M., Hoogstrate, A.M., and Karpuschewski, B., *Advances in high performance micro abrasive blasting*. Cirp Annals-Manufacturing Technology, 2005. **54**(1): p. 281-284.
90. Soukhanovskii, V.A., et al., *Supersonic gas injector for fueling and diagnostic applications on the National Spherical Torus Experiment*. Review of Scientific Instruments, 2004. **75**(10): p. 4320-4323.
91. Van Steenkiste, T. and Gorkiewicz, D.W., *Analysis of tantalum coatings produced by the kinetic spray process*. Journal of Thermal Spray Technology, 2004. **13**(2): p. 265-273.
92. Aksel, M.H. and Eralp, O.C., *Gas Dynamics*. 1993, Prentice Hall International (UK) Ltd: Hemel Hempstead, Hertflrdshire.
93. Wilchinsky, Z.W., *Measurement of orientation in polypropylene film*. Journal of Applied Physics, 1960. **31**(11): p. 1969-1972.
94. Paradkar, R.P., et al., *On-line estimation of molecular orientation in polypropylene fibers using polarized Raman spectroscopy*. Applied Spectroscopy, 2001. **55**(5): p. 534-539.

95. deBaez, M.A., Hendra, P.J., and Judkins, M., *The Raman spectra of oriented isotactic polypropylene*. Spectrochimica Acta Part a-Molecular and Biomolecular Spectroscopy, 1995. **51**(12): p. 2117-2124.
96. Haynes, B.D., *An experimental and analytical investigation on the production of microfibers using a single hole melt blowing process*. 1991, University of Tennessee, Knoxville.
97. Andrews, E.H., *Cooling of a spinning thread-line*. British Journal of Applied Physics, 1959. **10**(1): p. 39-43.
98. Bheda, J.H. and Spruiell, J.E., *Dynamics and structure development during high-speed melt spinning of nylon-6. 1. Online experimental measurements*. Journal of Applied Polymer Science, 1990. **39**(2): p. 447-463.
99. Patel, R.M., Bheda, J.H., and Spruiell, J.E., *Dynamics and structure development during high-speed melt spinning of nylon-6.2. Mathematical-modeling*. Journal of Applied Polymer Science, 1991. **42**(6): p. 1671-1682.
100. Matsui, M., *Air drag on a continuous filament in melt spinning*. Transactions of the Society of Rheology, 1976. **20**(3): p. 465-474.
101. Mitsoulis, E. and Beaulne, M., *Numerical simulation of rheological effects in fiber spinning*. Advances in Polymer Technology, 2000. **19**(3): p. 155-172.
102. Henson, G.M., et al., *A thin-filament melt spinning model with radial resolution of temperature and stress*. Journal of Rheology, 1998. **42**(2): p. 329-360.
103. Sun, J., Subbiah, S., and Marchal, J.M., *Numerical analysis of nonisothermal viscoelastic melt spinning with ongoing crystallization*. Journal of Non-Newtonian Fluid Mechanics, 2000. **93**(1): p. 133-151.
104. Doufas, A.K. and McHugh, A.J., *Simulation of melt spinning including flow-induced crystallization. Part III. Quantitative comparisons with PET spinline data*. Journal of Rheology, 2001. **45**(2): p. 403-420.